

An Improved Global Model for Electronegative Discharge and Ignition Conditions for Peripheral Plasma Connected to a Capacitive Discharge

Sungjin Kim



Electrical Engineering and Computer Sciences
University of California at Berkeley

Technical Report No. UCB/EECS-2006-56

<http://www.eecs.berkeley.edu/Pubs/TechRpts/2006/EECS-2006-56.html>

May 15, 2006

Copyright © 2006, by the author(s).
All rights reserved.

Permission to make digital or hard copies of all or part of this work for personal or classroom use is granted without fee provided that copies are not made or distributed for profit or commercial advantage and that copies bear this notice and the full citation on the first page. To copy otherwise, to republish, to post on servers or to redistribute to lists, requires prior specific permission.

**An Improved Global Model
for Electronegative Discharge
and
Ignition Conditions for Peripheral Plasma
Connected to a Capacitive Discharge**

by

Sungjin Kim

B.S. (Seoul National University) 1992

M.S. (Seoul National University) 1994

A dissertation submitted in partial satisfaction of the

requirements for the degree of

Doctor of Philosophy

in

Engineering-Electrical Engineering and Computer Sciences

in the

Graduate Division

of the

University of California, Berkeley

Committee in charge:

Professor Michael A. Lieberman, Chair

Professor Allan J. Lichtenberg

Professor David B. Graves

Spring 2006

An Improved Global Model for Electronegative Discharge
and
Ignition Conditions for Peripheral Plasma Connected to a Capacitive Discharge

Copyright © 2006

by

Sungjin Kim

Abstract

An Improved Global Model for Electronegative Discharge and Ignition Conditions for Peripheral Plasma Connected to a Capacitive Discharge

by

Sungjin Kim

Doctor of Philosophy in Engineering-Electrical Engineering
and Computer Sciences

University of California, Berkeley

Professor Michael A. Lieberman, Chair

An improved volume-averaged global model is developed for a cylindrical electronegative (EN) plasma that is applicable over a wide range of electron densities, electronegativities, and pressures. It is applied to steady and pulsed-power oxygen discharges. The model incorporates effective volume and surface loss factors for positive ions, negative ions, and electrons combining three EN discharge regimes: a two-region regime with a parabolic EN core surrounded by an electropositive edge, a one-region parabolic EN plasma, and a one-region flat-topped EN plasma, spanning the plasma parameters and gas pressures of interest for low pressure. Pressure-dependent effective volume and surface loss factors for the neutral species, and an updated set of reaction rate coefficients for oxygen based on the latest results were incorporated. The model solutions yield important processing quantities as the neutral/ion flux ratio Γ_O/Γ_i , with the discharge aspect ratio, pulsed-power period, and duty ratio as parameters. For steady discharges, increasing $2R/L$ from 1 to 6 leads to a factor of 0.45 reduction in Γ_O/Γ_i . For

pulsed discharges with a fixed duty ratio, Γ_o/Γ_i is found to have a minimum with respect to pulse period. A 25% duty ratio pulse reduces Γ_o/Γ_i by a factor of 0.75 compared to the steady-state case.

A configuration of both theoretical and practical interest is a capacitive discharge connected through a dielectric or metal slot to a peripheral grounded region. The configuration is used in commercial dual frequency capacitive discharges, where a dielectric slot surrounding the substrate separates the main plasma from the peripheral grounded pumping region. Ignition of the peripheral plasma produces effects such as poor matching and relaxation oscillations that are detrimental to processing performance. Discharge models are developed for diffusion and plasma maintenance in the slot, and plasma maintenance in the periphery. The theoretical predictions of ignition conditions as a function of voltage and pressure are compared with experimental results for a driving frequency of 27.12 MHz and a gap spacing of 0.635 cm connecting the two regions, giving good agreement. Instabilities associated with the loss of confinement in both the kilohertz and hertz frequency range are discovered, and a physical model for the kilohertz frequency range instability is proposed.

Professor Michael A. Lieberman
Dissertation Committee Chair

*To my wife, Minjeong Kim and my daughter, Heeyeon Catherine Kim,
for all the love, support and encouragement.*

Contents

1. Introduction	1
1.1. Global Modeling of Electronegative Discharges	1
1.2. Peripheral Plasma Connected to a Capacitive Discharge	4
Part I. Improved Global Model for Electronegative Discharges	6
2. An Improved Global Model	7
2.1. Introduction	7
2.2. Model Physics	8
2.2.1. Wall Loss Factors	9
2.2.2. Finite Cylindrical Discharge	16
2.2.3. Neutral Dynamics	21
2.3. Model Equations and Solution Procedures	23
2.3.1. Energy Loss and Rate Coefficients	23
2.3.2. Particle Balance Equations	27
2.3.3. Energy Balance Equations	29
3. Solutions for Steady State Oxygen Discharges	30
3.1. Steady State Oxygen Discharge Results	30
3.2. Comparison with Previous Results	34
3.3. Comparison with Experimental Results	37

4. Solutions for Pulsed power Oxygen Discharges	40
4.1. Introduction	40
4.2. Time-average Electron Temperature and Densities	41
4.3. Flux Ratio of Neutrals to Positive Ions	43
5. Conclusions to Part I	46
Part II. Ignition Conditions	
for Peripheral Plasma Connected to a Capacitive Discharge	48
6. Calculations of Ignition Conditions	49
6.1. Introduction	49
6.2. Plasma Transport in the Slot	52
6.3. Capacitive Discharge Maintenance	57
6.4. Two Dimensional Effects on Discharge Maintenance	65
6.5. Maintenance Curves under Various Conditions	71
7. Experimental Results	
for a Capacitive Discharge Connected to a Peripheral Chamber	78
7.1. Experimental Setup and Diagnostics	78
7.1.1. Experimental Setup	78
7.1.2. Diagnostics	83
7.2. Experimental Measurements	87
7.3. Comparison of Experimental Maintenance Curve with Theory	93
7.4. Instabilities in Ar plasma Associated with the Peripheral Breakdown	97
7.5. A Model of High Frequency Instability	103
7.5.1. Electromagnetic Analysis of the Slot Impedance	103

7.5.2. Interaction of the Matching Network and Discharge	109
7.5.3 Time Variations in the Main Discharge	115
8. Conclusions to Part II	119
9. Discussions and Suggestions for Future Work	122
Appendix A. Reaction Rate Coefficients for Oxygen	125
Appendix B. Analysis on the Propagation Characteristics in the Slot	130
Appendix C. MATLAB Codes for Simulations	134
Bibliography	154

List of Figures

1.1.	Confined plasma operation of a dual frequency capacitive discharge; the cylindrical central discharge chamber with powered electrode radius R and axial height l is connected through an annular dielectric slot of radial extent w and axial gap spacing g to a grounded peripheral region of radial extent w_{per}	4
2.1.	Edge-to-center positive ion density ratio h_l versus n at 25 mTorr O_2 for $n_{e0} = 10^9$, 10^{10} , and 10^{11} cm^{-3} ; (a) from Eq(2.2), (b) from Eq(2.3), (c) from Eq(2.4), circles from Eq(2.7).....	12
2.2.	Edge-to-center positive ion density ratio h_l versus α_0 at 25 mTorr O_2 for $n_{e0} = 10^9$, 10^{10} , and 10^{11} cm^{-3} ; (a) from Eq(2.2), (b) from Eq(2.3), (c) from Eq(2.4), circles from Eq(2.7).....	13
2.3.	Edge-to-center positive ion density ratio h_l versus α_0 at $n_{e0} = 10^{10} \text{ cm}^{-3}$ for $p = 5$, 25, and 100 mTorr O_2 ; (a) from Eq(2.2), (b) from Eq(2.3), (c) from Eq(2.4), circles from Eq(2.7).....	14
2.4.	Size of EN region l/l_p versus central electronegativity α_0 at 25 mTorr O_2 for $n_{e0} = 10^9$, 10^{10} , and 10^{11} cm^{-3}	18
3.1.	Electron temperature T_e versus pressure at 500, 1000 and 2000 W of absorbed power.....	31
3.2.	Core electron density n_{e0} versus pressure at 500, 1000 and 2000 W of absorbed power.....	31
3.3.	Average negative ion density \bar{n}_{o^-} versus pressure at 500, 1000 and 2000 W of absorbed power.....	32
3.4.	Average electronegativity $\bar{\alpha}$ versus pressure at 500, 1000 and 2000 W of absorbed power.....	32
3.5.	Flux ratio of O neutrals to positive ions (Γ_0/Γ_+) versus pressure for $2R/L = 1, 3$ and 6 in low power range. Here $R = 15 \text{ cm}$ and the absorbed power at each $2R/L$ was adjusted to yield similar values of Γ_+ on the wall.....	33

3.6 (a).	Electron temperature T_e versus pressure for old model, old model with u_{B0} , and new model; $R = 15$ cm, $L = 5$ cm.....	35
3.6 (b).	Core electron density n_{e0} versus pressure for old model, old model with u_{B0} , and new model; $R = 15$ cm, $L = 5$ cm.....	36
3.7 (a).	Electron temperature T_e versus pressure comparison between models and experiment; $P_{\text{abs}} = 120, 180$ W; $R = 8$ cm, $L = 7.5$ cm.....	37
3.7 (b).	Core electron density n_{e0} versus pressure comparison between models and experiment; $P_{\text{abs}} = 120, 180$ W; $R = 8$ cm, $L = 7.5$ cm.....	38
4.1.	Time-averaged electron temperature T_e versus pulse period at $2R/L = 1$ for 50%, 25% duty ratio and for a CW plasma; $R = 15$ cm.....	41
4.2 (a).	Time-averaged electron density n_e versus pulse period at $2R/L = 1$ for 50%, 25% duty ratio and for a CW plasma; $R = 15$ cm.....	42
4.2 (b).	Time-averaged electron density n_e versus pulse period at $2R/L = 6$ for 50%, 25% duty ratio and for a CW plasma; $R = 15$ cm.....	43
4.3 (a).	Time-averaged flux ratio of O neutrals to positive ions (Γ_O/Γ_+) versus pulse period at $2R/L = 1$ for 50%, 25% duty ratio and for a CW plasma.....	44
4.3 (b).	Time-averaged flux ratio of O neutrals to positive ions (Γ_O/Γ_+) versus pulse period at $2R/L = 6$ for 50%, 25% duty ratio and for a CW plasma.....	44
6.1.	Confined plasma operation of a dual frequency capacitive discharge; the cylindrical central discharge chamber with powered electrode radius R and axial height l is connected through an annular dielectric slot of radial extent w and axial gap spacing g to a grounded peripheral region of radial extent w_{per} ; for this study $V_{\text{bias}}=0$	49
6.2.	Plasma density in the slot versus position at 50 mTorr in argon, showing the pinch-off length w_{po} using various diffusion models.....	57
6.3.	Symmetric one-dimensional capacitive discharge model; \tilde{V}_1 is the voltage drop across s_{rf} , the rf portion of the sheath, while \tilde{V} includes the additional rf voltage that drops across an additional dc sheath width arising from the additional dc potential; \tilde{V}_T also includes the voltage drop across the dielectric.....	58

6.4.	Measured and calculated maintenance voltage versus pressure for a 2.2 cm plate separation driven at 13.56 MHz in argon (no dielectric).....	64
6.5.	Maintenance curves for experimental conditions $f = 27.12$ MHz, $l = 2.54$ cm; $g = 0.635$ cm, $w = 3.8$ cm, and $w_{per} = 5.1$ cm; quartz dielectric confinement rings.....	73
6.6.	Maintenance curves for the same conditions as those of figure 6.5 but with $g = 0.3175$ cm.....	74
6.7.	Maintenance curves for the same conditions as those of figure 6.5 but with $w = 2$ cm	75
6.8.	Maintenance curves for the same conditions as those of figure 6.5 but with grounded metal confinement rings.....	76
7.1 (a).	A front view drawing of the experiment chamber (viewed from the ground electrode side) with descriptions of the components.....	79
7.1 (b).	A vertical-section drawing of the experiment chamber with descriptions of the componets.....	80
7.2.	Schematic diagram of the matching network used for the experiment.....	82
7.3.	The capacitive discharge experimental setup. Left is a view from the front, and the right is a view from the side.....	82
7.4.	A drawing of the floating potential measurement ring probe.....	84
7.5.	Equivalent circuit model of the potential measurement system.....	84
7.6.	The Langmuir probe. The probe tip length is 2.5 mm and its radius is 65 μ m (diameter = 0.13 mm).....	86
7.7.	Comparison of the two different states: (a) the confined plasma inside the quartz ring, (b) the plasma ignited in the periphery showing unstable blinking.....	88
7.8.	Hysteresis curves at 100 mTorr with upper level indicating breakdown of peripheral plasma and lower level indicating a confined plasma; (a) with respect to the absorbed rf powers, (b) with respect to the rf voltage V_{rf} measured with Z-scan.....	89
7.9.	Hysteresis curves with respect to the rf voltage at four different pressures with upper level indicating breakdown of peripheral plasma and lower level indicating	

	a confined plasma; the pressures are (a) 50 mTorr, (b) 75 mTorr, (c) 100 mTorr, and (d) 198 mTorr.....	90
7.10.	Time-varying optical emission I from the main discharge region, showing a high frequency (43.3 kHz) relaxation oscillation; 100 mTorr and 80 W absorbed power; argon emission at 748.7 nm was detected through a notch filter and a fiber optic cable; the zero of I is not calibrated.....	92
7.11.	Time-varying optical emission I from the main discharge region, showing a low frequency (4.21 Hz) relaxation oscillation; 77 mTorr and 202 W absorbed power; the zero of I is not calibrated.....	92
7.12.	Comparison of experimental data (measured by Z-scan probe) with the maintenance curves for experimental conditions $f = 27.12$ MHz, $l = 2.54$ cm, $g = 0.635$ cm, $w = 3.8$ cm, and $w_{per} = 5.1$ cm; quartz dielectric confinement rings. The upward triangles (\blacktriangle) denote the rf voltage when the periphery ignites, and the downward triangles (\blacktriangledown) denote the rf voltage when the confinement is restored.....	94
7.13.	Comparison of experimental data (measured by floating potential ring) with the maintenance curves for experimental conditions $f = 27.12$ MHz, $l = 2.54$ cm, $g = 0.635$ cm, $w = 3.8$ cm, and $w_{per} = 5.1$ cm; quartz dielectric confinement rings. The filled triangles denote the rf voltage just prior to the periphery ignition.....	96
7.14.	Time-varying optical emission I from the main discharge region (a) and the periphery (b), before the peripheral breakdown; 100 mTorr and 30 W absorbed power ($P_{fwd} = 200$ W / $P_{refl} = 170$ W); the zero of I is not calibrated.....	98
7.15.	Time-varying optical emission I from the main discharge region (a) and the periphery (b), right after the peripheral breakdown has started; 100 mTorr and 38 W absorbed power ($P_{fwd} = 200$ W / $P_{refl} = 162$ W); the zero of I is not calibrated.....	98
7.16.	Time-varying optical emission I from the main discharge region (a) and the periphery (b), with a little higher absorbed power than the case of figure 7.15; 100 mTorr and 48 W absorbed power ($P_{fwd} = 200$ W / $P_{refl} = 152$ W); the zero of I is not calibrated.....	99

7.17.	Time-varying optical emission I from the main discharge region (a) and the periphery (b), after the low frequency instability has started; 100 mTorr and 58 W absorbed rf power ($P_{\text{fwd}} = 200 \text{ W} / P_{\text{refl}} = 142 \text{ W}$); the zero of I is not calibrated.....	99
7.18.	Time-varying optical emission I and time-varying rf plasma potential from the main discharge region oscillating together with a frequency of 46.5 kHz; 100mTorr and 15W absorbed power ($P_{\text{fwd}} = 100 \text{ W} / P_{\text{refl}} = 85 \text{ W}$); the rf plasma potential shown here is the voltage V_1 measured by the floating potential ring without additional capacitance; the zero of I is not calibrated.....	100
7.19.	Time-varying optical emission I and time-varying Langmuir probe ion saturation current I_{i_sat} from the main discharge region oscillating together with a frequency of 46.5 kHz; 100mTorr and 15W absorbed power ($P_{\text{fwd}} = 100 \text{ W} / P_{\text{refl}} = 85 \text{ W}$); the zero of I is not calibrated.....	101
7.20.	Time-varying Langmuir probe ion saturation current I_{i_sat} from the main discharge region and the calculated plasma density oscillating together with a frequency of 46.5 kHz; 100mTorr and 15W absorbed power ($P_{\text{fwd}} = 100 \text{ W} / P_{\text{refl}} = 85 \text{ W}$); plasma densities were calculated by taking the time-average of I_{i_sat} for each 40 periods of 27.12 MHz oscillation.....	102
7.21.	Circuit model of the rf power source, L-type matching network, main discharge region, and dielectric slot region.....	104
7.22.	Model configuration used to determine the dispersion characteristics $k(\omega)$ and slot impedance Z_{sl} of the surface wave that propagates in the slot plasma.....	104
7.23.	(a) Real and imaginary part of the axial wavenumber k versus slot density n_{sl} , and (b) slot impedance Z_{sl} versus n_{sl} , for the base case described in the text....	108
7.24.	Magnitude of the source voltage $ V_T $ versus main discharge grounded electrode sheath voltage V_p , for six different slot plasma densities, for the base case conditions described in the text.....	111
7.25.	Voltages $V_{T \text{ res}}$ (a), V_p (b), and V_a (c) versus slot density n_{sl} , for the base case conditions.....	113
7.26.	(a) Slot plasma density, (b) grounded sheath voltage V_p , and (c) powered sheath voltage V_a versus time, for the base conditions.....	114

7.27.	Pulsed-power calculation of (a) main discharge optical emission, (b) plasma density, and (c) electron temperature versus time, for the base case conditions.....	116
7.28.	Time variations for a 46.5 kHz relaxation oscillation; $p = 100$ mTorr, $P_{\text{fwd}} = 100$ W, $P_{\text{refl}} = 85$ W; (a) optical emission signal; (b) plasma density n_e ; (c) plasma potential V_p	117

List of Tables

2.1. Basic Reaction Set for the Oxygen Discharge.....	24
2.2. Rate Coefficients for Excitation of Atomic Oxygen.....	26
2.3. Rate Coefficients for Excitation of Molecular Oxygen.....	26
6.1. Coefficients for collisionless and collisional models.....	53
6.2. Rate coefficients and threshold energies for argon.....	60

Acknowledgements

I am especially grateful to my research advisors, Professor Michael A. Lieberman and Professor Allan J. Lichtenberg, for their wonderful guidance, ideas, and support during the course of this work. The work reported in this thesis includes parts that are collaborative with them. It has resulted in two papers that have been submitted for publication (*‘Improved volume-averaged model for steady and pulsed-power electronegative discharges’* and *‘Plasma ignition in a grounded chamber connected to a capacitive discharge’*) and a third paper in preparation (*‘Relaxation oscillations in a capacitive discharge chamber connected to a peripheral grounded chamber’*). I wish to thank Professor David B. Graves for serving on my thesis committee, and Professor Nathan Cheung for serving on my qualifying examination committee.

I especially want to thank Jon T. Gudmundsson from University of Iceland for his great work on the calculations of new reaction rate coefficients for oxygen that appear in Appendix A and so many useful discussions during his visit that contributed a lot to this work. I also would like to thank my former colleague and visiting scholars to our lab, Alexei Marakhtanov, Jisoo Kim from Lam Research Corporation, and Zuwen Zhou from Guizhou Educational College, for many helpful discussions and contributions to this work. I want to thank Phill Guillory, Joe Donnelly, Bob Connolly, and Bob Hamilton from the Microfabrication Laboratory, Joe Gavazza and Ben Lake from the machine shop, and Tho Nguyen from Electronics Support Group, for their help and support throughout this work. I would also thank Eric Hudson and Lam Research Corporation for the support and useful discussions on the experiments of peripheral plasma ignition.

I also gratefully acknowledge the use of unpublished experimental results of Takashi Kimura at Nagoya Institute of Technology, used in the steady state result comparison with theory.

This work was partially supported by the Lam Research Corporation, the State of California MICRO Program, National Science Foundation Grant ECS-0139956, and a UC Discovery Grant from Industry-University Cooperative Research Program (IUCRP).

Chapter 1

Introduction

1.1 Global Modeling of Electronegative Discharges

As the feature size of microelectronic devices shrink, processing steps become more critical and demanding. Therefore, a better understanding of plasma behavior becomes increasingly important in providing required process controls. Most of the plasma processing involves electronegative (EN) gas mixtures, such as O_2 , Cl_2 , CF_4 , SF_6 , or their mixtures. For EN plasmas, due to the presence of negative ions, the number of equations governing the equilibrium is large and analysis becomes complicated.

Previous methods that have been used to treat the numerous processes in EN plasmas have been global models in which the equation set of the charged species has been expressed in terms of volume-averaged quantities. In one class of global models, all quantities are assumed to be uniform over a cylindrical discharge. The positive ion flux emerging from the plasma is calculated by using flux factors that have been determined separately for one-dimensional plane-parallel and cylindrical plasmas with only positive ions present [1,2]. This technique has been applied to weakly electronegative discharges, such as low pressure, high power O_2 and O_2/Ar mixtures [3-5], CF_4/Ar mixtures [6], and highly electronegative Cl_2 [4,7]. Pulsed-power models have been developed for Cl_2 [8,9], SF_6 [10], and O_2 [11,12]. For the time-independent (CW) cases with weakly attaching

gases at low pressure and high power [3,5], the electronegativity $\alpha \equiv n_-/n_e$ at the plasma edge was considered to be sufficiently low that the electropositive Bohm velocity was used in the calculation of the wall flux. For higher α in strongly attaching gases, usually at higher pressure and lower power [4,7], heuristic expressions were used to calculate the positive-ion edge fluxes based on the average electronegativity of the discharge. There are significant errors introduced by these approximations, which ignore the effects of plasma profiles, with the low and high α approximations not smoothly joining at low pressure. The pulsed models [8-12], using uniform quantities, followed the same format as the CW models and suffered from the same inaccuracies.

A different type of global model has been used for a high electronegativity Cl_2 discharge in a high aspect ratio discharge chamber [13]. In this case a parabolic profile was used in the small axial dimension, while the radial profile was taken to be uniform and the radial loss neglected. The use of an axial parabolic profile is an approximation justified by a more complete 1D analysis [14,15]. In that study it was found that over a fairly sizeable range of high electronegativity values, $\alpha_0 \equiv n_{-0}/n_{e0}$ with n_{-0} the central negative ion density and n_{e0} the (assumed constant) electron density, a parabolic negative ion profile, extending over the entire plasma, reasonably approximated calculated profiles. Assumptions of uniform radial profile and negligible radial flux were not justified, but taken to be intuitively reasonable with an aspect ratio $2R/L$ of 20 in the device.

Recently, more realistic models have been constructed for the low α regime, incorporating the concept of a stratified plasma consisting of an electronegative core surrounded by an electropositive edge [16-18] which used a loss factor h_l for the electrons constructed self-consistently in 1D for the electropositive edge [19]. The most

complete model for a finite length cylindrical electronegative (EN) plasma was constructed [18] by introducing a single length scale that defines a smaller EN cylinder embedded in the larger plasma. In all of these models, single types of positively and negatively charged ions and electrons were assumed to be the principal charged species in determining the additional parameter. The plasma thus formed was incorporated into a full model of an attaching feedstock gas with the relevant species and reaction rates included. A complete generalized global model, with varying charged-species profiles depending on the electronegativity, includes one additional spatial parameter and one additional equation. The resulting equations are readily solved as in previous global models. Results, applicable to lower pressures and modest electronegativities, were compared to experiments in an oxygen discharge, obtaining reasonably good agreement with measured parameters [18].

In the models described above, comparisons with experiments indicated reasonable agreement with some discharge parameters. However, as described above, the models were limited to certain parts of the parameter space. It is apparent that a more broadly applicable model for a 2D EN plasma is needed.

In Part I of this dissertation, we present a new volume-average model developed for cylindrical (radius R , length L) steady and pulsed-power electronegative (EN) discharges, valid over a wider range of plasma parameters and pressures than previous models.

1.2 Peripheral Plasma Connected to a Capacitive Discharge

The transport and maintenance of rf-generated plasma in grounded regions is both of physical interest and has technological implications. A particular configuration, which has been found to have desirable processing applications [20], shown schematically in figure 1.1 is a dual frequency capacitive discharge, with the main cylindrical discharge connected to a peripheral cylindrical (pumping) region through an annular slot narrowed with a dielectric. The feedstock gas flows from the main discharge region through the slot, and is pumped in the grounded peripheral chamber.

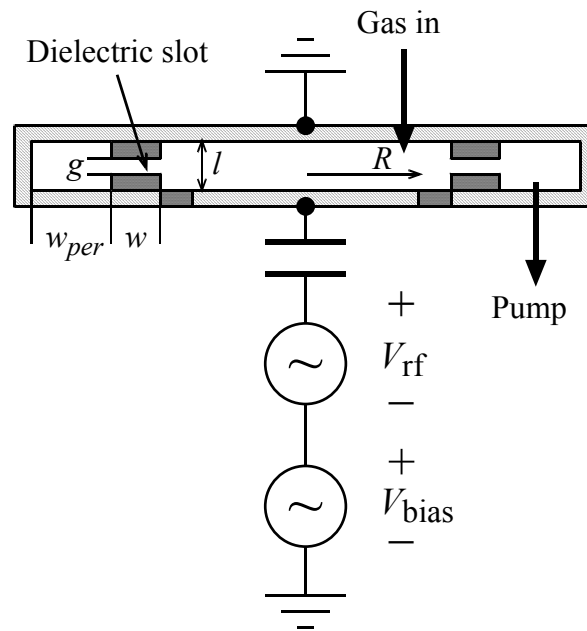


Figure 1.1. Confined plasma operation of a dual frequency capacitive discharge; the cylindrical central discharge chamber with powered electrode radius R and axial height l is connected through an annular dielectric slot of radial extent w and axial gap spacing g to a grounded peripheral region of radial extent w_{per} .

There are two purposes for using the structure described above. One is to control the processing pressure by adjusting the gap spacing in the slot. The other is to separate the main processing discharge from peripheral pumping region. In a commercial reactor such as a dry etching chamber, the separation of processing plasma from the periphery has several benefits because the plasma enhanced chemical reactions are confined to the region inside the dielectric ring. This prevents build-up of chamber wall polymer deposition, which reduces wafer contamination from the particles. Because the chamber wall outside the confinement ring remains clean after many wafers have been processed, process drift can be minimized by maintaining a constant wall condition. Also, because the chamber wall cleaning step is easier, overall throughput of the system can be enhanced.

However, in operation of a commercial reactor, a peripheral plasma is sometimes formed, which produces detrimental effects on processing. The undesired plasma is, under some conditions, ignited and maintained inside the peripheral pumping region, affecting the matching condition of the system or making the processing discharge unstable. Until now, this peripheral plasma breakdown seemed to be unpredictable and uncontrollable, for there were no physical models to explain the phenomenon.

In Part II of this dissertation, we present a study which is designed to understand the conditions of peripheral ignition, and therefore propose a model to determine the conditions required to confine the discharge inside the main processing region.

Part I

Improved Global Model for Electronegative Discharges

Abstract

An improved volume-averaged global model is developed for a cylindrical electronegative (EN) plasma that is applicable over a wide range of electron densities, electronegativities, and pressures. It is applied to steady and pulsed-power oxygen discharges. The model incorporates effective volume and surface loss factors for positive ions, negative ions, and electrons combining three EN discharge regimes: a two-region regime with a parabolic EN core surrounded by an electropositive edge, a one-region parabolic EN plasma, and a one-region flat-topped EN plasma, spanning the plasma parameters and gas pressures of interest for low pressure. Pressure-dependent effective volume and surface loss factors for the neutral species, and an updated set of reaction rate coefficients for oxygen based on the latest results were incorporated. The model solutions yield important processing quantities as the neutral/ion flux ratio Γ_O/Γ_i , with the discharge aspect ratio, pulsed-power period, and duty ratio as parameters. For steady discharges, increasing $2R/L$ from 1 to 6 leads to a factor of 0.45 reduction in Γ_O/Γ_i . For pulsed discharges with a fixed duty ratio, Γ_O/Γ_i is found to have a minimum with respect to pulse period. A 25% duty ratio pulse reduces Γ_O/Γ_i by a factor of 0.75 compared to the steady-state case.

Chapter 2

An Improved Global Model

2.1 Introduction

For next-generation plasma etching processes in the microelectronics industry, control and reduction of the ratio of neutral radical flux to ion flux (Γ_O/Γ_i) at the wafer surface are required to accomplish the patterning of the vertical etch profiles of high aspect-ratio features [21]. To determine the effect of pressure, power and pulsing, on the plasma parameters and the flux ratio, more accurately, we have developed a new volume-average model of cylindrical (radius R , length L) steady and pulsed-power electronegative (EN) discharges, valid over a wider range of plasma parameters and pressures than previous models.

In this work, we extend the generalized global model to a broader range of electronegativities and pressures, combining three electronegative discharge regimes: (a) a two-region low pressure regime with a parabolic EN core surrounded by an EP edge [18], (b) a one-region parabolic EN plasma applicable at low pressures and high α_0 's, and (c) a one-region flat-topped EN plasma applicable at higher pressures and high α_0 's. These regimes span the range of plasma densities and gas pressures of interest for low pressure processing. We also introduce density-weighted averages for multiple positive and negative ion species, and we introduce pressure-dependent effective volume and

surface loss factors for the neutral species. We apply the model to steady-state and pulsed discharges in oxygen, using a set of reaction rate coefficients based on the latest published cross-section sets and measurements. We give example solutions of the model for both steady and pulsed power excitation, concentrating on the variations of the neutral radical/ion flux ratio Γ_o/Γ_i with respect to discharge parameters such as the aspect ratio $2R/L$ and the pulsed-power period and duty ratio (pulse on-time/pulse period). We compare the results to experimental values for oxygen over a range of pressures. In section 2.2 we describe the physical basis for the model. In section 2.3 we give the complete set of time-varying equations and the procedures used to determine their solutions numerically. In chapter 3 we present solutions to the model for CW oxygen plasmas and compare the results to previous calculations and to an experiment. In chapter 4 results are presented for a pulsed oxygen discharge. Conclusions and further discussion are given in chapter 5. Appendix A gives details of the reaction rate coefficients used.

2.2 Model Physics

In recent years, a reasonable understanding of electronegative discharge equilibria has been achieved (see [2], section 10.3 and references therein). At moderate electronegativities (regime a), a plasma containing negative ions tends to stratify into an EN core having a parabolic negative ion density profile, and an electropositive (EP) edge [22] (see also reference [14,19,23,24]). The electron density is nearly uniform in the core, $n_e = n_{e0}$, falling gradually to an edge density n_{es} at the plasma sheath edge. The stratification occurs because the ambipolar field required to confine the more energetic

mobile electrons pushes the negative ions into the discharge center. Since the negative ions generally have a low temperature compared to the electrons, only a very small field is required to confine them to the core. The higher temperature electrons, in Boltzmann equilibrium with this field, have a nearly uniform density in the presence of the negative ions, but then form a more usual electropositive plasma in the edge regions. At higher electronegativities (regime b), the EP edge region disappears, and at still higher electronegativities (regime c), the profile of the negative ions tends to flatten in the discharge center. These transitions are also dependent on electron density and pressure. In a low pressure EP discharge, ions flow into the sheath edge at the Bohm velocity, $u_B = (eT_e/M)^{1/2}$. The Bohm velocity is modified (reduced) by the presence of negative ions near the sheath edge ([2], section 6.4). To capture the profile changes and the change in Bohm velocity as the electronegativity varies, it is convenient to introduce a loss factor h that relates the flux Γ of electron-ion pairs lost to the wall to the product of the central positive ion density and the EP Bohm velocity. For one-dimensional plane parallel geometry

$$\Gamma = h_l n_{+0} u_B \quad (2.1)$$

where $n_{+0} = n_{-0} + n_{e0}$ is the central positive ion density.

2.2.1 Wall Loss Factors

The h_l wall loss factors have been derived previously for the various electronegativity regimes. We adapt 1D results from (a) the low-pressure parabolic-profile EN core with a low pressure EP edge [14], (b) one-region EN parabolic-profile and (c) one-region flat-topped EN profile [23]. We also considered a fourth regime (d)

with a flat-topped EN core and an EP edge [24], but, as seen in the figures described below, this regime only specifies the transition between regimes (a) and (c), and therefore, is not incorporated into the overall EN discharge model, which includes heuristic transitions between regimes. We ignore effects due to ion-sound speed limitations (shocks) within the discharge volume [25], but do incorporate within the h_l factor a reduced Bohm velocity at the plasma edge. Including an internal ion sound limitation somewhat lowers the values of the h_l factors. We do not consider the highly electronegative regime for which the wall sheath potential collapses, allowing negative ions to flow to the walls. We account for the different properties (temperature, mass, mean free path) of the positive and negative ion species. We use a constant mean free path model for the diffusion coefficients: $D_{\pm} = \pi \bar{v}_{\pm} \lambda_{\pm} / 8$, with $\bar{v}_{\pm} = (8eT_{\pm} / \pi M_{\pm})^{1/2}$ and λ_{\pm} the appropriate ion-neutral mean free path. Denoting the edge-to-center positive ion density ratios for the three regimes as h_a , h_b , and h_c , respectively, then approximate results for the h_l factors are:

$$h_a \approx \frac{0.86}{\left(3 + \eta \frac{l_p}{\lambda_+}\right)^{1/2}} \frac{1}{1 + \alpha_0} \equiv h_{l_0} \frac{1}{1 + \alpha_0} \quad (2.2)$$

which as electronegativity $\alpha_0 \rightarrow 0$ approaches the constant electropositive result h_{l_0} of Godyak [1],

$$h_b \approx \frac{1}{\gamma_-^{1/2} + \gamma_+^{1/2} \frac{\eta}{(2\pi)^{1/2}} \frac{l_p}{\lambda_+}} \frac{\alpha_0}{1 + \alpha_0} \equiv h_{l_{\infty}} \frac{\alpha_0}{1 + \alpha_0} \quad (2.3)$$

which as $\alpha_0 \rightarrow \infty$ gives a result $h_{l_{\infty}}$ that is independent of both α_0 and n_{e0} , and

$$h_c = \frac{1}{\gamma_-^{1/2} + \gamma_+^{1/2} \frac{n_*^{1/2} n_{+0}}{n_{-0}^{3/2}}} \approx \frac{1}{\gamma_-^{1/2} + \gamma_+^{1/2} \frac{n_*^{1/2}}{n_{-0}^{1/2}}} \quad (2.4)$$

which depends on n_{-0} but is independent of α_0 and n_{e0} . We have used the simplifying nomenclature

$$\eta = \frac{2T_+}{T_+ + T_-}; \quad \gamma_- = \frac{T_e}{T_-}; \quad \gamma_+ = \frac{T_e}{T_+}; \quad l_p = L/2 \quad (2.5)$$

$$n_* = \frac{15}{36} \left(\frac{8eT_+}{\pi M_+} \right)^{1/2} \frac{\eta^2}{K_{\text{rec}} \lambda_+} \quad (2.6)$$

where, in the preceding expressions, l_p is the half-length of the system, the subscripts + and - denote the (one type of) positive and negative ions, the subscript 0 denotes the center values, and K_{rec} is the positive-negative ion recombination coefficient.

The exact results for the h_l -factors for the four regimes are shown in figure 2.1 (versus negative ion density) and figure 2.2 (versus electronegativity) for the case of an oxygen discharge at 25 mTorr for three different electron densities n_e , with $T_+ = T_- = 0.054$ V, $M_+ = M_- = 32$ amu, $\lambda_+ = \lambda_- = 1/330p$ (Torr), $T_e = 3$ V, $K_{\text{rec}} = 1.4 \times 10^{-7}$ cm³/s, and $l_p = 9.5$ cm. (In this somewhat idealized case, the positive and negative ions have the same mass, temperature, and mean free path). The solid lines labeled with the regime (in parentheses) give the results and indicate the region of validity of the model. Electron densities of 10^9 , 10^{10} and 10^{11} cm⁻³ are also labeled in the figures. The dotted lines give the regions where an internal shock (ion sound speed limitation) occurs in the model, and thus indicate regions where the models are not valid.

To obtain a single description of the fluxes covering the full parameter range, we “stitch together” the edge-to-center density ratios (h_l -factors) using a linear ansatz that

sums the h_l -results for regimes (a), (b), and (c), determining an h_l factor to be used in (2.1):

$$h_l = h_a + h_b + h_c. \quad (2.7)$$

Equation (2.7) is plotted as the circles in figure 2.1 and figure 2.2. It is seen to give a smooth fit to the actual h_l -factors in their regions of validity, and it approximately captures the transitions between the regimes. The ansatz, which slightly overestimates the flux, gives errors less than 30% for this 25 mTorr oxygen discharge case, at the

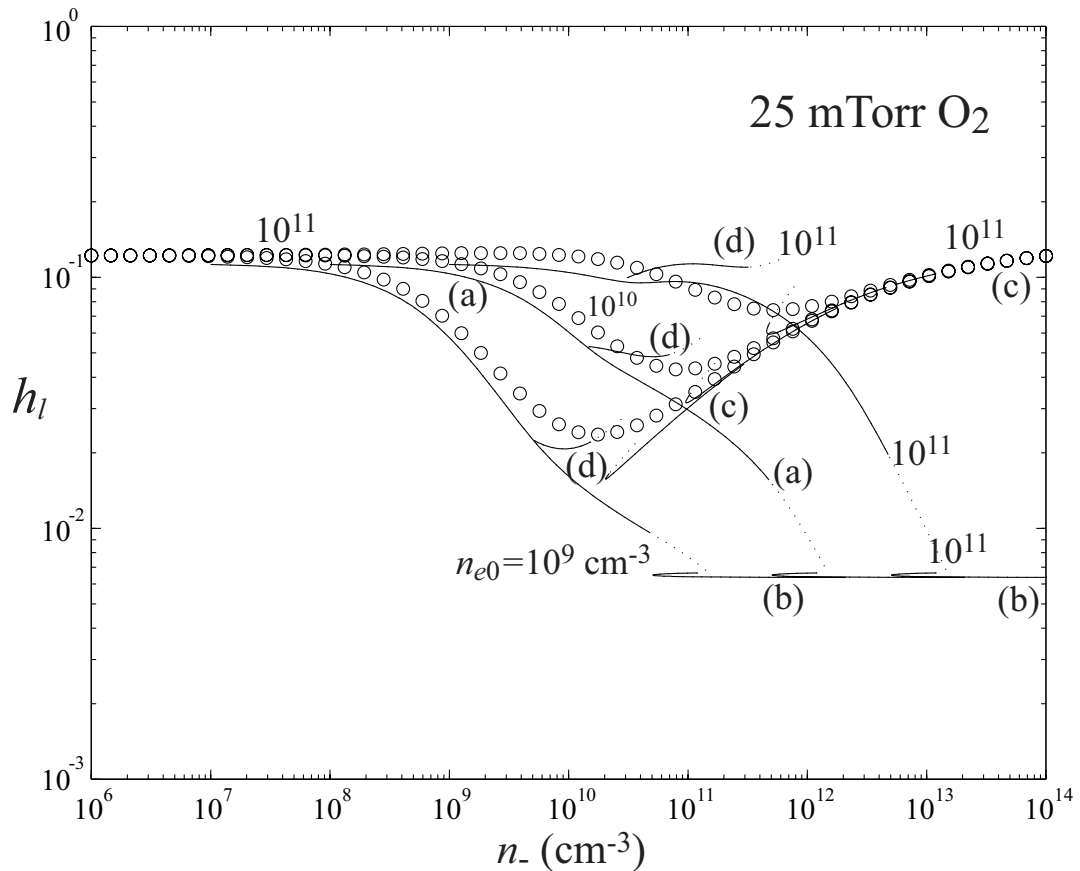


Figure 2.1. Edge-to-center positive ion density ratio h_l versus n_+ at 25 mTorr O_2 for $n_{e0} = 10^9, 10^{10},$ and 10^{11} cm^{-3} ; (a) from Eq(2.2), (b) from Eq(2.3), (c) from Eq(2.4), circles from Eq(2.7).

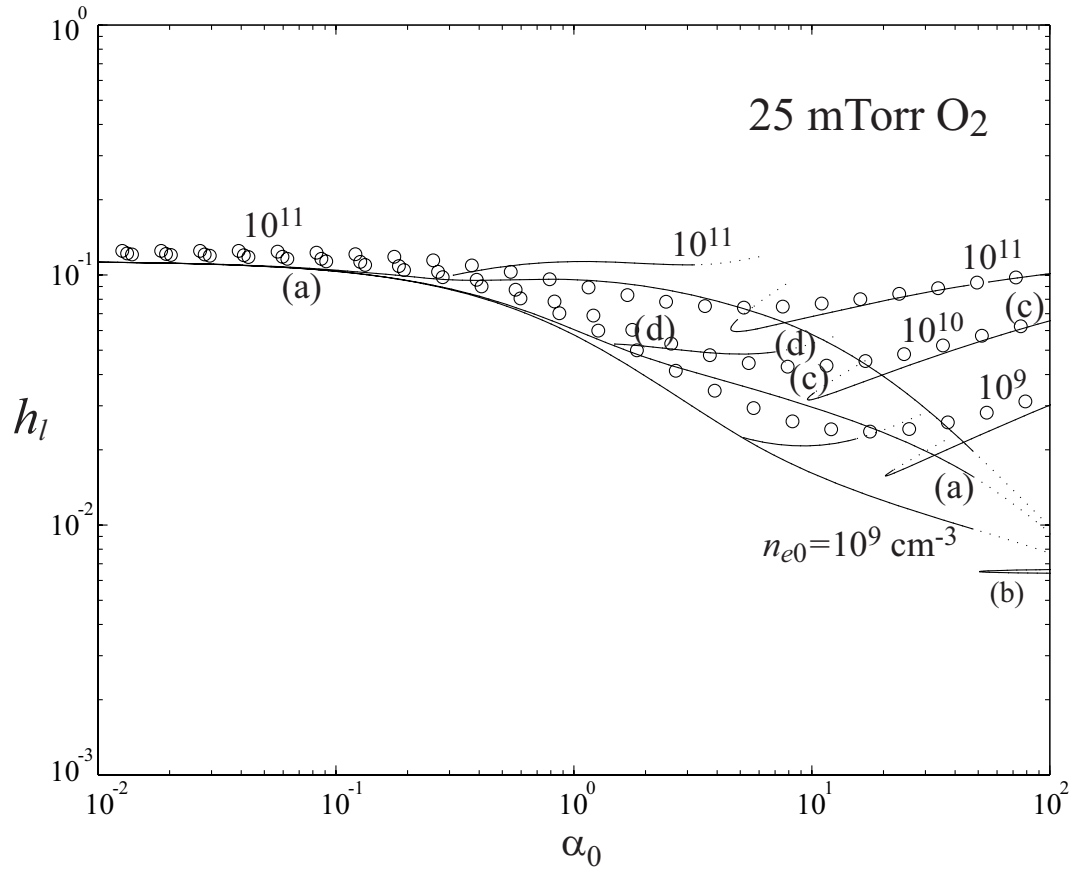


Figure 2.2. Edge-to-center positive ion density ratio h_l versus α_0 at 25 mTorr O_2 for $n_{e0} = 10^9$, 10^{10} , and 10^{11} cm^{-3} ; (a) from Eq(2.2), (b) from Eq(2.3), (c) from Eq(2.4), circles from Eq(2.7).

transitions between the regimes. We also see from (2.7) and figures 2.1 and 2.2 that, at 25 mTorr, the regime (b) giving h_b is unimportant. At this pressure and higher pressures the flattening of the core becomes important before the core extends to the periphery, a situation that does not hold at sufficiently low pressures and electron densities. Calculations for oxygen at 5 mTorr and 100 mTorr at $n_{e0} = 10^{10}$ cm^{-3} are compared with $p = 25$ mTorr in figure 2.3, to indicate the pressure dependence. Note also that in h_a , the principal electronegative dependence is on α_0 , such that plotting h_l versus α_0 (figure 2.2)

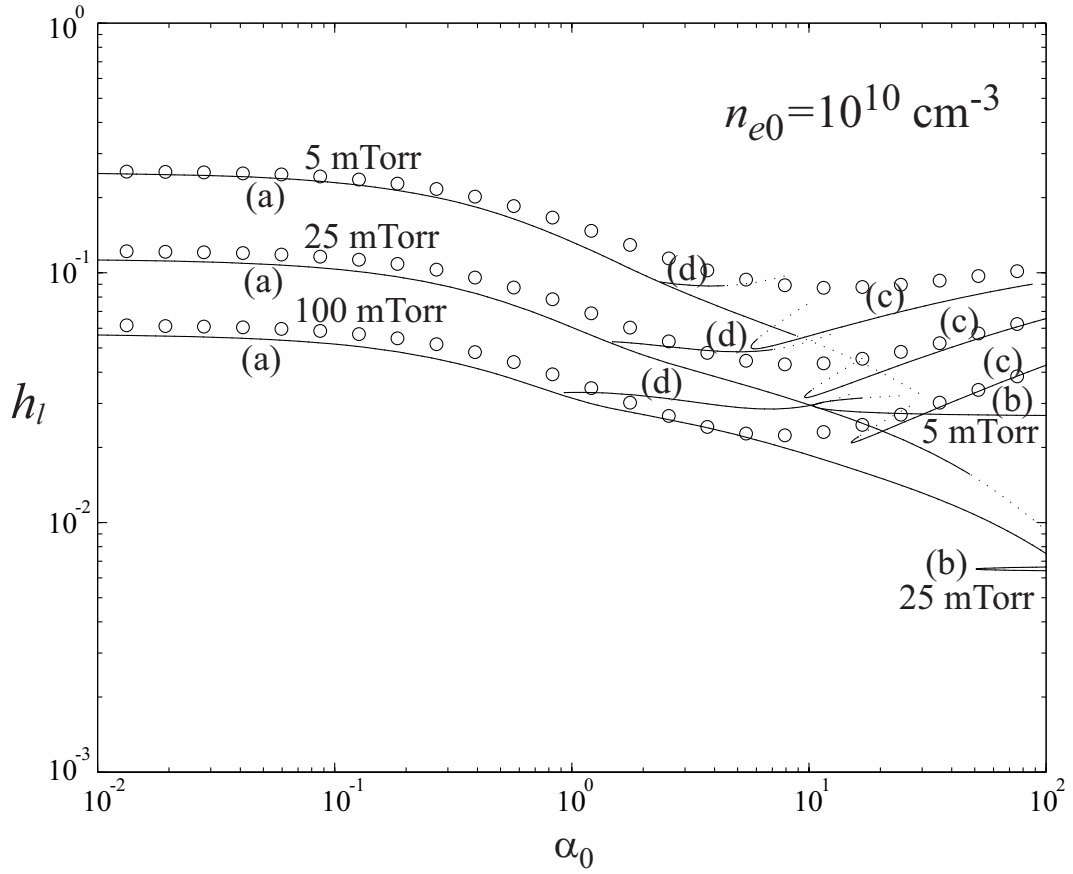


Figure 2.3. Edge-to-center positive ion density ratio h_l versus α_0 at $n_{e0} = 10^{10} \text{ cm}^{-3}$ for $p = 5, 25, \text{ and } 100 \text{ mTorr O}_2$; (a) from Eq(2.2), (b) from Eq(2.3), (c) from Eq(2.4), circles from Eq(2.7).

brings the values close together at three widely separated values of n_{e0} . The opposite situation holds for h_c , where the dependence on n_0 (figure 2.1) brings the values of h_l versus n_0 together at the various n_{e0} 's.

To understand physically the results shown in the figures, we examine more closely the expression for the h_l factors in (2.2)-(2.4), and the justification of the ansatz in (2.7). For regime (a) with $\alpha_0 \ll 1$, the quantity h_{l0} in (2.2) is the Godyak result [1] for the electropositive end-loss factor in one-dimensional slab geometry, which is independent of

α_0 (or n_{-0}). As the central electronegativity builds up, in this two-region model, the principal result is that $n_{+0} = (1 + \alpha_0)n_{e0}$ increases in the EN core, with the loss flux in the EP edge remaining nearly a constant, accounting for the decrease of h_l as $(1 + \alpha_0)^{-1}$. There are weaker dependencies on n_{e0} (at fixed α_0) seen in figure 2.2, which we do not take into account in (2.2). As α_0 increases to be significantly greater than unity, the central electronegative core fills most of the plasma, such that the loss flux is governed primarily by a diffusion solution in an electronegative plasma, having a parabolic profile in the approximation of regime (b) in (2.3). The h_l factor goes to a constant value $h_{l\infty}$ as $\alpha_0 \gg 1$, which is much below the electropositive constant value h_{l0} for $\alpha_0 \ll 1$, because the Bohm speed at the plasma-sheath edge is governed by the low negative ion temperature rather than the high electron temperature as in regime (a). As α_0 increases further, the central electronegative core also begins to flatten because the positive-negative ion recombination loss competes with the positive ion diffusion to make the particle balance more local. This leads to a steepening of the edge gradient and therefore to an increase of h_l in regime (c) with increasing n_{-0} (or α_0 at constant n_{e0}). The pressure dependence ($n_* \propto p$) indicates that this steepening occurs for smaller values of n_{-0} at higher pressure, because the diffusion loss decreases with pressure and the recombination loss remains relatively constant. Since over the entire range of parameters the regime (a, b, or c) is determined by the largest of h_a , h_b , and h_c , as seen from previous work [24], the ansatz sum in (2.7) works well, with h_b significant only at the lowest pressures and electron densities.

If there are multiple positive or negative ion species, then we use density-weighted quantities for the temperatures, mean free paths, ion masses, and recombination coefficient in (2.2)-(2.7), as well as a density-weighted Bohm velocity in (2.1). Density weighting means using such quantities as

$$\bar{T}_+ = \frac{T_{1+}n_{1+} + T_{2+}n_{2+}}{n_{1+} + n_{2+}}. \quad (2.8)$$

2.2.2 Finite Cylindrical Discharge

We consider in this work cylindrical discharges having $L \leq 2R$, and we use the flux given in (2.1)-(2.7) as incident on *both* the end walls *and* the circumferential wall. There is some error in using (2.1)-(2.7) on the circumferential wall, which we discuss below, after presenting the complete model. The main calculation that is required to complete the model is a determination of the extra parameter l_- , the half-width of the EN core, and its use to define an *effective volume of negative ions*, to be used in a global model. In the high- α_0 regimes (b) and (c), the core extends over the entire plasma and $l_- = l_p$. In regime (a), l_- can be found from the results given by Kouznetsov *et al.* [19] For small α_0 , such that $l_- \ll l_p$, one finds that

$$1 - \frac{l_-}{l_p} \approx 1 - \left(\frac{\alpha_0 R_\lambda}{h_{\text{eff}}} \right)^{1/2} \equiv \beta_1 \quad (2.9)$$

and for larger α_0 such that $l_p - l_- \ll l_p$, one finds

$$1 - \frac{l_-}{l_p} \approx \frac{h_{\text{eff}} - \alpha_0 R_\lambda}{R_{\text{rec}} F(\alpha_0)} \equiv \beta_2 \quad (2.10)$$

where

$$R_\lambda = \left(\frac{2\pi}{\gamma_+} \right)^{1/2} \frac{\lambda_+}{l_p} \frac{1}{\eta}; \quad h_{\text{eff}} = h_{i0} + (1 - h_{i0})\alpha_0 R_\lambda \quad (2.11)$$

$$R_{\text{rec}} = \frac{K_{\text{rec}} n_{e0} l_p}{u_B}; \quad F(\alpha_0) = \frac{8}{15} \alpha_0^2 + \frac{2}{3} \alpha_0. \quad (2.12)$$

R_λ in (2.11) gives the pressure dependence of l_- , and R_{rec} in (2.12) gives the n_{e0} dependence. Results (2.9)-(2.12) hold in regime (a) of the two-region model, for moderate electronegativities

$$0 < \alpha_0 R_\lambda < 1. \quad (2.13)$$

As $\alpha_0 R_\lambda$ approaches unity, h_{eff} in (2.11) also approaches unity; that is, there is no drop-off of the electron density in the vanishingly-thin edge region of the two-region model. A reasonable ansatz combining (2.9) and (2.10) and valid over the entire range of (2.13) is found to be

$$\frac{l_-}{l_p} = 1 - \frac{1}{\left(\frac{1}{\beta_1^3} + \frac{1}{\beta_2^3} \right)^{1/3}}. \quad (2.14)$$

The fits (circles) from (2.14) to the actual l_-/l_p (solid lines) from the complete equation set given by Kouznetsov *et al.* [19] are shown in figure 2.4 for the 25 mTorr oxygen case. Thus (2.14) reasonably captures the dependence of l_-/l_p on α_0 and n_{e0} over the applicable range of pressures and densities.

Following Kimura *et al.* [18], if the negative ions have a parabolic density profile in z , the density profile in r can be approximated as uniform in r for $r \leq R - l_p$

$$n_-(r, z) = n_{e0} \alpha_0 \left(1 - \frac{z^2}{l_-^2} \right); \quad r \leq R - l_p \quad (2.15)$$

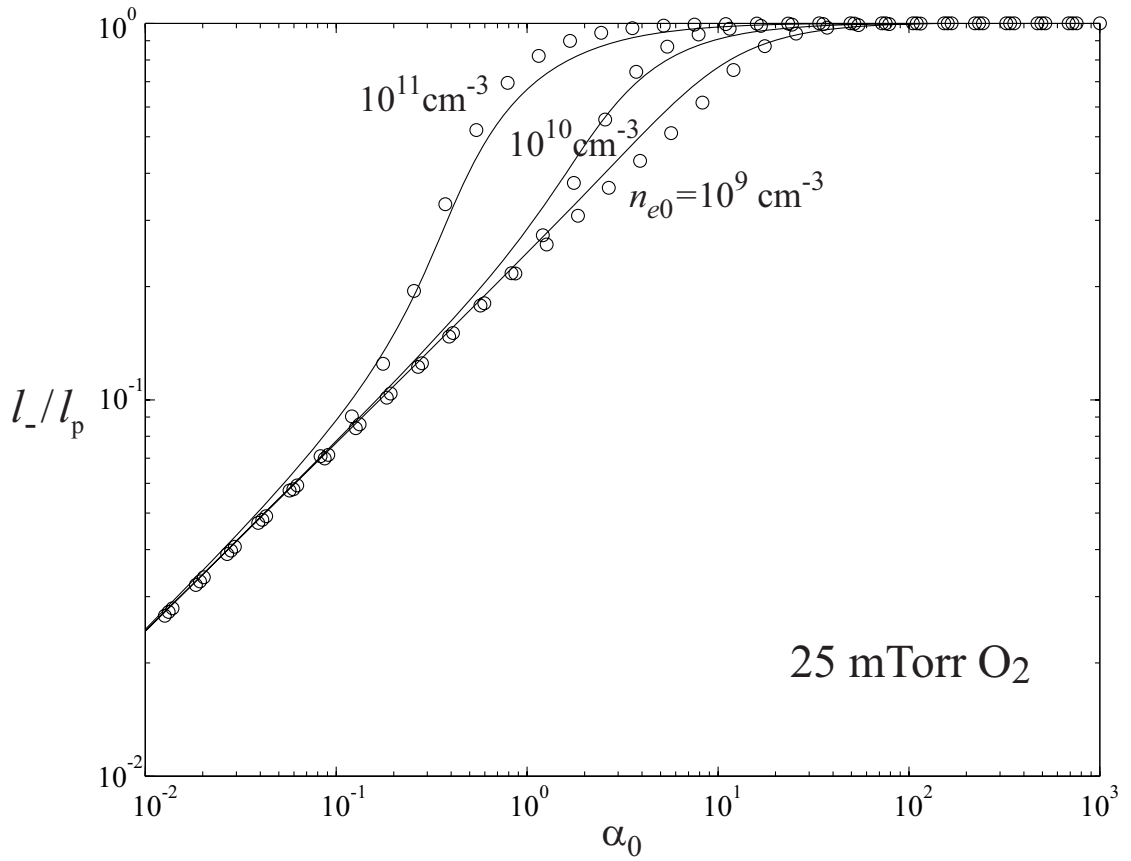


Figure 2.4. Size of EN region l/l_p versus central electronegativity α_0 at 25 mTorr O₂ for $n_{e0} = 10^9, 10^{10},$ and 10^{11} cm^{-3} .

and as parabolic for $R - l_p < r < r_-$,

$$n_-(r, z) = n_{e0} \alpha_0 \left(1 - \frac{(r - r_- + l_-)^2}{l_-^2} \right) \left(1 - \frac{z^2}{l_-^2} \right); \quad R - l_p < r < r_- \quad (2.16)$$

where

$$r_- = R - l_p + l_- \quad (2.17)$$

is the radius of the electronegative region.

Letting $V = 2\pi R^2 l_p$, the volume of the entire plasma, we can define an average negative ion density over the entire plasma volume by

$$\bar{n}_- V \equiv n_{-0} V_- \quad (2.18)$$

where V_- is the *effective volume for negative ions*, given by

$$V_- = \frac{\iint n_-(r, z) 2\pi r dr dz}{n_{-0}} = \frac{2}{3} \left(1 - \frac{2}{3} \frac{l_-}{r_-} + \frac{1}{6} \frac{l_-^2}{r_-^2} \right) 2\pi r_-^2 l_- . \quad (2.19)$$

From (2.18), we have the relation

$$n_{-0} = \frac{V}{V_-} \bar{n}_- . \quad (2.20)$$

To determine the relation between peak and average values of positive ion density, we use the quasineutrality relations

$$n_{+0} = n_{-0} + n_{e0} \quad (2.21)$$

$$\bar{n}_+ = \bar{n}_- + n_{e0} . \quad (2.22)$$

Eliminating n_{e0} from (2.21) and (2.22) yields

$$n_{+0} = \bar{n}_+ - \bar{n}_- + n_{-0} . \quad (2.23)$$

Substituting n_{-0} from (2.20) into (2.23), we find

$$n_{+0} = \bar{n}_+ + \left(\frac{V}{V_-} - 1 \right) \bar{n}_- . \quad (2.24)$$

Equations (2.20) and (2.24) give the relations between peak and average values of the negative and positive ion densities, as needed to relate the average (global) quantities to the plasma structure.

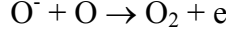
For $l_-/l_p \leq 1$, in Kimura *et al.* [18], the negative ion balance equation was found to be

$$V \frac{d\bar{n}_-}{dt} = K_{\text{att}} n_g n_{e0} V - K_{\text{rec}} n_{-0} n_{+0} V_{\text{rec}} \quad (2.25)$$

where the *effective volume for recombination* of positive and negative ions is

$$V_{\text{rec}} = \left[\frac{2\pi l_-}{1 + \alpha_0} \right] \left[\frac{8}{15} \alpha_0 \left(r_-^2 - \frac{14}{15} r_- l_- + \frac{4}{15} l_-^2 \right) + \frac{2}{3} \left(r_-^2 - \frac{2}{3} r_- l_- + \frac{1}{6} l_-^2 \right) \right]. \quad (2.26)$$

Adding a detachment process to (2.25), such as



we obtain

$$V \frac{d\bar{n}_-}{dt} = K_{\text{att}} n_g n_{e0} V - K_{\text{rec}} n_{-0} n_{+0} V_{\text{rec}} - K_{\text{det}} n_{\text{O}} n_{-0} V. \quad (2.27)$$

The positive ion balance equation is taken to be

$$V \frac{d\bar{n}_+}{dt} = K_{\text{iz}} n_g n_{e0} V - K_{\text{rec}} n_{-0} n_{+0} V_{\text{rec}} - h_l n_{+0} u_B A \quad (2.28)$$

where $A = 2\pi R^2 + 2\pi R \cdot 2l_p$. Two approximations are made in choosing the particle loss to the walls in (2.28) to be $h_l n_{+0} u_B A$. First, by taking the total area of the end walls to be $2\pi R^2$, rather than some reduced effective area due to the parabolic portion (2.16) of the radial density profile, we somewhat overestimate the wall loss. Second, we assume the same wall loss factor for the circumferential wall area $2\pi RL$ as for the end walls, consistent with a previous approximate calculation [18]. The wall loss factor h_R for the circumferential wall of a finite cylinder electronegative discharge has not been calculated exactly, but Godyak [1] gives the estimate $h_R = 0.8 / (4 + R/\lambda_+)^{1/2}$ for an infinitely long, cylindrical electropositive discharge, which does not differ much from the slab geometry result h_{l0} in (2.2). Again, this difference is not important if the central EN region is large.

The right hand sides of (2.27) and (2.28), including V_{rec} and h_l , are explicitly functions of the peak quantities α_0 and n_{e0} , whereas the time derivatives on the left hand

sides are in terms of average quantities. Given the average quantities at any moment in time, the peak quantities are obtained from

$$n_{e0} = \bar{n}_+ - \bar{n}_- \quad (2.29)$$

$$\alpha_0 V_-(\alpha_0, n_{e0}) = \bar{\alpha} V \quad (2.30)$$

where $\bar{\alpha} \equiv \bar{n}_- / n_{e0}$ is the average electronegativity. Equation (2.30) implicitly gives α_0 as a function of $\bar{\alpha}$. Since α_0 is a monotonic function of $\bar{\alpha}$, this equation can be easily solved numerically. Hence, the right hand sides of (2.27) and (2.28) can be evaluated.

2.2.3 Neutral Dynamics

Neutral excited states and radicals are considered here to be created mainly by electron excitation and/or dissociation processes, and lost mainly by diffusion to the walls, which have a sticking probability γ_A . Within our model of a uniform electron density, we employ the same approximation that is used for the positive ion density, with $L \ll 2R$, that a diffusion equation in z alone determines the axial profile of the neutral density n_A

$$-D_A \frac{d^2 n_A}{dz^2} = K_A n_g n_{e0} \quad (2.31)$$

where D_A is the neutral diffusion coefficient and K_A is a rate coefficient. Equation (2.31) has a parabolic solution

$$n_A = n_{A0} \left(1 - \frac{z^2}{d^2} \right) \quad (2.32)$$

where d is a parabolic scale length. The boundary condition at $z = l_p$ is [26]

$$\Gamma_A(l_p) = -D_A \left(\frac{dn_A}{dz} \right)_{l_p} = \frac{\gamma_A}{2(2 - \gamma_A)} n_A(l_p) \bar{v}_A \quad (2.33)$$

with $\bar{v}_A = (8kT_A/\pi M_A)^{1/2}$ the mean speed, and γ_A is a wall recombination coefficient.

Substituting (2.32) into (2.33) determines d

$$d^2 = l_p^2 + 4D_A l_p (2 - \gamma_A) / \gamma_A \bar{v}_A \quad (2.34)$$

From (2.33), the loss flux can then be written as

$$\Gamma_A = h_A \cdot \frac{1}{4} \frac{2\gamma_A}{2 - \gamma_A} n_{A0} \bar{v}_A \quad (2.35)$$

with an edge-to-center density ratio

$$h_A \equiv \frac{n_A(l_p)}{n_{A0}} = \frac{1}{1 + \frac{l_p \bar{v}_A \gamma_A}{4D_A(2 - \gamma_A)}} \quad (2.36)$$

Since the density distribution is parabolic, the average density is

$$\bar{n}_A = \left[\frac{2}{3} + \frac{1}{3} \left(1 - \frac{l_p^2}{d^2} \right) \right] n_{A0} \quad (2.37)$$

To apply this result to our finite cylinder geometry, we make a similar assumption as for the negative ion density, that n_A has a parabolic profile in z given by (2.32) and a uniform profile in r for $r < R - l_p$, and that it has the same parabolic profiles in both r and z for $R - l_p < r < R$

$$n_A = n_{A0} \left(1 - \frac{z^2}{d^2} \right) \left(1 - \frac{(r - R + l_p)^2}{d^2} \right) \quad (2.38)$$

Integrating (2.32) over z and r for $r < R - l_p$ and (2.38) over z and r for $r > R - l_p$ gives the relation between peak and average densities

$$\bar{n}_A V = n_{A0} V_A \quad (2.39)$$

where

$$V_A = V \left(1 - \frac{1}{3} \frac{l_p^2}{d^2} \right) \left(1 - \frac{2}{3} \frac{l_p}{R} \frac{l_p^2}{d^2} + \frac{1}{6} \frac{l_p^2}{R^2} \frac{l_p^2}{d^2} \right) \quad (2.40)$$

is the effective volume for the neutrals.

The above formalism, for $2R > L$, is for the most common processing configurations. The inverse situation, with $2R < L$, can be developed in a manner quite similar to that presented here, with a radial loss factor h_R appearing in the wall loss expression, and various integrations being performed primarily over cylinders.

2.3 Model Equations and Solution Procedures

2.3.1 Energy Loss and Rate Coefficients

We assume seven species in the oxygen discharge: electrons, molecular oxygen in the ground state $O_2(^3\Sigma_g^-)$, metastable molecular oxygen $O_2^*(a^1\Delta_g)$, atomic oxygen in the ground state $O(^3P)$, positive ions O^+ and O_2^+ and the negative ion O^- . The reactions and rate coefficients assumed in the model are listed in Table 2.1. The choice of reactions and species is based on earlier modeling work where significantly more species and reactions were considered [17,27]. The rate coefficients for electron impact ionization of the oxygen atom [3], charge transfer [28], and electron impact ion-pair formation [2] are taken from the existing literature. For this work the other reaction rate coefficients have been revised from Gudmundsson's earlier work [27] and are discussed in Appendix A. The rate coefficients for electron impact collisions were calculated assuming a Maxwellian electron energy distribution and fit over an electron temperature range of

Reaction	Rate Coefficient (m ³ /s)	Source
e + O ₂ momentum transfer	$K_{el} = 4.7 \times 10^{-14} T_e^{0.5}$	[29,30]
e + O ₂ → O ₂ ⁺ + 2e	$K_{iz1} = 2.34 \times 10^{-15} T_e^{1.03} \exp(-12.29/T_e)$	[31]
e + O ₂ → O + O ⁻	$K_{att} = 1.07 \times 10^{-15} T_e^{-1.391} \exp(-6.26/T_e)$	[32]
e + O ₂ → O + O ⁺ + 2e	$K_{iz4} = 1.88 \times 10^{-16} T_e^{1.699} \exp(-16.81/T_e)$	[31]
e + O ₂ → O ⁺ + O ⁻ + e	$K_{iz3} = 7.1 \times 10^{-17} T_e^{0.5} \exp(-17/T_e)$	[2]
e + O ₂ → 2O + e	$K_{diss} = 6.86 \times 10^{-15} \exp(-6.29/T_e)$	[29,30]
e + O ₂ → O + O [*] + e	$K_{diss} = 3.49 \times 10^{-14} \exp(-5.92/T_e)$	[29,30]
e + O → O ⁺ + 2e	$K_{iz2} = 9.0 \times 10^{-15} T_e^{0.7} \exp(-13.6/T_e)$	[3]
e + O ₂ ⁺ → 2O	$K_{ei} = 2.2 \times 10^{-14} T_e^{-1/2}$	[27]
O ⁻ + O → O ₂ + e	$K_{det} = 1.6 \times 10^{-16}$	[33]
O ⁻ + O ₂ ⁺ → O + O ₂	$K_{rec} = 2.6 \times 10^{-14} (300/T_i)^{0.44}$	[27]
O ⁻ + O ₂ ⁺ → 3O	$K_{rec2} = 2.6 \times 10^{-14} (300/T_i)^{0.44}$	[27]
O ⁻ + O ⁺ → 2O	$K_{rec3} = 4.0 \times 10^{-14} (300/T_i)^{0.43}$	[27]
O ⁺ + O ₂ → O + O ₂ ⁺	$K_{ch} = 2.0 \times 10^{-17} (300/T_i)^{0.5}$	[28]
e + O ₂ → O ₂ [*] + e	$K_{ex} = 1.37 \times 10^{-15} \exp(-2.14/T_e)$	[29,30]
e + O ₂ [*] → O ₂ + e	$K_{deex} = 2.06 \times 10^{-15} \exp(-1.163/T_e)$	Detailed balancing
e + O ₂ [*] → O ₂ ⁺ + 2e	$K_{izm} = 2.34 \times 10^{-15} T_e^{1.03} \exp(-11.31/T_e)$	[31]
e + O ₂ [*] → O + O ⁻	$K_{attm} = 4.19 \times 10^{-15} T_e^{-1.376} \exp(-5.19/T_e)$	[32]
e + O ₂ [*] → 2O + e	$K_{dism} = 6.86 \times 10^{-15} \exp(-5.31/T_e)$	Threshold reduction
O ⁻ + O ₂ [*] → O ₂ + O + e	$K_{rec4} = 3.3 \times 10^{-17}$	[34]
O + wall → ½ O ₂	$\gamma_O = 0.5$, for $p \leq 10$ mTorr; = (0.43, 0.33, 0.27, 0.23, 0.2, 0.15, 0.13) for $p = (15, 25, 35, 40, 50, 60, 70)$ mTorr	[35]
O ₂ [*] + wall → O ₂	$\gamma_{O_2^*} = 0.007$	[36]

Notes. T_e in the range 1-7 eV; T_i in kelvins; O₂^{*} is a ¹Δ_g state; O^{*} is ¹D state.

Table 2.1. Basic Reaction Set for the Oxygen Discharge

1 - 7 eV.

The collisional energy loss per electron-ion pair created, $\mathcal{E}_c(T_e)$, is defined separately for O atoms and for O₂ molecules as

$$\mathcal{E}_c = \mathcal{E}_{iz} + \sum_i \mathcal{E}_{ex,i} \frac{K_{ex,i}}{K_{iz}} + \frac{K_{el}}{K_{iz}} \frac{3m_e}{m_i} T_e \quad (2.41)$$

where \mathcal{E}_{iz} is the ionization energy, $\mathcal{E}_{ex,i}$ is the threshold energy for the i -th excitation process, K_{iz} is the ionization rate coefficient, $K_{ex,i}$ is the rate coefficient for the i -th excited state and K_{el} is the elastic scattering rate coefficient. Thus the terms on the right hand side account for the loss of electron energy due to ionization, excitation, and elastic (polarization) scattering against neutral atoms. A more detailed discussion of the calculation of \mathcal{E}_c for oxygen atoms and oxygen molecules is given elsewhere [37,38].

The rate coefficient for elastic collisions of electrons with atomic oxygen is calculated from the elastic collision cross section taken from the theoretical calculations by Thomas and Nesbet [39] for $E < 2$ eV and from the review by Itikawa and Ichimura [40] for $E > 2$ eV. The excitation rate coefficients for atomic oxygen were calculated from the excitation cross sections given in the review by Laher and Gilmore [41] and are given in Table 2.2. The rate coefficients for the higher excited states of atomic oxygen are given by a rate coefficient K_{h^*} calculated from the total cross sections for excitation of atomic oxygen given by Laher and Gilmore [41] and subtracting the rate coefficients of all other reactions given in Table 2.2. The cross sections for the electron impact elastic scattering and excitation of molecular oxygen are taken from the dataset compiled by Phelps [42]. The excitation rate coefficients are listed in Table 2.3. We use an ion-neutral cross section of $\sigma_i = 7.5 \times 10^{-19}$ m² for both O⁺ and O₂⁺ ions [43], with $\lambda_i = (n_g \sigma_i)^{-1}$ the

Reaction	Threshold (eV)	Rate Coefficient (m ³ /s)
Non-Rydberg States		
$e + O(^3P) \rightarrow O(^1D) + e$	1.96	$K_{1D} = 4.54 \times 10^{-15} \exp(-2.36/T_e)$
$e + O(^3P) \rightarrow O(^1S) + e$	4.18	$K_{1S} = 7.86 \times 10^{-16} \exp(-4.489/T_e)$
$e + O(^3P) \rightarrow O(^3P^0) + e$	15.65	$K_{3P^0} = 2.53 \times 10^{-15} \exp(-17.34/T_e)$
Rydberg States		
$e + O(^3P) \rightarrow O(^5S^0) + e$	9.14	$K_{5S} = 9.67 \times 10^{-16} \exp(-9.97/T_e)$
$e + O(^3P) \rightarrow O(^3S^0) + e$	9.51	$K_{3S} = 3.89 \times 10^{-15} \exp(-9.75/T_e)$
$e + O(^3P) \rightarrow O^{h*} + e$	12.0	$K_{h*} = 4.31 \times 10^{-14} \exp(-18.59/T_e)$

Notes. T_e in the range 1-7 eV.

Table 2.2. Rate Coefficients for Excitation of Atomic Oxygen

Reaction	Threshold (eV)	Rate Coefficient (m ³ /s)
$e + O_2(r = 0) \rightarrow O_2(r > 0) + e$	0.02	$K_{rot} = 1.87 \times 10^{-17} \exp(-2.9055/T_e)$
$e + O_2(v = 0) \rightarrow O_2(v = 1) + e$	0.19	$K_{v=1} = 2.8 \times 10^{-15} \exp(-3.72/T_e)$
$e + O_2(v = 0) \rightarrow O_2(v = 2) + e$	0.38	$K_{v=2} = 1.28 \times 10^{-15} \exp(-3.67/T_e)$
$e + O_2(X^3\Sigma_g^-) \rightarrow O_2(a^1\Delta_g) + e$	0.977	$K_{a^1\Delta_g} = 1.37 \times 10^{-15} \exp(-2.14/T_e)$
$e + O_2(X^3\Sigma_g^-) \rightarrow O_2(b^1\Sigma_g^+) + e$	1.627	$K_{b^1\Sigma_g^+} = 3.24 \times 10^{-16} \exp(-2.218/T_e)$
$e + O_2(X^3\Sigma_g^-) \rightarrow O_2(ex1) + e$	4.5	$K_{ex1} = 1.13 \times 10^{-15} \exp(-3.94/T_e)$
$e + O_2(X^3\Sigma_g^-) \rightarrow O_2(dis1) + e$	6.0	$K_{dis1} = 6.86 \times 10^{-15} \exp(-6.29/T_e)$
$e + O_2(X^3\Sigma_g^-) \rightarrow O_2(dis2) + e$	8.4	$K_{dis2} = 3.49 \times 10^{-14} \exp(-5.92/T_e)$
$e + O_2(X^3\Sigma_g^-) \rightarrow O_2(dis3) + e$	9.97	$K_{dis3} = 1.44 \times 10^{-16} \exp(-17.25/T_e)$
$e + O_2(X^3\Sigma_g^-) \rightarrow O_2(ex2) + e$	14.7	$K_{ex2} = 1.13 \times 10^{-15} \exp(-18.35/T_e)$

Notes. T_e in the range 1-7 eV.

Table 2.3. Rate Coefficients for Excitation of Molecular Oxygen

ion-neutral mean free path.

2.3.2 Particle Balance Equations

Using the reaction rate coefficients listed in Table 2.1, differential equations of particle balance for the species in the oxygen discharge are listed in equation (2.42) - (2.47).

$$\begin{aligned} \frac{dn_{O_2}}{dt} = & \frac{Q}{V} + K_{\text{rec}} n_{O_2^+0} n_{O^-0} \frac{V_{\text{rec}}}{V} + K_{\text{det}} \bar{n}_{O^-} \bar{n}_O + K_{\text{deex}} n_{e0} \bar{n}_{O_2^*} + K_{\text{rec4}} \bar{n}_{O^-} \bar{n}_{O_2^*} \\ & - (K_{\text{iz1}} + K_{\text{att}} + K_{\text{diss}} + K_{\text{iz3}} + K_{\text{iz4}} + K_{\text{ex}}) n_{O_2} n_{e0} - K_{\text{ch}} \bar{n}_{O^+} n_{O_2} \\ & + \mathcal{V}_{O_2^+} n_{O_2^+0} + \mathcal{V}_{O_2^*} n_{O_2^*0} + \frac{1}{2} \mathcal{V}_O n_{O0} - K_{\text{pump}} n_{O_2} \end{aligned} \quad (2.42)$$

$$\begin{aligned} \frac{d\bar{n}_{O_2^+}}{dt} = & K_{\text{iz1}} n_{O_2} n_{e0} + K_{\text{izm}} \bar{n}_{O_2^*} n_{e0} + K_{\text{ch}} \bar{n}_{O^+} n_{O_2} - (K_{\text{rec}} + K_{\text{rec2}}) n_{O_2^+0} n_{O^-0} \frac{V_{\text{rec}}}{V} \\ & - K_{\text{ei}} n_{e0} \bar{n}_{O_2^+} - \mathcal{V}_{O_2^+} n_{O_2^+0} \end{aligned} \quad (2.43)$$

$$\begin{aligned} \frac{d\bar{n}_{O^+}}{dt} = & K_{\text{iz2}} \bar{n}_O n_{e0} + (K_{\text{iz3}} + K_{\text{iz4}}) n_{O_2} n_{e0} - K_{\text{rec3}} n_{O^+0} n_{O^-0} \frac{V_{\text{rec}}}{V} - K_{\text{ch}} \bar{n}_{O^+} n_{O_2} \\ & - \mathcal{V}_{O^+} n_{O^+0} \end{aligned} \quad (2.44)$$

$$\begin{aligned} \frac{d\bar{n}_{O^-}}{dt} = & (K_{\text{att}} + K_{\text{iz3}}) n_{O_2} n_{e0} + K_{\text{atm}} n_{O_2^*} n_{e0} - (K_{\text{rec}} + K_{\text{rec2}}) n_{O_2^+0} n_{O^-0} \frac{V_{\text{rec}}}{V} \\ & - K_{\text{rec3}} n_{O^+0} n_{O^-0} \frac{V_{\text{rec}}}{V} - K_{\text{det}} \bar{n}_O \bar{n}_{O^-} - K_{\text{rec4}} \bar{n}_{O^-} \bar{n}_{O_2^*} \end{aligned} \quad (2.45)$$

$$\begin{aligned} \frac{d\bar{n}_O}{dt} = & 2K_{\text{ei}} n_{e0} \bar{n}_{O_2^+} + (K_{\text{rec}} + 3K_{\text{rec2}}) n_{O_2^+0} n_{O^-0} \frac{V_{\text{rec}}}{V} + 2K_{\text{rec3}} n_{O^+0} n_{O^-0} \frac{V_{\text{rec}}}{V} \\ & + (2K_{\text{diss}} + K_{\text{att}} + K_{\text{iz4}}) n_{e0} n_{O_2} + K_{\text{ch}} \bar{n}_{O^+} n_{O_2} + K_{\text{rec4}} \bar{n}_{O^-} \bar{n}_{O_2^*} \\ & + (K_{\text{atm}} + 2K_{\text{dism}}) n_{e0} \bar{n}_{O_2^*} - K_{\text{iz2}} n_{e0} \bar{n}_O - K_{\text{det}} \bar{n}_{O^-} \bar{n}_O + \mathcal{V}_{O^+} n_{O^+0} \\ & - \mathcal{V}_O n_{O0} - K_{\text{pump}} \bar{n}_O \end{aligned} \quad (2.46)$$

$$\begin{aligned} \frac{d\bar{n}_{O_2^*}}{dt} = & K_{\text{ex}} n_{O_2} n_{e0} - (K_{\text{izm}} + K_{\text{atm}} + K_{\text{deex}} + K_{\text{dism}}) \bar{n}_{O_2^*} n_{e0} - K_{\text{rec4}} \bar{n}_{O_2^*} \bar{n}_{O^-} \\ & - \nu_{O_2^*} n_{O_2^*0} - K_{\text{pump}} \bar{n}_{O_2^*} \end{aligned} \quad (2.47)$$

The term Q in (2.42) refers to the flow rate of molecular oxygen into the chamber. K_{pump} is the pumping rate for the neutral species (O_2 , O and O_2^*). In (2.43) and (2.44), the wall loss rate of positive ions is denoted as ν_i ($i = O_2^+$ and O^+ respectively), which can be calculated as

$$\nu_i n_{i0} = \Gamma_i \frac{A}{V} = h_i n_{i0} u_{B,i} \frac{A}{V} \quad (2.48)$$

where $h_i = h_a + h_b + h_c$ and $u_{B,i} = (eT_e/M_i)^{1/2}$. The wall loss rate of neutral oxygen atoms is denoted as ν_O , which can be calculated as [26]

$$\nu_O n_{O0} = \Gamma_O(l_p) \frac{A}{V} = h_O \frac{1}{4} \frac{2\gamma_O}{2(2-\gamma_O)} n_{O0} \bar{v}_O \frac{A}{V} \quad (2.49)$$

with an edge-to-center density ratio

$$h_O \equiv \frac{n_O(l_p)}{n_{O0}} = \left[1 + \frac{l_p \bar{v}_O \gamma_O}{4D_O(2-\gamma_O)} \right]^{-1} \quad (2.50)$$

where the diffusion coefficient $D_O = (eT_g \lambda_i / M_O \bar{v}_O)$. In same way, the wall loss rate of metastable oxygen $O_2^*(^1\Delta_g)$ is expressed as $\nu_{O_2^*}$, which can be calculated as

$$\nu_{O_2^*} n_{O_2^*0} = \Gamma_{O_2^*}(l_p) \frac{A}{V} = h_{O_2^*} \frac{1}{4} \frac{2\gamma_{O_2^*}}{2(2-\gamma_{O_2^*})} n_{O_2^*0} \bar{v}_{O_2^*} \frac{A}{V} \quad (2.51)$$

with the edge-to-center density ratio

$$h_{O_2^*} \equiv \frac{n_{O_2^*}(l_p)}{n_{O_2^*0}} = \left[1 + \frac{l_p \bar{v}_{O_2^*} \gamma_{O_2^*}}{4D_{O_2^*}(2-\gamma_{O_2^*})} \right]^{-1} \quad (2.52)$$

where the diffusion coefficient $D_{O_2^*} = \left(eT_g \lambda_i / M_{O_2^*} \bar{v}_{O_2^*} \right)$. In (2.51) and (2.52), γ_O and $\gamma_{O_2^*}$ are the wall recombination coefficients for these species.

2.3.3 Energy Balance Equations

The differential equation of power balance can be written as

$$\begin{aligned} \frac{d}{dt} \left(\frac{3}{2} e n_{e0} T_e \right) = \frac{P_{\text{abs}}}{V} - (e \mathcal{E}_{c_{-O_2}} K_{iz1} n_{e0} n_{O_2} + e \mathcal{E}_{c_{-O}} K_{iz2} n_{e0} \bar{n}_O) \\ - e(\mathcal{E}_e + \mathcal{E}_{i_{-O_2^*}}) \mathcal{V}_{O_2^*} n_{O_2^*0} - e(\mathcal{E}_e + \mathcal{E}_{i_{-O^+}}) \mathcal{V}_{O^+} n_{O^+0} \end{aligned} \quad (2.53)$$

where $\mathcal{E}_{c_{-O_2}}$ and $\mathcal{E}_{c_{-O}}$ are the collisional energy loss per electron-ion pair created for the neutrals O_2 and O respectively, determined from the processes listed in Tables 2.2 and 2.3, and

$$\mathcal{E}_e + \mathcal{E}_i = 2T_e + \frac{T_e}{2} + \frac{T_e}{2} \ln \left(\frac{M_i}{2\pi m_e} \right) \quad (2.54)$$

is the energy lost to the wall per electron-ion pair. In (2.53), P_{abs} is the absorbed power, which can be constant in time for a steady power or periodically time-varying for a pulsed power discharge.

The equations (2.42)–(2.47) and (2.53) can be solved together, numerically, with appropriate initial values for each particle density and electron temperature, calculating the time-evolution of their values. For a steady power, each particle density and the electron temperature converge to a set of values, and the plasma approaches an equilibrium state. For pulsed power, the values oscillate with time as the driving power varies periodically. For this case, we calculate time-average values for the densities and electron temperature to compare the equilibrium values to those with steady power.

Chapter 3

Solutions for

Steady State Oxygen Discharges

3.1 Steady State Oxygen Discharge Results

First, we have applied the global model to a cylindrical oxygen discharge driven by steady (CW) power, in a stainless steel chamber with radius $R = 15$ cm and length $L = 30$ cm. We assume the flow rate of oxygen feedstock is 50 sccm, a neutral gas temperature of $T_g = 600$ K and the wall recombination coefficient for atomic oxygen γ_o which decreases from 0.5 to smaller values as the pressure increases [35] as listed in Table 2.1. For metastable molecules, we use $\gamma_{o_2^*} = 0.007$ [36]. The chamber pressure is varied from 1 mTorr to 100 mTorr for absorbed powers of 500, 1000, and 2000 W.

The electron temperature is shown versus the chamber pressure in figure 3.1, falling with increasing pressure and, as expected, almost independent of the absorbed power. The electron density dependence on the chamber pressure is shown in figure 3.2, decreasing with pressure, and increasing nearly linearly with increasing absorbed power as expected. The electron density decrease as the pressure increases at a constant power is due both to the increasing electronegativity and to higher collisional energy loss. Figure 3.3 shows the average negative ion density as a function of pressure for various absorbed

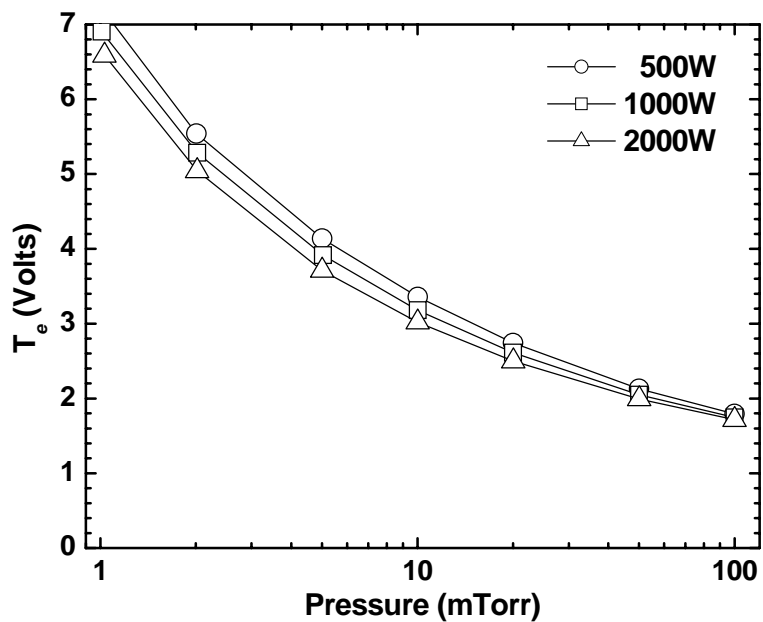


Figure 3.1. Electron temperature T_e versus pressure at 500, 1000 and 2000 W of absorbed power.

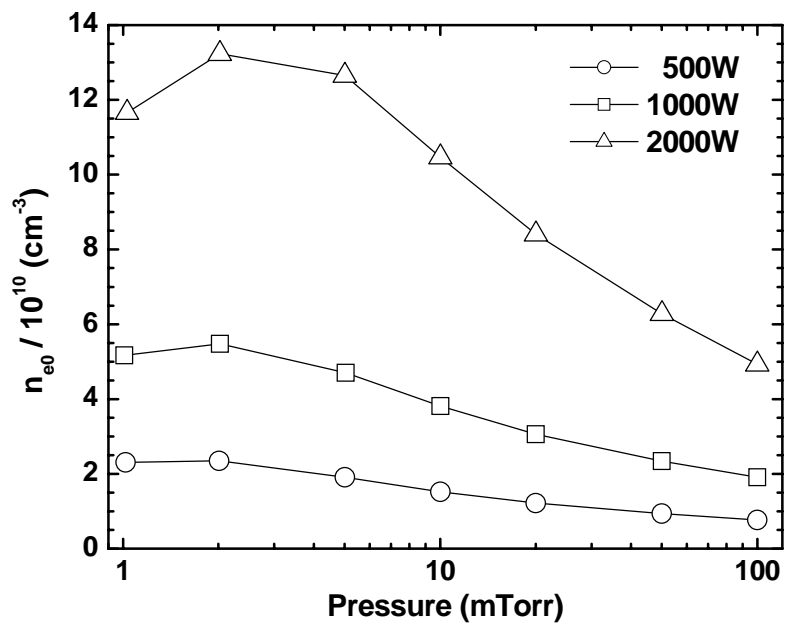


Figure 3.2. Core electron density n_{e0} versus pressure at 500, 1000 and 2000 W of absorbed power.

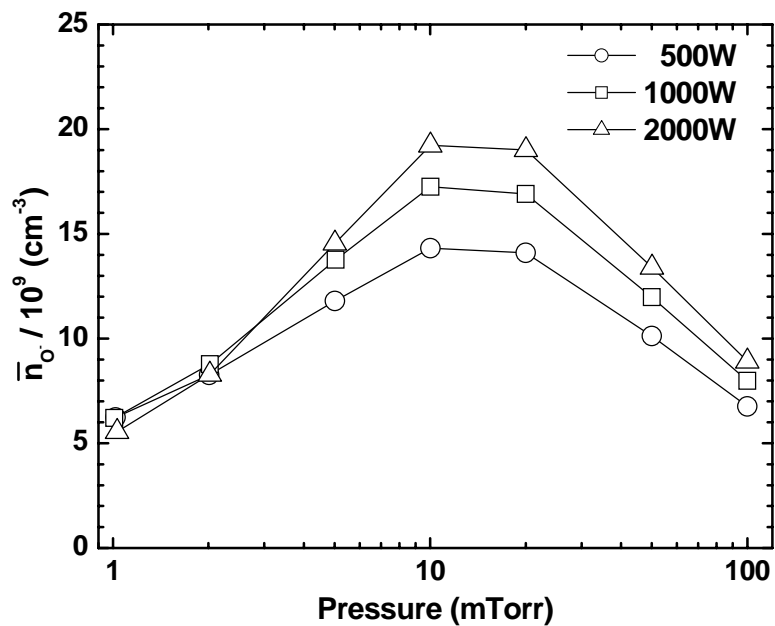


Figure 3.3. Average negative ion density \bar{n}_{o^-} versus pressure at 500, 1000 and 2000 W of absorbed power.

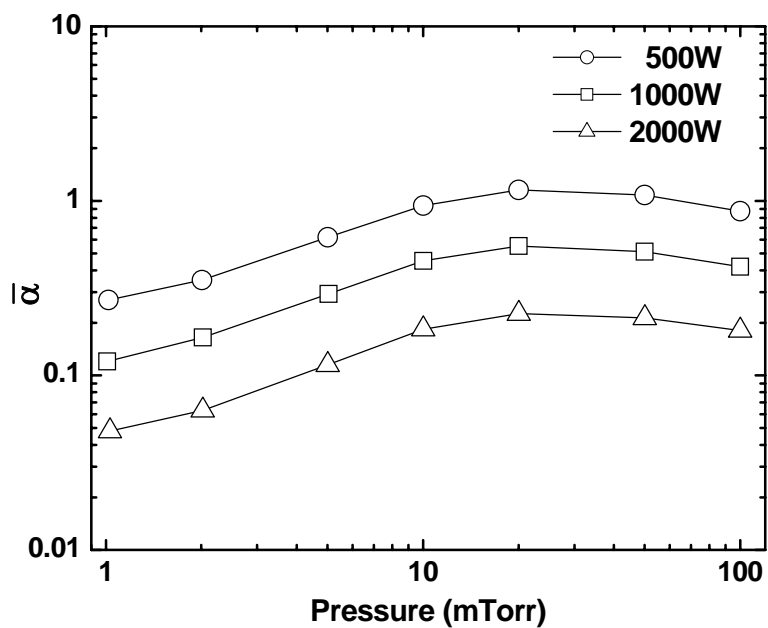


Figure 3.4. Average electronegativity $\bar{\alpha}$ versus pressure at 500, 1000 and 2000 W of absorbed power.

powers. At low pressures, the average negative ion density increases with increasing pressure due to the increased dissociative attachment. But at high pressures, the negative ion density decreases with increasing pressure because of the lower electron density. The average electronegativity $\bar{\alpha} \equiv \bar{n}_-/n_e$ as a function of pressure is shown in figure 3.4. The electronegativity decreases with increasing power and increases with increasing pressure in the low pressure regime, as expected theoretically [2].

Figure 3.5 shows the flux ratio of O neutrals to positive ions (Γ_O/Γ_+) versus pressure on a log-log scale for three discharge aspect ratios in a low power range, with higher powers giving similar scaling. The discharge aspect ratio $2R/L$ was varied as 1, 3 and 6 by varying L as 30, 10 and 5 cm respectively, and the absorbed power at each

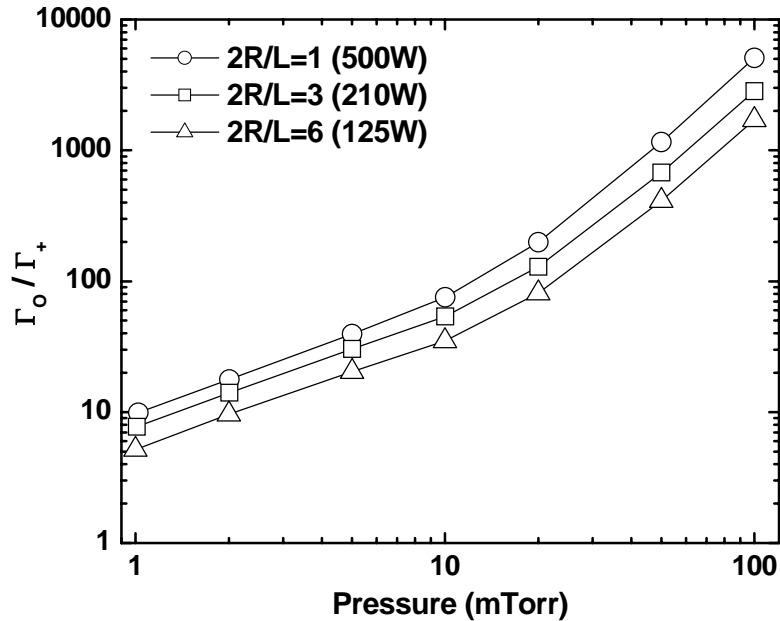


Figure 3.5. Flux ratio of O neutrals to positive ions (Γ_O/Γ_+) versus pressure for $2R/L = 1, 3$ and 6 in low power range. Here $R = 15$ cm and the absorbed power at each $2R/L$ was adjusted to yield similar values of Γ_+ on the wall.

aspect ratio was adjusted to yield similar values of positive ion flux (Γ_+) on the wall. In both power ranges and all pressures, the flux ratio decreases as the discharge aspect ratio increases. With an aspect ratio of 6, the flux ratio decreases about 65% compared to the flux ratio with an aspect ratio of 1. The flux ratio increases with increasing pressure up to 10 mTorr with a slope of ~ 0.8 for all the aspect ratios in both power ranges. For these log-log plots, this slope implies that the flux ratio Γ_o/Γ_+ is proportional to $p^{0.8}$. This can be qualitatively understood by the relation ([2], p 340)

$$\Gamma_o \propto n_g^{1-\mathcal{E}_{\text{diss}}/\mathcal{E}_{\text{iz}}} \quad (3.1)$$

where $\mathcal{E}_{\text{diss}}$ is the threshold energy for dissociation and \mathcal{E}_{iz} is the threshold energy for ionization. From Table 2.1, $\mathcal{E}_{\text{diss}} = 6.29$ V and $\mathcal{E}_{\text{iz}} = 12.29$ V, such that $1 - \mathcal{E}_{\text{diss}}/\mathcal{E}_{\text{iz}} \sim 0.5$ for our simulations. For $n_g \propto p$, $\Gamma_o \propto p^{0.5}$, which is comparable to $p^{0.8}$. With pressures higher than 10 mTorr, the slope becomes larger than 0.8 because of the decreasing wall recombination coefficient γ_o which increases atomic oxygen densities.

3.2 Comparison with Previous Results

We have two major tasks in comparing our CW improved global model results with previous results. We first show why the improved model is more consistent in application to both low and high α discharges than the simpler global models previously used. We then compare the new results to available experimental data.

For the first task we do not compare directly to previous published work, because different geometries were employed, and the most accurate reaction sets were not used.

Here we use the flatter geometry ($R = 15$ cm and $L = 5$ cm) often used numerically, but we use the present reaction set, with the simpler models. Key elements to the simpler models are the use of uniform densities for all species, and the use of the Godyak electropositive h_l and h_r factors modified to incorporate the lower diffusion rates for higher pressures [3,11], with the modified loss factors scaling as u_B^{-1} at high pressures. In one model [3], the electropositive Bohm velocity $u_{B0}(T_e)$ is used. In a second model [11], an electronegative Bohm velocity is used to incorporate the effect of a decreased Bohm velocity with increased electronegativity α_s at the sheath edge; however, the average $\bar{\alpha}$, rather than α_s , is used in this model. The comparisons are shown in figure 3.6. They indicate that the improved model has consistently higher losses at all pressures giving

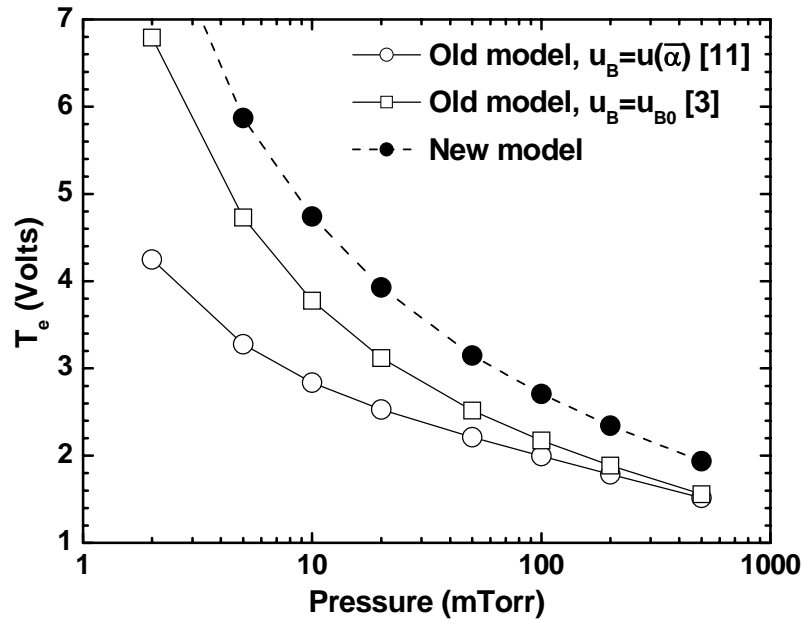


Figure 3.6 (a). Electron temperature T_e versus pressure for old model, old model with u_{B0} , and new model; $R = 15$ cm, $L = 5$ cm.

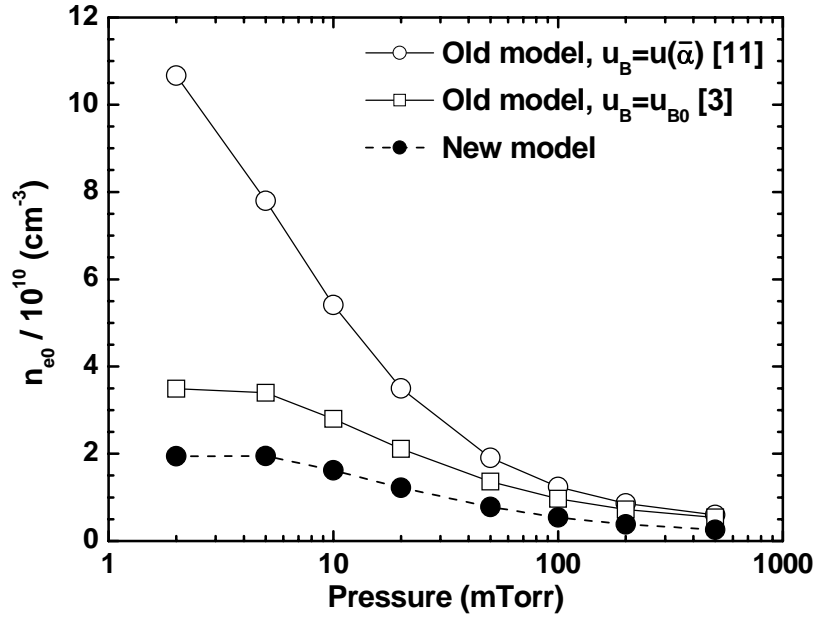


Figure 3.6 (b). Core electron density n_{e0} versus pressure for old model, old model with u_{B0} , and new model; $R = 15$ cm, $L = 5$ cm.

higher T_e values and lower n_e values. The largest discrepancies are at low pressure when the simpler global model employing a decreased Bohm velocity seriously underestimates the losses. At high pressure the two simpler global models converge due to a cancellation of the factor u_B , in the loss fluxes $u_B h_l$ and $u_B h_r$. The new model electron density is nearly a factor of two below the simpler models, which at higher pressure is principally due to the flattening of the central positive ion density, resulting in increasing edge gradients and therefore increasing loss.

3.3 Comparison with Experimental Results

Various experiments have been performed on inductive discharges in oxygen, measuring T_e , n_e , and other parameters. Usually, both pressure and power were varied, and the results compared to various models. The variations of n_e with P_{abs} are quite similar to that expected from our improved global model, i.e. roughly $n_e \propto P_{\text{abs}}$. The experimental variations of n_e with pressure, however, were different than the model predictions in that they indicated that $n_e \approx \text{constant}$ or somewhat increasing as the pressure is increased [16,18], rather than significantly falling with pressure predicted by the model. One such comparison is shown in figure 3.7 [44]. The decreasing n_e in the

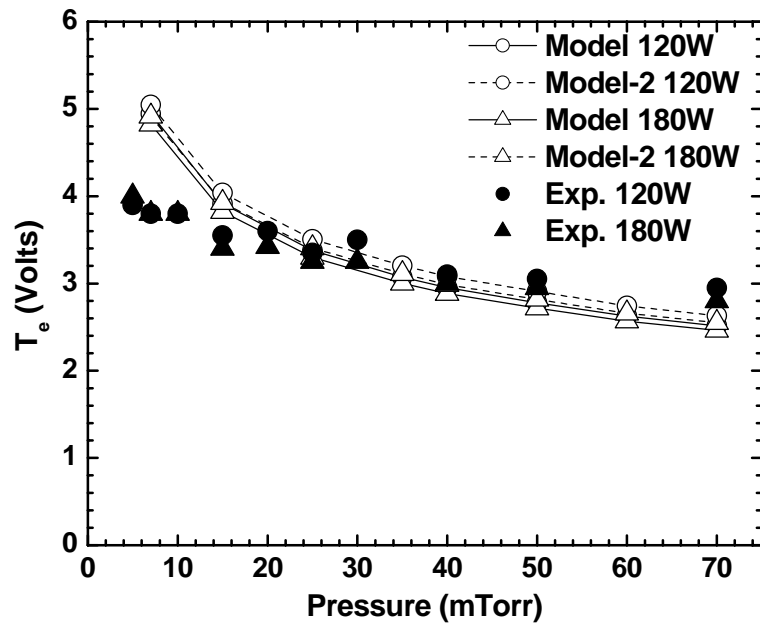


Figure 3.7 (a). Electron temperature T_e versus pressure comparison between models and experiment; $P_{\text{abs}} = 120, 180 \text{ W}$; $R = 8 \text{ cm}$, $L = 7.5 \text{ cm}$.

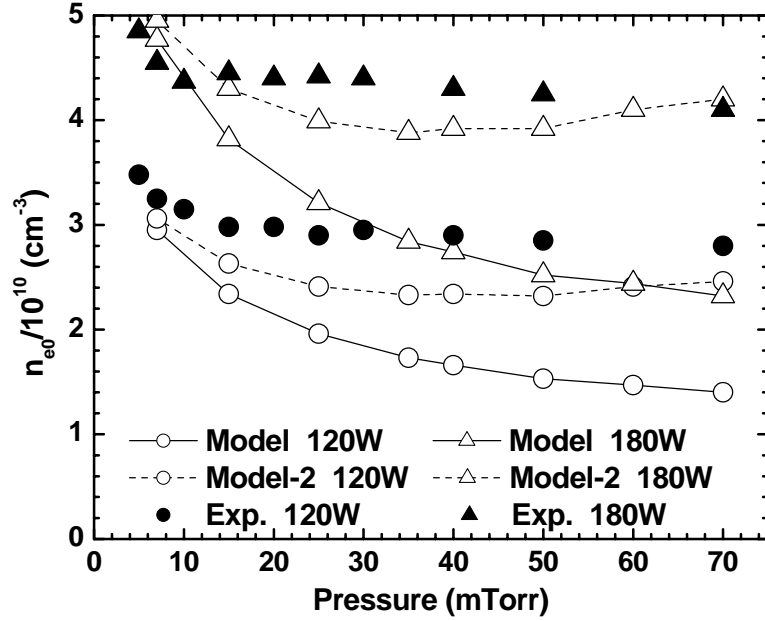


Figure 3.7 (b). Core electron density n_{e0} versus pressure comparison between models and experiment; $P_{\text{abs}} = 120, 180 \text{ W}$; $R = 8 \text{ cm}$, $L = 7.5 \text{ cm}$.

model results from T_e falling as the pressure increases to maintain ionization balance. For oxygen, \mathcal{E}_c given by (2.41) is a rapidly increasing function of decreasing T_e . Since the power losses scale as $\mathcal{E}_c n_{e0}$, n_{e0} decreases as \mathcal{E}_c increases. One explanation for the different n_{e0} variations with pressure is that experiments and fluid simulations [45] indicate an enhanced T_e near the heating coil of an inductive discharge, with T_e in the bulk plasma falling to lower values. The global model assumes a uniform T_e everywhere in the discharge. To explore this effect within the model, we can introduce an effective volume V_ε for ionization and energy losses through the ansatz

$$V_\varepsilon = V \cdot \frac{1}{\frac{L}{\lambda_\varepsilon} + 1} \quad (3.2)$$

where λ_ε is an average energy relaxation length

$$\lambda_\varepsilon = \frac{\bar{v}_e}{n_g \sqrt{3K_{\text{el}}K_{\text{inel}}}} \quad (3.3)$$

with $K_{\text{inel}} = K_{\text{ex}}$ (see Table 1). Using V_ε in place of V for the ionization and energy loss processes within the model yields the dashed lines in figure 3.7 (model-2). We see that a decreasing V_ε with increasing pressure (n_g) leads to nearly flat n_{e0} variation with pressure, as seen experimentally.

Chapter 4

Solutions for

Pulsed-power Oxygen Discharges

4.1 Introduction

We have also applied the improved global model to an oxygen discharge driven by pulsed-power excitation. The chamber pressure was set to 10 mTorr, where the plasma is considered to be weakly electronegative. An approximately square pulse waveform of the power modified by rise and fall times each approximates 50% of the pulse time of the power modulation was used, and the modulation period was varied. The effect of the duty-ratio (on-time/period) was examined by comparing duty ratios of 50% and 25%, together with the steady (CW) power case. The peak power values of the pulse for the pulsed conditions are varied such that the time-average powers are the same as that of the steady power. Two chamber geometries with aspect ratios $2R/L = 1$ and 6 were examined with $R = 15$ cm and $L = 30$ cm and 5 cm, respectively. The time-average powers for the two aspect ratios were adjusted to yield similar values of positive ion flux (Γ_+) on the wall. The same values as for the steady power case were used for the flow rate of the oxygen feedstock, the neutral gas temperature T_g , and the wall recombination coefficients

γ_O and $\gamma_{O_2^*}$. For this simulation we did not consider the reaction $e + O_2 \rightarrow O + O^* + e$ for the generation of $O^*(^1D)$.

4.2 Time-average Electron Temperature and Densities

Figures 4.1-4.3 show the time-average plasma parameters as a function of pulse period for two duty-ratios and for two discharge aspect ratios. The time-average electron temperature dependence on the pulse period for $2R/L = 1$ is shown in figure 4.1. For a very short pulse period, the plasma only responds to the average power, such that the time-average electron temperature is very close to that for the CW plasma. For longer

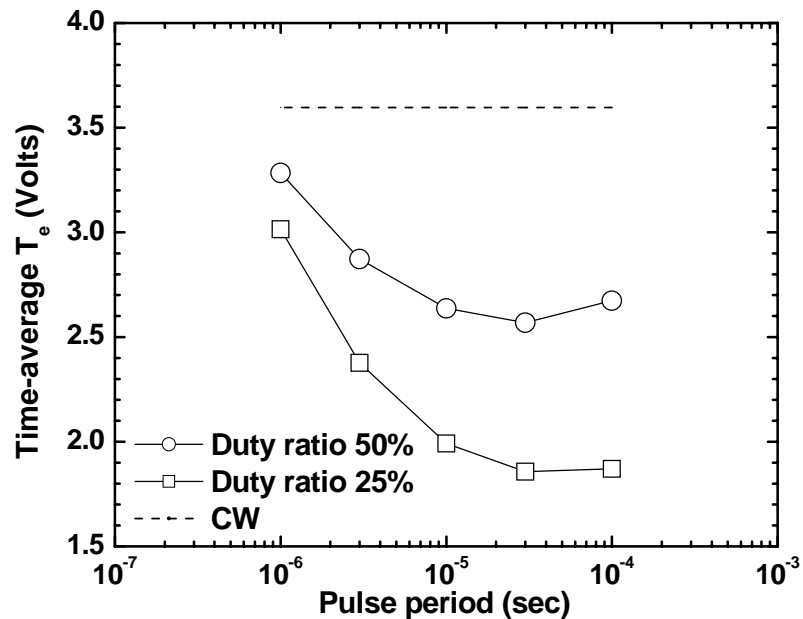


Figure 4.1. Time-averaged electron temperature T_e versus pulse period at $2R/L = 1$ for 50%, 25% duty ratio and for a CW plasma; $R = 15$ cm.

periods, the time-average electron temperature decreases with the period up to 30 μsec periods. For the smaller duty ratio, the time-average electron temperature decreases to a lower value because the temperature is low during most of the off-time. At 100 μsec , the time-average temperature slightly increases, because of a non-zero power during the fall-time of the pulsed power [46]. There is a similar variation of the time-average electron temperature for the higher aspect ratio, with the minimum occurring at a slightly lower pulse period.

Figure 4.2 shows the time-average electron densities as functions of pulse period, for $2R/L = 1$ in (a) and for $2R/L = 6$ in (b). All the curves have maxima as the pulse period is varied, with the peak value increasing as the duty ratio decreases, following

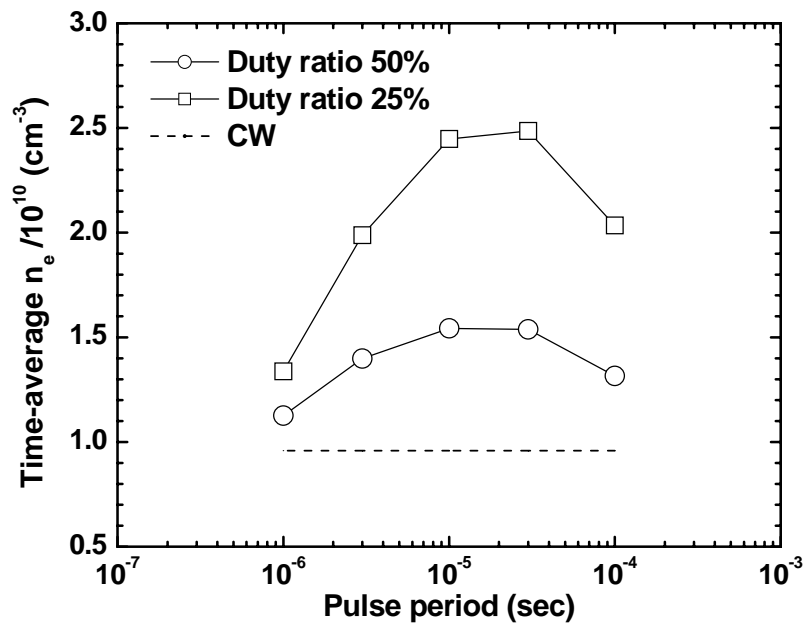


Figure 4.2 (a). Time-averaged electron density n_e versus pulse period at $2R/L = 1$ for 50%, 25% duty ratio and for a CW plasma; $R = 15$ cm.

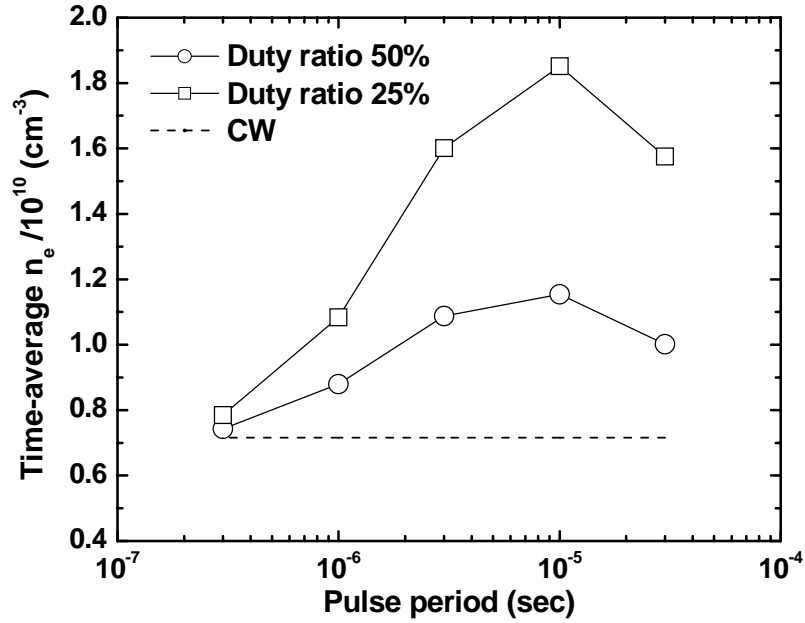


Figure 4.2 (b). Time-averaged electron density n_e versus pulse period at $2R/L = 6$ for 50%, 25% duty ratio and for a CW plasma; $R = 15$ cm.

roughly the decreasing temperature seen in figure 4.1. With 25% duty ratio, the maximum value of the time-average electron density is about 2.5 times higher than those of the CW plasma. At longer pulse periods the density decays during the long off-period, so leading to a decreasing average density.

4.3 Flux Ratio of Neutrals to Positive Ions

The relation between the flux ratio of O neutrals to positive ions (Γ_O/Γ_+) and the pulse period is shown in figure 4.3, for $2R/L = 1$ in (a) and for $2R/L = 6$ in (b). At a fixed duty-ratio, the ratio Γ_O/Γ_+ has a minimum value as the pulse period is varied, with the

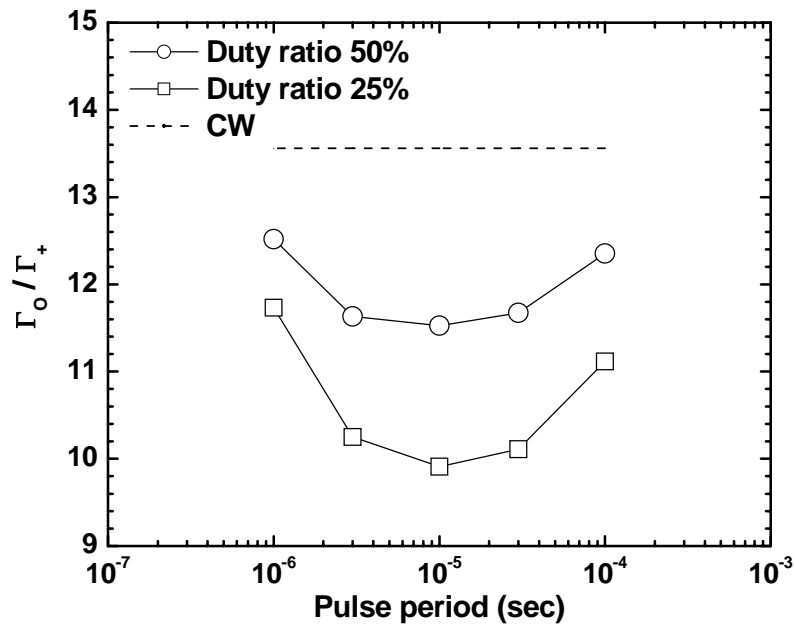


Figure 4.3 (a). Time-averaged flux ratio of O neutrals to positive ions (Γ_O/Γ_+) versus pulse period at $2R/L = 1$ for 50%, 25% duty ratio and for a CW plasma; $R = 15$ cm.

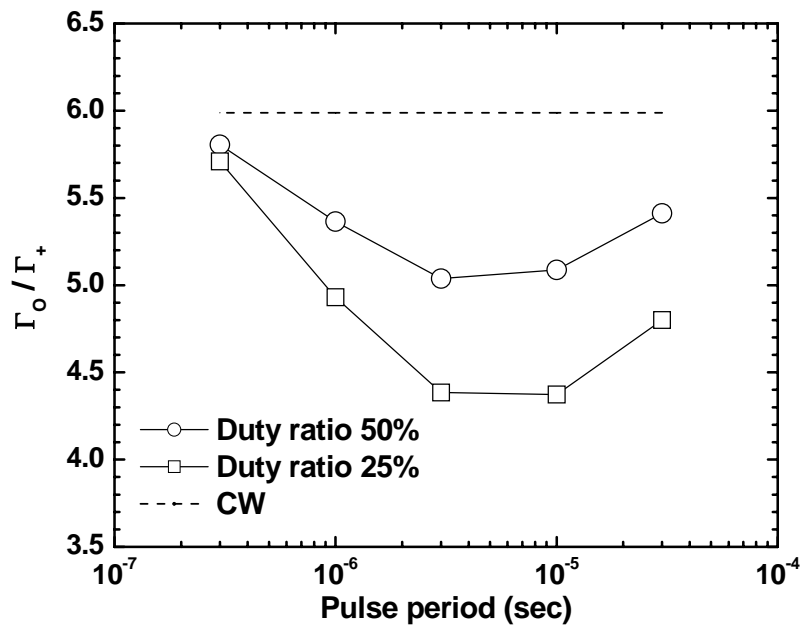


Figure 4.3 (b). Time-averaged flux ratio of O neutrals to positive ions (Γ_O/Γ_+) versus pulse period at $2R/L = 6$ for 50%, 25% duty ratio and for a CW plasma; $R = 15$ cm.

minimum value decreasing as the duty-ratio decreases. A partial explanation is that the ion density and therefore the ion flux increases with increasing n_e . For steady power (CW) discharges, increasing the aspect ratio $2R/L$ from 1 to 6 leads to a factor of 0.45 reduction in Γ_o/Γ_+ , again partially explained by the increase in n_e . For pulsed discharges at the pulse period of the minimum neutral density, a 25% duty-ratio pulse with 50% rise and fall time reduces Γ_o/Γ_+ by a factor of 0.75 compared to the CW plasma.

Chapter 5

Conclusions to Part I

An improved volume-averaged model of electronegative discharges has been developed, applicable to cylindrical plasmas of varying aspect ratio and over a broad range of electronegativities and pressures. The model takes into account the separation of the plasma into a central EN core surrounded by an electropositive penumbra, and allows for both a parabolic or a flattened core region, depending on the ratio of recombination flux to exiting flux. The spatial variations and spatial averaging are taken into account by introducing an additional length parameter and an additional equation to determine it. The methods follow those developed by Kimura *et al.* [18] but extend to include higher electronegativities and pressures, when the central core fills the entire plasma volume and/or flattens, and is therefore applicable over a wider parameter range.

A set of reaction rate coefficients, updated from previous model calculations, is determined for oxygen for the species O_2 , $O_2^*(a^1\Delta_g)$, O , O_2^+ , O^+ , and O^- , based on the latest published cross section sets and measurements. The reaction rates are summarized in Tables 2.1 - 2.3 with related discussion given in Appendix A.

The model is solved for both steady and pulsed-power excitation over a wide range of powers and pressures. The charged particle temperatures and densities, in steady state discharges, are determined as a function of pressure with both power and aspect ratio as parameters. The results are useful for generally understanding the behavior of

electronegative discharges. They are used to compare the improved global model with simpler global models and to validate the improved model by comparison with experiments.

The solution also yields the neutral/ion flux ratio Γ_o/Γ_+ as the discharge aspect ratio $2R/L$ and pulsed-power period and duty ratio (pulse on-time/pulse period) are varied, which is an important parameter to be minimized in processing applications. For steady discharges, increasing $2R/L$ from 1 to 6 leads to a factor of 0.45 reduction in Γ_o/Γ_+ . For pulsed discharges with a fixed duty ratio, Γ_o/Γ_+ is found to have a minimum with respect to pulse period. A 25% duty ratio pulse reduces Γ_o/Γ_+ by a factor of 0.75 compared to the steady-state case.

Part II

Ignition Conditions for Peripheral Plasma Connected to a Capacitive Discharge

Abstract

A configuration of both theoretical and practical interest is a capacitive discharge connected through a dielectric or metal slot to a peripheral grounded region. The configuration is used in commercial dual frequency capacitive discharges, where a dielectric slot surrounding the substrate separates the main plasma from the peripheral grounded pumping region. Ignition of the peripheral plasma produces effects such as poor matching and relaxation oscillations that are detrimental to processing performance. Discharge models are developed for diffusion and plasma maintenance in the slot, and plasma maintenance in the periphery. The theoretical predictions of ignition conditions as a function of voltage and pressure are compared with experimental results for a driving frequency of 27.12 MHz and a gap spacing of 0.635 cm connecting the two regions, giving good agreement. Instabilities associated with the loss of confinement in both the kilohertz and hertz frequency range are discovered, and a physical model for the kilohertz frequency range instability is proposed.

Chapter 6

Calculations of Ignition Conditions

6.1 Introduction

In operation of a commercial reactor, a peripheral plasma is sometimes formed, which produces detrimental effects on processing. This study is designed to understand the conditions for which peripheral ignition occurs, and therefore to determine the conditions required to confine the discharge to the central region. As shown in figure 6.1,

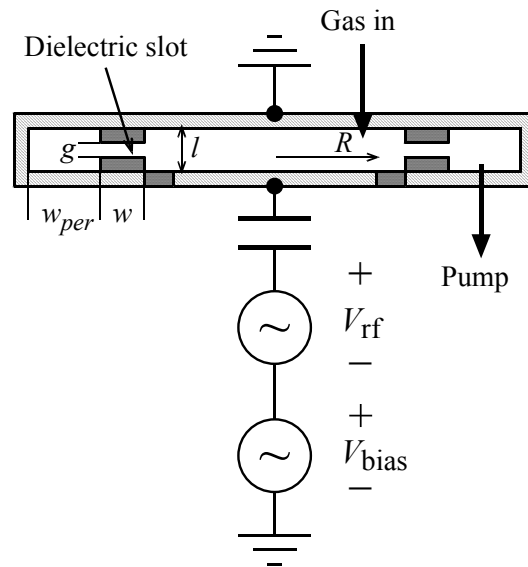


Figure 6.1. Confined plasma operation of a dual frequency capacitive discharge; the cylindrical central discharge chamber with powered electrode radius R and axial height l is connected through an annular dielectric slot of radial extent w and axial gap spacing g to a grounded peripheral region of radial extent w_{per} ; for this study $V_{bias}=0$.

the discharge is driven by a high frequency source of frequency ω and voltage V_{rf} in series with a low frequency source of frequency ω_b and voltage V_{bias} . Here we confine our analysis to a single high frequency ($V_{\text{bias}} = 0$). The main discharge, having plate separation l , is connected to a peripheral region of length w_{per} through an annular dielectric slot of gap length w and gap spacing g . The variable-gap slot is a flexible way of balancing required pumping speed with confinement of plasma to the central region. Because of the small pumping conductance of the slot, there can be a significant pressure gradient within the slot, which we can model using different average pressures in the slot and peripheral regions. The configuration in the figure is based on a commercial reactor, but the particular dimensions used are related to a research experiment that has been built to study the phenomena, which also has general theoretical interest for rf plasma diffusion in slots, and for plasma ignition in grounded regions far from an rf driving electrode.

The parameters of the experiment have a central discharge powered electrode of $R = 6.35$ cm (2.5 in) and a ground electrode up to the slot of $R_g = 8.9$ cm (3.5 in), with the 2.54 cm (1 in) gap between the powered electrode and the lower grounded electrode insulated with a quartz dielectric (see figure 6.1). The axial separation of the powered and upper grounded electrode is $l = 2.54$ cm, the slot length is $w = 3.8$ cm, and the grounded peripheral length is $w_{\text{per}} = 5.1$ cm. The separation of the dielectric spacers in the slot can be varied, but for the experiment reported here only the widest spacing of $g = 0.635$ cm is used. In the analysis we compare results in which either g or w are varied, and also consider the effect of replacing the slot dielectric rings with grounded metal rings.

A number of important issues determine ignition of a peripheral plasma.

(1) Plasma transport into a slot. In Sec. 6.2, we develop a transport model based on the following physics. The main discharge sets a uniform dc potential for plasma in the slot and for the plasma density at the slot entrance. Assuming diffusion of plasma into the slot and loss of plasma on the slot walls, then the density decays into the slot and the sheath thickness increases. When the sheath thickness grows to be approximately half of the gap spacing, then the plasma ‘pinches off’ inside the slot.

(2) Maintenance of a capacitive rf discharge. In Sec. 6.3, we determine the minimum rf voltage required to maintain a planar (one-dimensional) discharge at a given pressure. At low pressures, with a small resistive voltage component, the maintenance voltage is determined by the condition that the total thickness of the sheaths approaches closely the gap spacing, leading to a thin bulk plasma that cannot be sustained by ionization. The sheath thickness becomes large at either very low or very high rf voltages, yielding a double-valued maintenance curve at a given pressure.

(3) Maintenance of a plasma discharge in a dielectric slot and in a peripheral grounded region, including two-dimensional effects of wave propagation, radial current flows, and voltage variations in the slot. Since the slot plasma is driven at one end (its inner radius) by the rf voltage of the main discharge plasma, with the top and bottom slot surfaces earthed through the quartz confinement rings, there is wave propagation and a large radial component of the rf current when a slot plasma is ignited. The radial current further increases when a peripheral plasma is also ignited, which draws its current through the slot. We determine the power absorption and the radial variation of the rf voltage under these conditions. With no slot plasma, the rf plasma voltage \tilde{V}_d of the main discharge capacitively couples through the slot to the periphery, which can ignite a

peripheral plasma. In Sec. 6.4 and 6.5, we incorporate these effects into a maintenance model, so that the results can be quantitatively compared with experimental results given in chapter 7.

6.2 Plasma Transport in the Slot

The main discharge sets a uniform dc plasma potential \bar{V} in the slot, and a plasma density n_0 at the slot entrance. Typically, \bar{V} can be hundreds of volts. As the plasma diffuses into the slot and is lost on the slot walls, the density decays, and the sheath thickness s , determined by a Child law, increases, until $s \approx g/2$, when the plasma ‘pinches off’ inside the slot. We can estimate the scaling of the plasma decay using the simplest (high pressure) rectangular coordinate diffusion model, neglecting ionization in the slot, to obtain the diffusion equation

$$-D_a \nabla^2 n = 0, \quad (6.1)$$

where D_a is the ambipolar diffusion coefficient, $n(x, z)$ is the density in the slot, and x corresponds to the radial direction with $x = 0$ at the slot entrance. Taking $n = n_0$ at $x = 0$ and approximating $n = 0$ at $z = \pm g/2$, (6.1) has a fundamental diffusion mode solution

$$n = \frac{4n_0}{\pi} \cos\left(\frac{\pi z}{g}\right) \exp\left(-\frac{\pi x}{g}\right) \quad (6.2)$$

which gives the exponential decay length $\Lambda = g/\pi$. We equate the ion current flow to the slot wall to the limiting current for a collisionless Child law to determine the sheath thickness s ,

$$eh_l n u_B = K_{\text{CL}} \varepsilon_0 \left(\frac{2e}{M} \right)^{1/2} \frac{\bar{V}^{3/2}}{s^2}, \quad (6.3)$$

where h_l is an edge-to-center density ratio, $K_{\text{CL}} \approx 0.82$ (see Table 6.1), and $u_B = (eT_e/M)^{1/2}$ is the Bohm velocity. Examining first the configuration in which the confinement rings are grounded conductors, not dielectrics, the dc voltage across each sheath in the slot is

$$\bar{V} = K_V \tilde{V}_d + 4.7T_e, \quad (6.4)$$

where $K_V \approx 0.83$ (see Table 6.1) and \tilde{V}_d is the rf voltage amplitude of the main discharge with respect to ground. The term $4.7T_e$ gives the floating potential across a dc sheath when the rf voltage across the sheath is near zero, and the factor K_V relates the rf voltages to the dc voltages ([2], p. 404). We take the condition for pinch-off that the two sheaths expand to fill the entire gap, $s = g/2$ at position $x = w_{\text{po}}$. At w_{po} , where the bulk plasma thickness within the slot vanishes, we use the (collisionless) Langmuir solution for the diffusion to estimate $h_l = 0.425$ ([2], p. 148). Setting $x = w_{\text{po}}$ in (6.2) and $s = g/2$ in (6.3),

Coefficient	Collisionless model	Collisional model
K_{CL}	0.82	$1.68 (\lambda_i/s_m)^{1/2}$
K_{stoc}	0.45	0.61
K_{cap}	1.23	1.52
$K_{\text{ohm,sh}}$	0.130	0.236
K_V	0.83	0.78

References: [2] section 11.2, [47]

Table 6.1. Coefficients for collisionless and collisional models

we can eliminate n to obtain

$$0.135en_0T_e^{1/2} \exp(-\pi w_{po}/g) g^2 = K_{CL} \sqrt{2\varepsilon_0} \bar{V}^{3/2}. \quad (6.5)$$

Solving for w_{po} , we obtain

$$w_{po} = \frac{g}{\pi} \ln \left[\frac{0.135e}{K_{CL} \sqrt{2\varepsilon_0}} \frac{g^2 T_e^{1/2} n_0}{\bar{V}^{3/2}} \right], \quad (6.6)$$

with \bar{V} given by (6.4). Equation (6.6) gives w_{po} as a function of the voltages, densities, and slot dimensions, and shows that the pinch-off length is proportional to the gap spacing g and depends weakly (logarithmically) on the other system parameters. For typical parameters $n_0 = 2 \times 10^{11} \text{ cm}^{-3}$, $\bar{V} = 100 \text{ V}$, and $T_e = 2 \text{ V}$ (at 50 mTorr), we find a pinch-off length $w_{po} \approx 0.7 \text{ cm}$ for an 0.5 cm gap spacing.

To make a quantitative calculation of the pinch-off length, we use the following more realistic assumptions for the diffusion.

(1) The slot voltage in the Child law is the voltage across the sheath between the plasma and the surface of the confinement ring. If the confinement rings are quartz insulators, as in the experiments, then there is a voltage divider that relates the slot plasma-to-earth voltage to the slot plasma-to-quartz surface voltage. Approximating the sheath to be a vacuum dielectric, we find

$$\bar{V} = K_v \tilde{V}_d \frac{s}{s + (l - g)/2\kappa_q} + 4.7T_e, \quad (6.7)$$

where κ_q is the dielectric constant of the quartz. We note that this reduces the voltage across the slot and consequently increases the pinch-off length w_{po} at a given voltage. Quantitatively, the change in length is 10 to 15 percent.

(2) A more general approach to the diffusion that is useful over a wider range of pressures equates the rate of change of the radial flux Γ_x to the local axial (along z) loss:

$$\frac{d}{dx}(\Gamma_x(x)d(x)) = -2n(x)h_l(x)u_B \quad (6.8)$$

with

$$h_l(x) \approx \frac{0.86}{(3 + d(x)/2\lambda_i)^{1/2}}, \quad (6.9)$$

the edge-to-center density ratio given by low pressure diffusion theory ([2], Eq. (5.3.13)), and with $d(x) = g - 2s(x)$ the bulk plasma thickness. For lower pressures, Γ_x depends in a nonlinear way on the density n ([2], Sec. 5.3):

$$\Gamma_x = n(x)u_{ix}(x) \approx \frac{2e\Gamma_e}{\pi M} \frac{\lambda_i}{\langle u_i \rangle} \frac{dn}{dx}, \quad (6.10)$$

where u_i is the (radial) diffusion velocity along the slot, and $\langle u_i \rangle \approx u_B/2$ is an average flow velocity over the axial cross section. We have evaluated this non-linear diffusion model in various approximations by integrating (6.8) and (6.10) along with the relations (6.3), (6.7), and (6.9), finding decay lengths larger than g/π by about 10 to 15 percent. The finite thickness of the sheath, and the variation of the sheath size with changing density are found to have minor effects on the decay length, because $d = g - 2s$ and $s \ll g$ over the high densities in most of the slot.

(3) At high pressures, the sheaths become collisional, such that the collisionless Child law is replaced with the collisional form (see Table 1). For $\lambda_i \ll g$, this results in a decreased pinch-off density, compared to the collisionless case, and therefore to a slightly increased pinch-off length, of 5 to 10 percent.

(4) Another physical quantity that leads to longer decay lengths is ionization within the slot. To calculate this effect, we examined the high pressure diffusion equation (6.1), except that we included the ionization

$$-D_a \nabla^2 n = \nu_{iz} n \quad (6.11)$$

where ν_{iz} is the ionization frequency of the main discharge. This equation was solved as in (6.2) by separation of variables, giving, with the same approximation as in (6.2) that $n = 0$ at $z = \pm g/2$, the decay length

$$\Lambda = \frac{g/\pi}{\left(1 - \nu_{iz} g^2 / D_a \pi^2\right)^{1/2}} \quad (6.12)$$

This results in 5 to 10 percent longer decay length than that obtained from (6.2) in the absence of ionization.

The conclusions are that for a slot length w exceeding the pinch-off length, typically about 1 cm for a gap spacing of 0.5 cm, diffusion of plasma from the main discharge into the slot is not sufficient to ignite a peripheral plasma. However, the diffusing plasma is highly conductive and carries the rf potential of the main discharge into the slot, thus increasing the capacitive coupling from the main discharge to the periphery. The increased coupling can lead to ignition of the peripheral plasma, provided that the maintenance condition for a peripheral discharge is met. The comparison of the high pressure model with the more complete analysis, using the collisionless Child law sheath, is given in figure 6.2. The results for the decay of the plasma density into the slot are shown for the high pressure diffusion model as the dotted line.

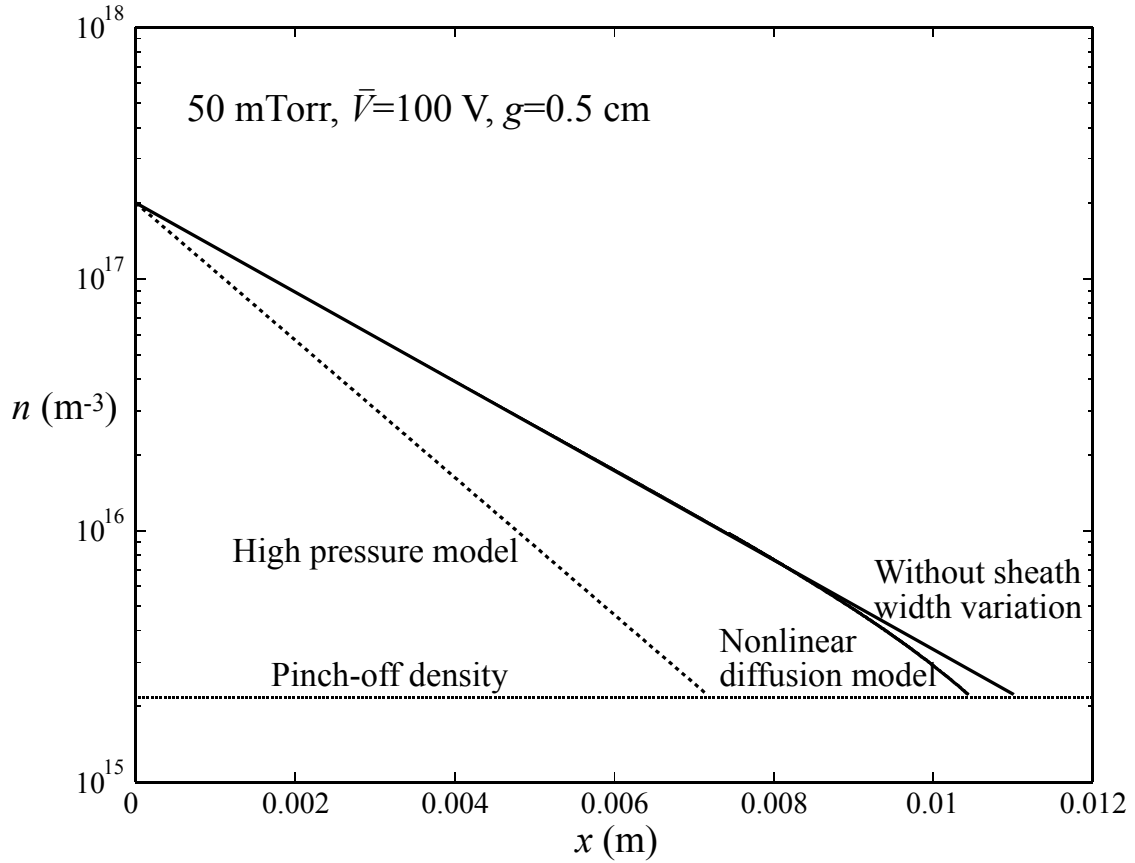


Figure 6.2. Plasma density in the slot versus position at 50 mTorr in argon, showing the pinch-off length w_{po} using various diffusion models.

6.3 Capacitive Discharge Maintenance

The condition on rf voltage versus pressure for which a capacitive rf discharge can just be maintained is known as the maintenance curve. The main feature of maintenance is that the total width of the sheaths approaches closely the gap spacing, leading to a thin bulk plasma and a rise in electron temperature. The ionization balance in the bulk or the electron power balance of the discharge is then lost, and the discharge extinguishes. The sheath becomes large at either very low or very high rf voltages,

yielding a double-valued maintenance curve. Some measurements of maintenance can be found in the literature for argon [48-51] and some molecular gases [52] at moderate pressures (below 1 Torr) over a limited range of discharge plate separations. Measurements of electrical characteristics, but not maintenance, over a wide range of pressures and voltages have been reported in argon [53].

Figure 6.3 illustrates the one-dimensional (1D) symmetric model that is used to determine the maintenance curves in a parallel plate device. The discharge region of thickness L is bounded by dielectrics each having a thickness $L_q/2$ and relative dielectric

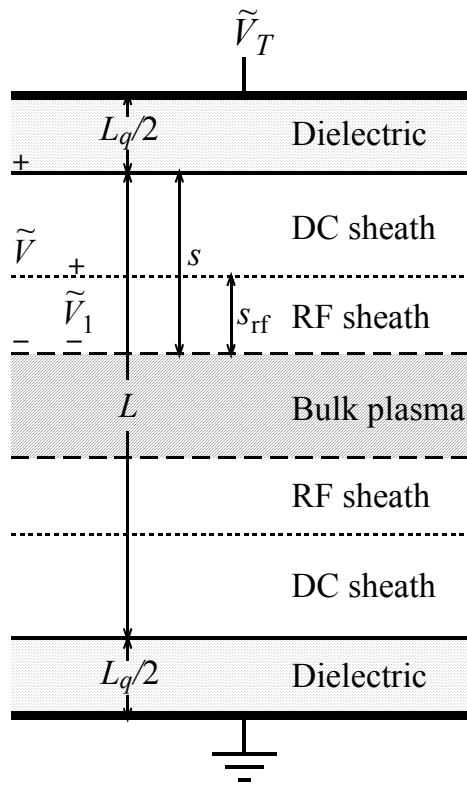


Figure 6.3. Symmetric one-dimensional capacitive discharge model; \tilde{V}_1 is the voltage drop across s_{rf} , the rf portion of the sheath, while \tilde{V} includes the additional rf voltage that drops across an additional dc sheath width arising from the additional dc potential; \tilde{V}_T also includes the voltage drop across the dielectric.

constant κ_q . The dielectric thickness can be set equal to zero to reproduce a simple capacitive discharge, which approximates a maintenance experiment described at the end of this section. Furthermore, the 1D model follows closely the standard models of a discharge that are well understood (see sections 11.2 and 11.3 of [2]).

At rf voltages describing the low voltage maintenance transition, some new physics enters into the description of rf discharges, beyond that included in the standard models, which must be included in the analysis: (1) A dc sheath voltage and dc sheath width exist in the absence of an rf voltage across the sheath (see figure 6.3). These dc effects are neglected in simple global models. We include these effects by using (6.4) to relate the dc and rf voltages. (2) Because the sheath includes both rf and dc parts, the rf voltage drop \tilde{V} across the entire sheath is not the same as the rf voltage drop \tilde{V}_1 across the rf-part of the sheath (see figure 6.3). In the discussion below, we give the relation between these two voltages. (3) In the standard model, the total voltage drop across the discharge thickness L is approximated by the reactive voltage drop across the sheaths alone. To determine the maintenance condition, the reactive voltage drop across the bulk plasma and the resistive voltage drops due to the electron and ion power absorption must be included in the analysis. (4) There is a transition from ambipolar to free diffusion of electrons in the bulk plasma (width $d = l - 2s$) when d becomes of order of four Debye lengths [54]. The transition increases the electron loss rate by a factor of $T_e/2T_i$, which is typically 20–100. This large increase in loss rate extinguishes the discharge. We have accounted for this effect by requiring that the bulk plasma be at least four Debye lengths thick.

Including these considerations, in the steady state, the production of electron-ion

Rate coefficients ($\text{m}^3 \text{s}^{-1}$)	Threshold energy (V)
$K_{\text{el}} = 2.236 \times 10^{-14} T_e^{1.609} \exp(0.0618 (\ln T_e)^2 - 0.117 (\ln T_e)^3)$	
$K_{\text{iz}} = 2.34 \times 10^{-14} T_e^{0.59} \exp(-17.44 / T_e)$	$\mathcal{E}_{\text{iz}} = 15.76$
$K_{\text{ex}} = 2.48 \times 10^{-14} T_e^{0.33} \exp(-12.78 / T_e)$	$\mathcal{E}_{\text{ex}} = 12.14$

Note: T_e is in the range of 1-7eV ([2], chapter 3).

Table 6.2. Rate coefficients and threshold energies for argon.

pairs in the volume by electron-neutral ionization is balanced by the loss of pairs to the walls (see [2] section 10.2 for more detailed explanations of the following equations):

$$K_{\text{iz}} n_g n d = 2 h_l n u_B \quad (6.13)$$

Here $K_{\text{iz}}(T_e)$ is the ionization rate coefficient (See Table 6.2), n_g is the neutral gas density, n is the central plasma density, $d = L - 2s$ is the quasineutral bulk plasma thickness, with s the maximum (rf + dc) sheath thickness, and h_l is the edge-to-center density ratio given by (6.9). It is well known that this particle (ion) balance relation sets the electron temperature T_e of the plasma, independent of the plasma density n_e . Typically $T_e \sim 2 - 5 \text{ eV}$, depending weakly on the pressure.

The corresponding electron power balance relation is

$$S_e = 2 e h_l n u_B (\mathcal{E}_c + \mathcal{E}'_e) \quad (6.14)$$

where S_e is the power per unit area absorbed by electrons from the rf field,

$$\mathcal{E}_c(T_e) = \mathcal{E}_{\text{iz}} + \mathcal{E}_{\text{ex}} K_{\text{ex}} / K_{\text{iz}} + 3(m/M) T_e K_{\text{el}} / K_{\text{iz}} \quad (6.15)$$

is the sum of the collisional electron energy losses from ionization, excitation, and elastic scattering per electron-ion pair created (typically $\mathcal{E}_c \sim 30 - 100 \text{ eV}$ for argon, depending on the pressure), and $\mathcal{E}'_e(T_e)$ is the electron kinetic energy lost from the plasma per

electron-ion pair created ($\mathcal{E}'_c \sim 6.8 T_e$ for argon). We see that the density is proportional to the electron power absorbed. There are three mechanisms for electron power absorption from the rf source (see [2], Chapter 11): Stochastic heating yields a time-average electron power absorption for each sheath

$$S_{\text{stoc}} = K_{\text{stoc}} \left(\frac{m}{e} \right)^{1/2} \varepsilon_0 \omega^2 T_e^{1/2} \tilde{V}_1. \quad (6.16)$$

Ohmic heating in the bulk plasma yields

$$S_{\text{ohm}} = K_{\text{ohm}} \frac{m}{2e} h_i \varepsilon_0 \omega^2 \nu_m d T_e^{1/2} \tilde{V}_1^{1/2}. \quad (6.17)$$

Ohmic heating in each sheath yields

$$S_{\text{ohm,sh}} = K_{\text{ohm,sh}} \frac{m}{2e} \varepsilon_0 \omega^2 \nu_m s \tilde{V}_1. \quad (6.18)$$

Here \tilde{V}_1 is the rf voltage across the rf-part of the sheath, and ν_m is the electron-neutral momentum transfer frequency. Summing these powers gives

$$S_e = 2S_{\text{stoc}} + 2S_{\text{ohm,sh}} + S_{\text{ohm}}. \quad (6.19)$$

The total power per unit area S_{abs} absorbed from the rf source includes both S_e and the ion power per unit area,

$$S_i = 2eh_i n u_B \mathcal{E}_i, \quad (6.20)$$

where $\mathcal{E}_i = \bar{V}$ is the dc voltage across each sheath, given by (6.4).

The rf current density flowing through the sheath can be written as

$$\tilde{J} = K_{\text{cap}} \frac{j\omega\varepsilon_0}{s_{\text{rf}}} \tilde{V}_1 = K_{\text{cap}} \frac{j\omega\varepsilon_0}{s} \tilde{V}. \quad (6.21)$$

The relation between \tilde{V}_1 and \tilde{V} can be found by noting that the electron powers (6.16)–(6.18) are functions of $|\tilde{J}|^2/n_s$, with $|\tilde{J}|^2/n_s \propto \tilde{V}_1^{1/2}$ in the standard model ([2], p. 404).

For example, the ohmic heating power in the bulk plasma is $S_{\text{ohm}} = \frac{1}{2} |\tilde{J}|^2 d / \sigma_{\text{dc}}$, with $\sigma_{\text{dc}} = e^2 n / m v_m$, yielding $S_{\text{ohm}} \propto h_i v_m d |\tilde{J}|^2 / n_s$. Eliminating s from the RHS of (6.21) by using the Child law (6.3), we obtain

$$\frac{|\tilde{J}|^2}{n_s} = K_{\text{cap}}^2 \omega^2 \varepsilon_0 \left(\frac{M}{2e} \right)^{1/2} \frac{u_B}{K_{\text{CL}} K_V^{3/2}} \frac{\tilde{V}^2}{(\tilde{V} + 4.7 T_e / K_V)^{3/2}}. \quad (6.22)$$

In the limit that $K_V \tilde{V} \gg 4.7 T_e$, the last (voltage-dependent) term in (6.22) reduces to the standard model result $\tilde{V}_1^{1/2}$. Therefore (6.22) generalizes the standard model result for $|\tilde{J}|^2/n_s$, from which we see that the rf voltage \tilde{V}_1 across the rf-part of the sheath is related to the total rf voltage \tilde{V} across the sheath by

$$\tilde{V}_1 = \frac{\tilde{V}^4}{(\tilde{V} + 4.7 T_e / K_V)^3}. \quad (6.23)$$

From the last two terms in (6.21), we also obtain the rf sheath thickness,

$$s_{\text{rf}} = s \left(\frac{\tilde{V}}{\tilde{V} + 4.7 T_e / K_V} \right)^3. \quad (6.24)$$

The effective resistance seen by the driving voltage source, accounting for stochastic heating, ohmic heating in the sheath, and ion energy losses, is given by

$$R_{\text{eff}} = 2 \frac{S_{\text{stoc}} + S_{\text{ohm,sh}} + S_i}{|\tilde{J}|^2}. \quad (6.25)$$

We account separately for the resistance of the bulk plasma using a complex κ_p , as given in (6.27) and (6.28), below. The total rf voltage V_T across the discharge is the sum of the voltages across the plasma and the dielectric (see figure 6.3),

$$\tilde{V}_T = \tilde{V}_{\text{pl}} + \tilde{V}_{\text{diel}} \quad (6.26)$$

where

$$\tilde{V}_{\text{pl}} = \frac{1}{j\omega\epsilon_0} \left(\frac{2s}{K_{\text{cap}}} + \frac{d}{\kappa_p} \right) \tilde{J} + R_{\text{eff}} \tilde{J} \quad (6.27)$$

and

$$\tilde{V}_{\text{diel}} = \frac{1}{j\omega\epsilon_0} \frac{L_q}{\kappa_q} \tilde{J} \quad (6.28)$$

with

$$\kappa_q = 1 - \frac{\omega_p^2}{\omega(\omega - j\nu_m)} \quad (6.29)$$

the bulk plasma dielectric constant, $\omega_p = (e^2 n / \epsilon_0 m)^{1/2}$ the plasma frequency and ν_m the electron-neutral collision frequency.

The model equations are numerically solved as follows: First we choose a vector of values for the sheath thickness s . Next, using $d = L - 2s$, we solve the particle balance (6.13) to determine T_e . Then we substitute S_e from (6.19) into the LHS of the electron power balance (6.14) and use the Child law (6.3) to eliminate the density in the RHS of (6.14). The resulting equation is a ninth-order polynomial equation for the variable $\sqrt{\tilde{V}}$. We find that for a given value of s , there are two (or zero) valid roots, which are the maximum and minimum real positive roots with $\sqrt{\tilde{V}} > \sqrt{4.7 T_e / K_v}$. Having determined

\tilde{V} , all other quantities, such as the powers, discharge current density \tilde{J} , and total voltage \tilde{V}_T , are evaluated. To find the maintenance voltage at a given pressure, we then determine the minimum (and maximum) rf voltage \tilde{V}_T for which a solution exists and for which the bulk plasma width exceeds a certain fixed number of Debye lengths, chosen (somewhat arbitrarily) to be $d > 4\lambda_{Ds}$. This constraint on the bulk plasma thickness does not affect the maintenance condition for most of the parameters of interest.

Figure 6.4 shows recent measurements of maintenance [48] (squares), along with the model results, for a symmetric capacitive discharge with the experimental parameters

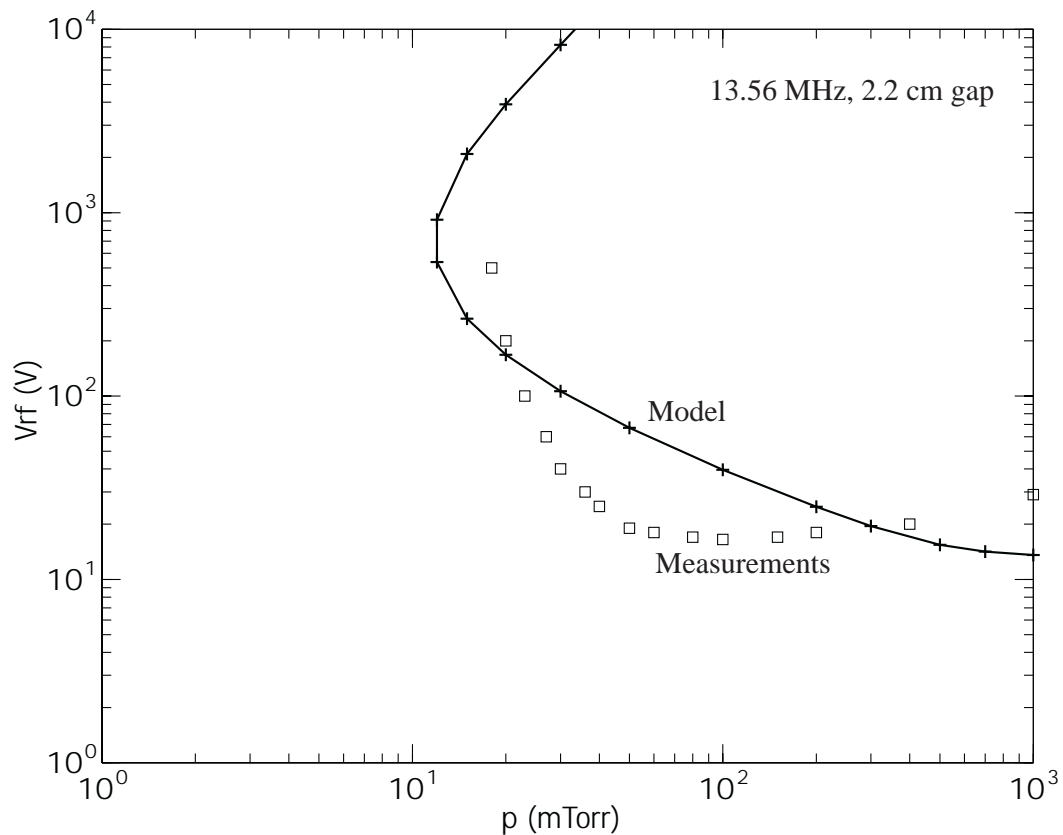


Figure 6.4. Measured and calculated maintenance voltage versus pressure for a 2.2 cm plate separation driven at 13.56 MHz in argon (no dielectric).

of $L = 2.2$ cm driven at 13.56 MHz. (There is no dielectric.) The model shows roughly the same form as the measurements for the lower branch of the maintenance curve, but with the minimum pressure for maintenance shifted from about 20 mTorr in the experiment to about 12 mTorr in the model. The upper branch is seen in the model, but not in the measurements which were limited to $V_{\text{rf}} < 500$ V. However, double-valued maintenance curves have been measured experimentally for molecular gases [52].

The α -to- γ transition can play a role in discharge maintenance [48,52]. This transition is due to a ‘Paschen-like’ breakdown of the sheath due to secondary emission from the discharge plates. When the Paschen voltage exceeds the dc voltage across the sheath, then the sheath ‘breaks down’, and the discharge enters the γ -mode. A calculation of the α -to- γ transition voltage versus pressure, indicated that it might be significant above 100 mTorr, but was not important in the pressure range to be examined experimentally. However, some residual differences between experiments and calculations, at lower pressures, are possibly due to multipactor effects [55], which are not captured in the model. The experiment is also not exactly one-dimensional as in the model.

6.4 Two Dimensional Effects on Discharge Maintenance

The mechanism of plasma breakdown and maintenance in a peripheral grounded region and a slot that connects the main discharge to the periphery is significantly more complicated than the 1D problem considered in the previous section. Since the slot and periphery walls are grounded, the voltage that drives a discharge in those regions is the rf

voltage \tilde{V}_d of the main discharge plasma with respect to ground. Because the slot is driven at one end (its inner radius) by \tilde{V}_d , with its top and bottom surfaces earthed through quartz or metal confinement rings, a large radial component of the rf current flows through the slot when it is ignited. The radial current further increases when a peripheral plasma is also ignited, which draws its current through the slot plasma. Furthermore, the two sheaths near the top and bottom earthed conductors see the same voltage, and therefore oscillate in-phase with each other, rather than 180° out-of-phase, as for the conventional discharge shown in figure 6.3.

To account for the in-phase motion, we can solve the conventional out-of-phase discharge model, with modifications to the ohmic power deposition discussed below, to determine a total voltage \tilde{V}_T . By symmetry, the main discharge plasma voltage for the in-phase situation is then $\tilde{V}_d = \tilde{V}_T/2$.

To determine the modification of the ohmic power for the in-phase situation, we examine the time-varying ohmic power dissipated in the slot

$$P_{\text{ohm}}(t) = \int_0^w dx \int_{-d(t)/2}^{d(t)/2} dz \frac{|\tilde{\mathbf{J}}(x, z, t)|^2}{\sigma_{\text{dc}}}, \quad (6.30)$$

where

$$\tilde{\mathbf{J}} = \hat{x} \tilde{J}_x(x, z, t) + \hat{z} \tilde{J}_z(x, z, t) \quad (6.31)$$

is the rf current flowing in the slot plasma, $d(t)$ is the time-varying bulk width of the plasma, and the conductivity σ_{dc} is assumed to be a constant. For a conventional discharge with out-of-phase sheaths, the radial current $\tilde{J}_x \equiv 0$ and the axial current $\tilde{J}_z = \tilde{J}_0(t)$, which is independent of x and z . We assume a sinusoidal time variation for

the current, $\tilde{J}_0 = J_0 \sin \omega t$, and we use a simple homogeneous density sheath model (neglecting the dc sheath component of the sheath thickness) to approximate the time-varying sheath motion. For the out-of-phase sheath oscillations, the two sheath thicknesses are

$$s_{1,2}(t) \approx \frac{s}{2}(1 \pm \cos \omega t). \quad (6.32)$$

We see from (6.32) that $s_1 + s_2 = s$ and $d(t) = L - s \equiv d_{\text{ave}} = \text{const.}$ Using these expressions to integrate (6.30), and averaging over an rf period, we obtain

$$P_{\text{ohm}} = \frac{1}{2} w d_{\text{ave}} \frac{J_0^2}{\sigma_{\text{dc}}}. \quad (6.33)$$

For in-phase excitation, we assume that $\tilde{J} \propto \tilde{E}$, with the electric field \tilde{E} a solution determined by solving Laplace's equation for the potential in the slot. Assuming open circuit boundary conditions $\tilde{J}_x = 0$ at $x = 0$, corresponding to no flow of current from the slot into the periphery, then the solution is

$$\tilde{J}_x = -2\tilde{J}_0(t) \frac{x}{d(t)}, \quad \tilde{J}_z = 2\tilde{J}_0(t) \frac{z}{d(t)} \quad (6.34)$$

Inserting these expressions into (6.30) and integrating yields

$$P_{\text{ohm}}(t) = \left[\frac{w d(t)}{3} + \frac{4w^3}{3d(t)} \right] \frac{\tilde{J}_0^2(t)}{\sigma_{\text{dc}}} \quad (6.35)$$

For a sinusoidal time variation of the current, we obtain from (6.32) (with $\pm \rightarrow +$ for both sheaths) that $d(t) = d_{\text{ave}} - s \cos \omega t$ for in-phase sheath motion, where, again, $d_{\text{ave}} = L - s$. Performing the time-averages using this $d(t)$ then yields

$$P_{\text{ohm}} = \frac{1}{2} \frac{\tilde{J}_0^2}{\sigma_{\text{dc}}} w d_{\text{ave}} \eta, \quad (6.36)$$

where

$$\eta = \frac{1}{3} + \frac{8w^2}{3s^2} \left(1 - \sqrt{1 - \frac{s^2}{d_{\text{ave}}^2}} \right) \equiv \eta_{\text{oc}}. \quad (6.37)$$

Comparing (6.36) together with (6.37) to (6.33), η_{oc} is the *ohmic enhancement factor* due to the geometry of the in-phase sheath motion, when the periphery draws no current. The second term in η_{oc} varies from $32w^2/3L^2$ as $s \rightarrow L/2$ (and $d_{\text{ave}} \rightarrow L/2$) to $4w^2/3L^2$ as $s \rightarrow 0$ (and $d_{\text{ave}} \rightarrow L$). The ohmic powers (6.17) and (6.18) in the model of Sec. 6.3 are multiplied by η_{oc} to determine the maintenance curve for the slot when there is no peripheral plasma.

When a peripheral plasma exists, then an additional current \tilde{I}_{per} is drawn through the slot, leading to an additional ohmic power dissipation. We assume that $\tilde{I}_{\text{per}} = j\omega C_{\text{per}} \tilde{V}_d$, with $C_{\text{per}} = K_{\text{cap}} \epsilon_0 l_{\text{eff}} / s_{\text{eff}}$, with l_{eff} and s_{eff} the effective width and sheath thickness of the peripheral plasma, chosen heuristically from the peripheral geometry. For example, for a periphery with $w_{\text{per}} \ll l$ (see Fig. 1), we choose $l_{\text{eff}} = l$ and s_{eff} to be a typical sheath width in an ignited peripheral plasma. The capacitance C_{per} is in parallel with the series combination $C_{\text{sl}} = 2K_{\text{cap}} \epsilon_0 w \kappa_q / (2\kappa_q s + K_{\text{cap}} l_q)$ of the sheath and quartz capacitances in the slot, with $l_q = l - g$ the total quartz thickness. Then the ratio of the peripheral and slot currents is

$$\frac{\tilde{I}_{\text{per}}}{\tilde{I}_0} = \frac{C_{\text{per}}}{C_{\text{sl}}} = \frac{l_{\text{eff}} (2s\kappa_q + K_{\text{cap}} l_q)}{2w\kappa_q s_{\text{eff}}}. \quad (6.38)$$

Using $\tilde{I}_{\text{per}} = \tilde{J}_{\text{xper}} d(t)$ and $\tilde{I}_0 = \tilde{J}_0 w$, we obtain in place of the \tilde{J}_x current in (6.34)

$$\tilde{J}_x = -\frac{\tilde{J}_0}{d(t)} \left(2x + \frac{C_{\text{per}}}{C_{\text{sl}}} w \right). \quad (6.39)$$

Using (6.39) in (6.30) and integrating to evaluate the ohmic power, and performing the time averages, we obtain (6.36) with

$$\eta = \eta_{\text{oc}} + 4 \frac{w^2}{s^2} \frac{C_{\text{per}}}{C_{\text{sl}}} \left(1 + \frac{1}{2} \frac{C_{\text{per}}}{C_{\text{sl}}} \right) \left(1 - \sqrt{1 - \frac{s^2}{d_{\text{ave}}^2}} \right) \equiv \eta_{\text{per}}. \quad (6.40)$$

The last term in (6.40) gives the enhancement in ohmic heating due to the current flow into the periphery. The ohmic powers (6.17) and (6.18) in the model of Sec. 6.3 are multiplied by η_{per} in (6.40) to determine the maintenance curve for the slot when a peripheral plasma is ignited.

We consider now the maintenance condition for plasma in the periphery when there is no plasma in the slot. Then the main discharge voltage \tilde{V}_d couples capacitively across the dielectric confinement rings to the periphery, igniting a conventional capacitive discharge in the periphery having two out-of-phase sheaths. Since the slot is thin, $g \ll l$, we assume that the entire distance l between the plates is filled with dielectric. We let the peripheral plasma voltage and current at the slot exit (taken as $x = 0$) be \tilde{V}_{pl} and \tilde{I}_{pl} , where \tilde{V}_{pl} is given by (6.27) and where $\tilde{I}_{\text{pl}} = \tilde{J}l$, with \tilde{J} given by (6.21). For given values of \tilde{V}_{pl} and \tilde{I}_{pl} , the voltage \tilde{V}_d at the slot entrance $x = w$ is determined from a two-dimensional solution of Laplace's equation within the dielectric. Considering the fundamental Fourier mode, the potential in the dielectric is

$$\Phi(x, z) = \cos \frac{\pi z}{l} \left(A_1 \cosh \frac{\pi x}{l} + A_2 \sinh \frac{\pi x}{l} \right). \quad (6.41)$$

At the slot exit, $\Phi(0,0) = A_1 = 4\tilde{V}_{\text{pl}}/\pi$. The factor of $4/\pi$ gives the fundamental mode amplitude for a voltage \tilde{V}_{pl} in the peripheral plasma that is uniform along z . Using $\mathbf{E} = -\nabla\Phi$, the x -component of the electric field at $x = 0$ is

$$E_x = -A_2 \frac{\pi}{l} \cos \frac{\pi z}{l}. \quad (6.42)$$

The displacement current flowing in the dielectric at the slot exit is

$$I_{\text{pl}} = \int_{-l/2}^{l/2} j\omega\epsilon_0\kappa_q A_2 \frac{\pi}{l} \cos \frac{\pi z}{l} dz \quad (6.43)$$

which yields $A_2 = I_{\text{pl}} / (2j\omega\epsilon_0\kappa_q)$. The voltage in the main discharge at the slot entrance is $\tilde{V}_d = \pi\Phi(w,0)/4$. Substituting A_1 and A_2 determined above into (6.41) to evaluate $\Phi(w,0)$, we find

$$\tilde{V}_d = \tilde{V}_{\text{pl}} \cosh \frac{\pi w}{l} + \frac{\pi}{4} \frac{l}{2j\omega\epsilon_0\kappa_q} \tilde{J} \sinh \frac{\pi w}{l}. \quad (6.44)$$

Equation (6.44) determines the main discharge plasma voltage when the peripheral plasma is ignited and there is no plasma in the slot.

If there is diffusion of plasma into the slot, but the slot is not ignited, then (6.44) is slightly modified. We assume a triangular spatial profile for the voltage variation from the center of the slot to the upper and lower grounded plates at the position of plasma pinch-off w_{po} . Then we find for the fundamental mode that $\tilde{V}_d = \pi^2\Phi(w-w_{\text{po}},0)/8$, replacing $\tilde{V}_d = \pi\Phi(w,0)/4$ in the preceding analysis, yielding

$$\tilde{V}_d = \frac{32}{\pi^3} \tilde{V}_{\text{pl}} \cosh \left(\pi \frac{w-w_{\text{po}}}{l} \right) + \frac{8}{\pi^2} \frac{l}{2j\omega\epsilon_0\kappa_q} \tilde{J} \sinh \left(\pi \frac{w-w_{\text{po}}}{l} \right). \quad (6.45)$$

Equation (6.45) determines the main discharge plasma voltage when the peripheral plasma is ignited and there is a diffusion ‘finger’ of plasma in the slot.

When both slot and periphery are ignited, then the peripheral region is directly connected to the main discharge by the ignited slot plasma. The rf voltage driving the peripheral plasma is then the main discharge voltage \tilde{V}_d , and the two sheaths at the upper and lower earthed surfaces of the periphery move in phase with each other. Therefore, we use an in-phase model with no capacitive voltage drops across dielectric surfaces to determine the maintenance condition of the periphery when the slot is ignited. For the preceding analysis in this section, we have assumed that the rf voltage is uniform along the slot plasma. We justify this assumption in Appendix B.

6.5 Maintenance Curves under Various Conditions

Incorporating the two-dimensional effects of previous section into the model of Sec. 6.3, we calculate the maintenance curves for the parameters used in the experiment: frequency $f = 27.12$ MHz, discharge plate separation $l = 2.54$ cm, gap spacing $g = 0.635$ cm, gap length $w = 3.8$ cm, periphery length $w_{\text{per}} = 5.1$ cm, and quartz dielectric constant $\kappa_q = 4.3$, with collisional sheaths. In figure 6.5, we show five curves for the following five conditions.

- (a) Slot maintenance with no ignited peripheral plasma. We use in-phase sheaths with η_{oc} given in (6.37), $L = g$ and $L_q = l - g$ (see Fig. 5 and Fig. 1), and \tilde{V}_T given in (6.26), with $\tilde{V}_d = \tilde{V}_T/2$.

- (b) Slot maintenance with an ignited peripheral plasma. We use in-phase sheaths with η_{per} given in (6.40), $L = g$, $L_q = l - g$, $w_{\text{eff}} = l$, $s_{\text{eff}} = 0.4l/\sqrt{2}$, and \tilde{V}_T given in (6.26), with $\tilde{V}_d = \tilde{V}_T/2$.
- (c) Periphery maintenance with no plasma in the slot. We use out-of-phase sheaths with $L = l/\sqrt{2}$ and $L_q = 0$, with \tilde{V}_d given by (6.44).
- (d) Periphery maintenance with a 1.27 cm diffusion plasma in the slot. We use out-of-phase sheaths with $L = l/\sqrt{2}$, $L_q = 0$, and $w_{\text{po}} = 1.27$ cm, with \tilde{V}_d given by (6.45).
- (e) Periphery maintenance with an ignited plasma in the slot. We use in-phase sheaths with η_{oc} given in (6.37), $L = l$, $L_q = 0$, $w = w_{\text{per}}$, and \tilde{V}_T given in (6.26), with $\tilde{V}_d = \tilde{V}_T/2$.

For example, at 100 mTorr, we see that the slot plasma will ignite at about 28 volts (curve a) and the periphery will ignite at about 500 volts (curve d). Hence, confinement is lost by ignition of the slot plasma at this pressure, since once the slot ignites, the periphery also ignites (curve e). However, for lower pressures, below about 14 mTorr, confinement is lost by ignition of the periphery (curve d), which then causes the slot to also ignite (curve b). For pressures below 10 mTorr, the periphery ignites without igniting the slot.

In figure 6.6, we show the same five curves for a reduced gap spacing $g = 0.3175$ cm and a correspondingly reduced pinch-off length, scaled from (6.6), of $w_{\text{po}} = 0.635$ cm. The thinner slot is much harder to ignite. The slot ignites at 90 V at 100 mTorr (curve a), which then causes the peripheral plasma to ignite (curve e).

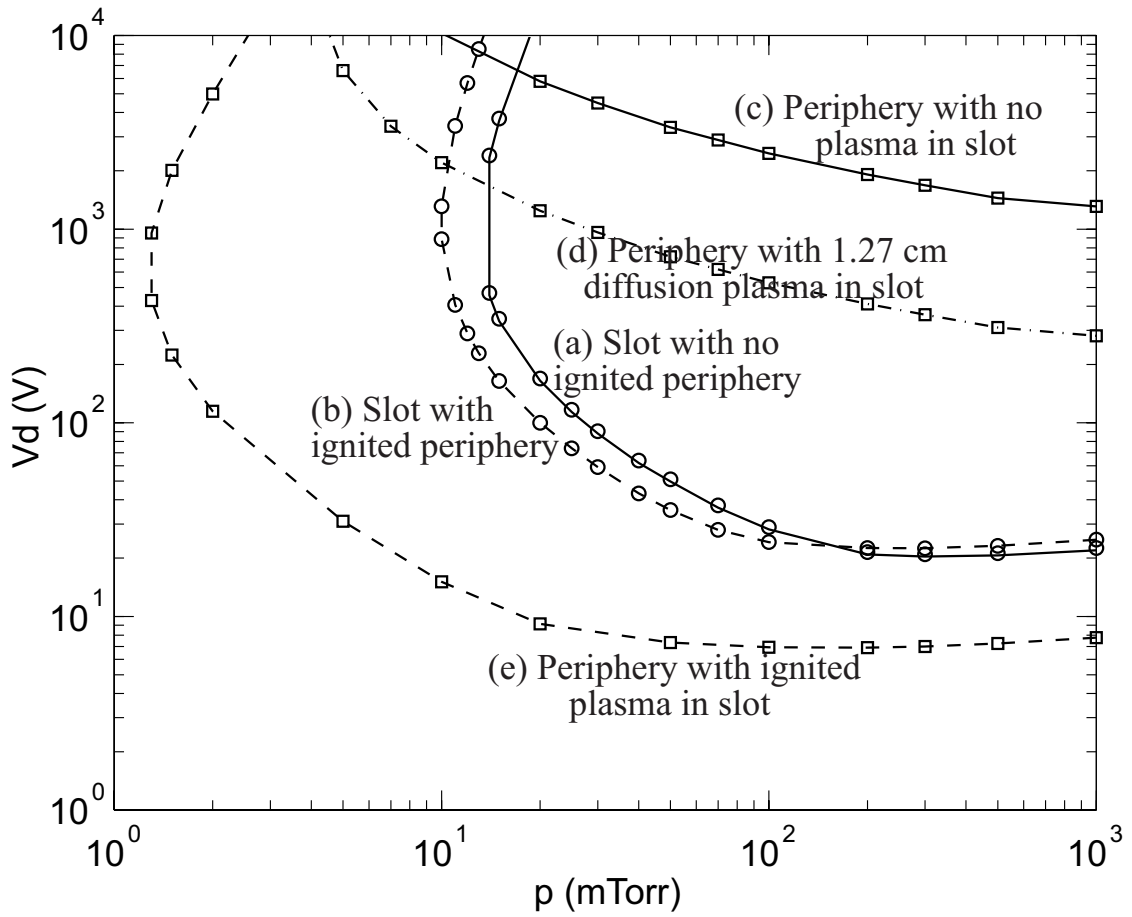


Figure 6.5. Maintenance curves for experimental conditions $f = 27.12$ MHz, $l = 2.54$ cm, $g = 0.635$ cm, $w = 3.8$ cm, and $w_{\text{per}} = 5.1$ cm; quartz dielectric confinement rings.

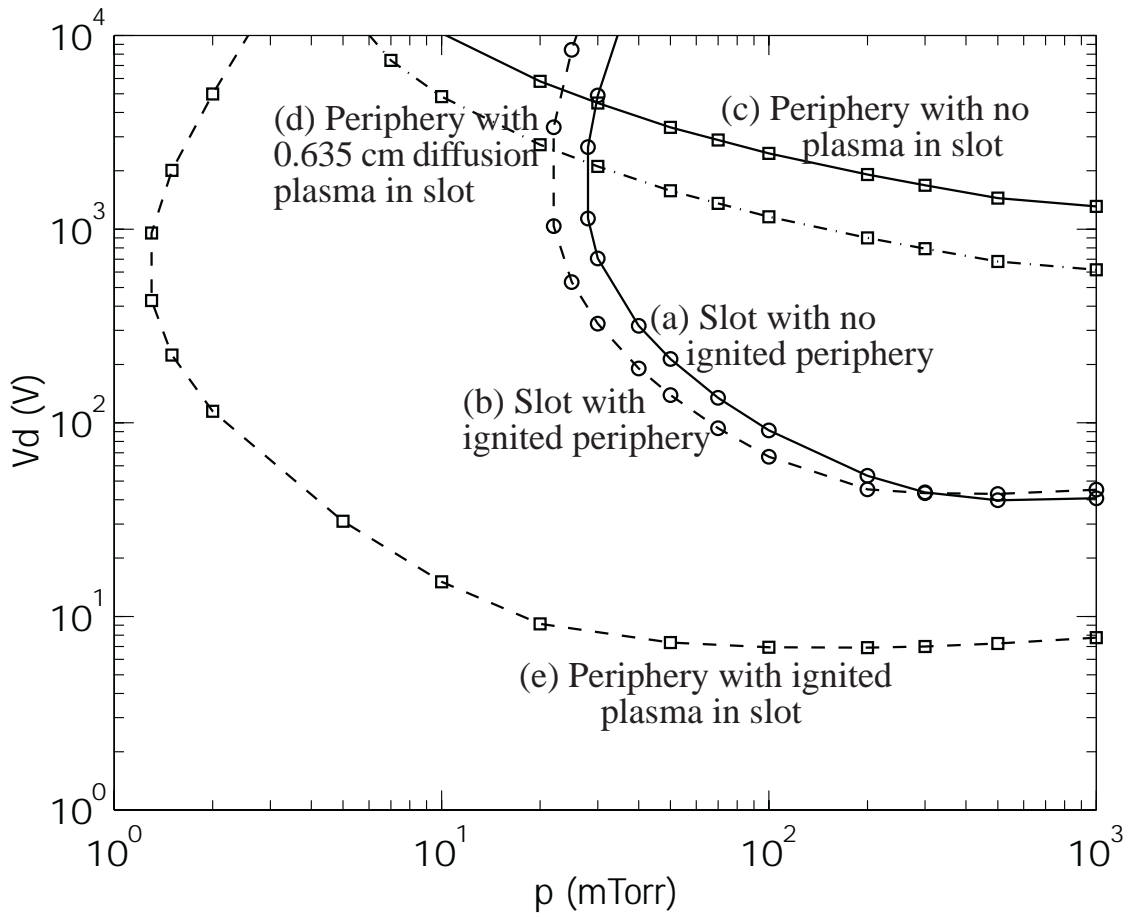


Figure 6.6. Maintenance curves for the same conditions as those of figure 6.5 but with $g = 0.3175$ cm.

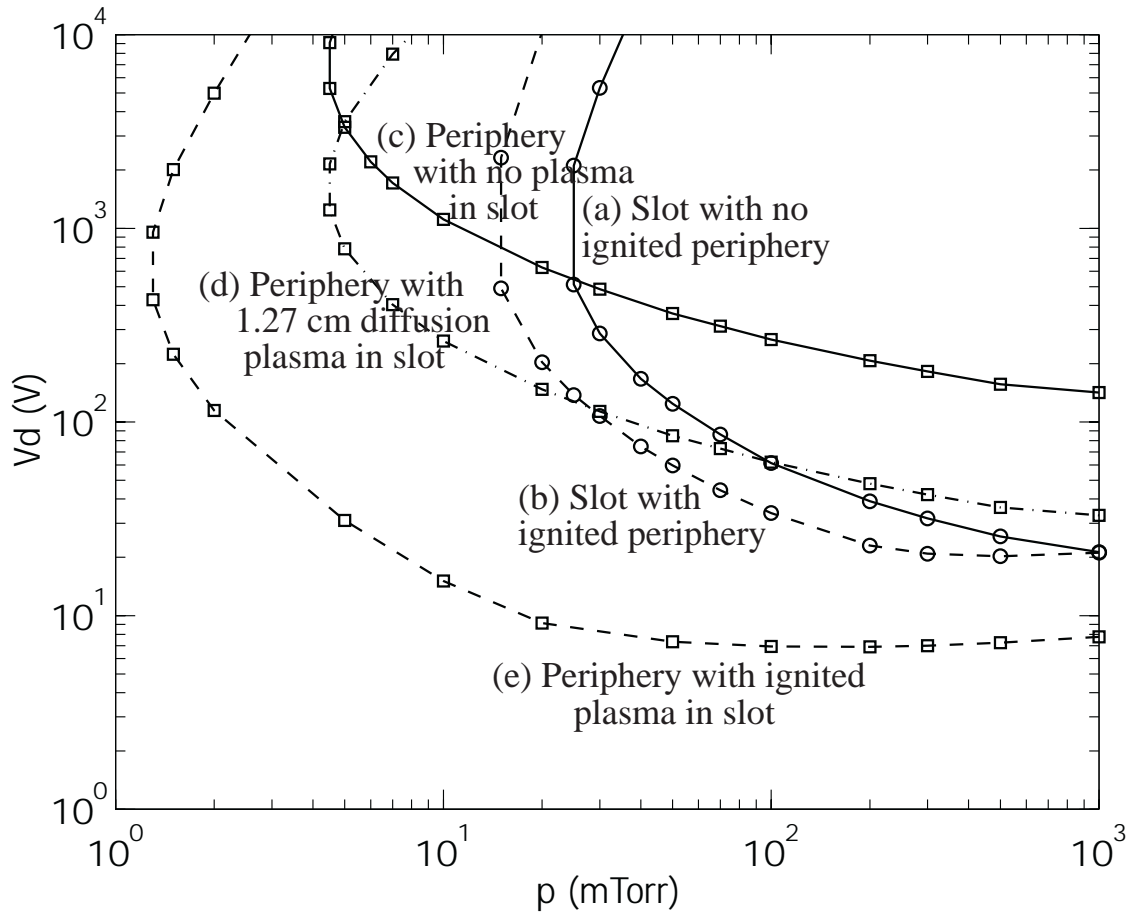


Figure 6.7. Maintenance curves for the same conditions as those of figure 6.5 but with $w = 2$ cm.

In figure 6.7, we show the same curves as in figure 6.5, but for a reduced gap length $w = 2$ cm. At 100 mTorr, the slot and periphery ignite at about the same voltage, 60 V (curves a and d). Between 25 - 100 mTorr, the peripheral plasma first ignites (curve d), subsequently igniting the slot (curve b); between 4 - 25 mTorr, the periphery ignites, but the slot does not ignite. Figures 6.5 - 6.7 can be used to determine loss of confinement for different periphery and slot pressures. For example, for the nominal conditions of figure 6.7 with a 10 mTorr periphery pressure, confinement is lost by ignition of the slot

plasma for slot pressures above about 30 mTorr (curve a), and by ignition of the periphery plasma for slot pressures below 30 mTorr (curve d).

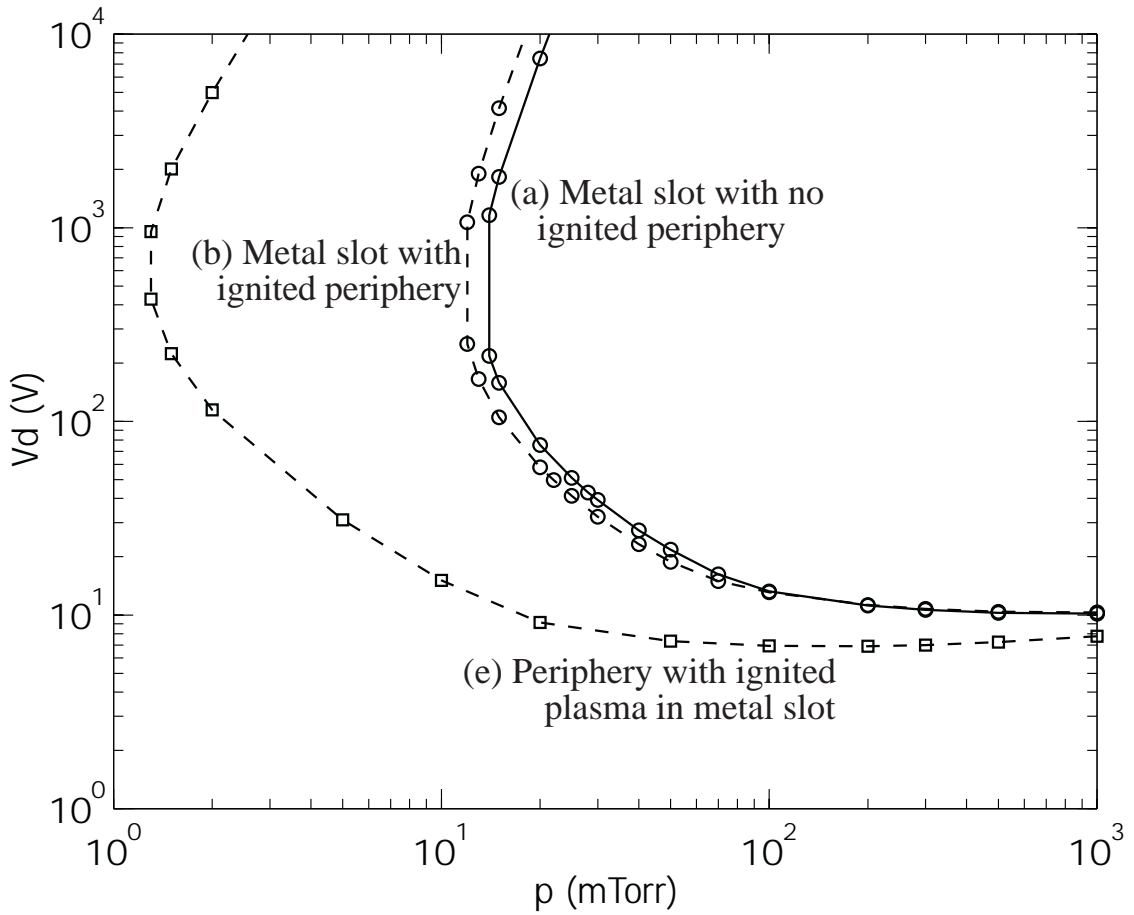


Figure 6.8. Maintenance curves for the same conditions as those of figure 6.5 but with grounded metal confinement rings.

In figure 6.8 we give the results for a somewhat different configuration, with the same dimensions as in figure 6.5, but with the slot plasma confined by grounded metal rings, rather than dielectric rings. The results are significantly lowered values of slot

maintenance at a given pressure (curves a and b), and identical peripheral maintenance when the slot is ignited (curve e). For dielectric rings, a part of \tilde{V}_d is dropped across the dielectric, yielding a reduced voltage drop across the slot plasma, compared to the case of metal rings. Hence, the maintenance voltage is reduced for the metal rings. However, with metal rings if the slot is not ignited it is very difficult to ignite the periphery, since the fields decay exponentially within the slot, with scale length g rather than l , placing curves c and d of figures 6.5 - 6.7 above the \tilde{V}_d -range in figure 6.8.

Chapter 7

Experimental Results

for a Capacitive Discharge

Connected to a Peripheral Chamber

7.1 Experimental Setup and Diagnostics

7.1.1 Experimental Setup

To compare with the theory, we have constructed a chamber for a confined capacitive discharge as shown in figure 7.1. The chamber has quartz confinement rings with 1.5 inch width (7 inch inner diameter, 10 inch outer diameter). Choosing different confinement ring thicknesses, the gap spacing g can be varied as $1/4$, $1/8$, $1/16$, and $1/32$ inch, such that the effect of varying gap spacing on the plasma transport in the slot, and slot and edge plasma breakdown and maintenance, can be measured and compared with the models. The chamber body and the electrode are made of stainless steel. The powered electrode diameter is 5 inches, and main discharge grounded electrode diameter is 7 inches. The separation between the electrode plates is 1 inch. A 6 mm ($1/4$ inch) wide optical slot is incorporated on the ground electrode with a quartz cover plate, to obtain the optical emission from the main discharge, the quartz confinement rings, and the peripheral discharge, along the entire diameter of the ground electrode. Other view ports

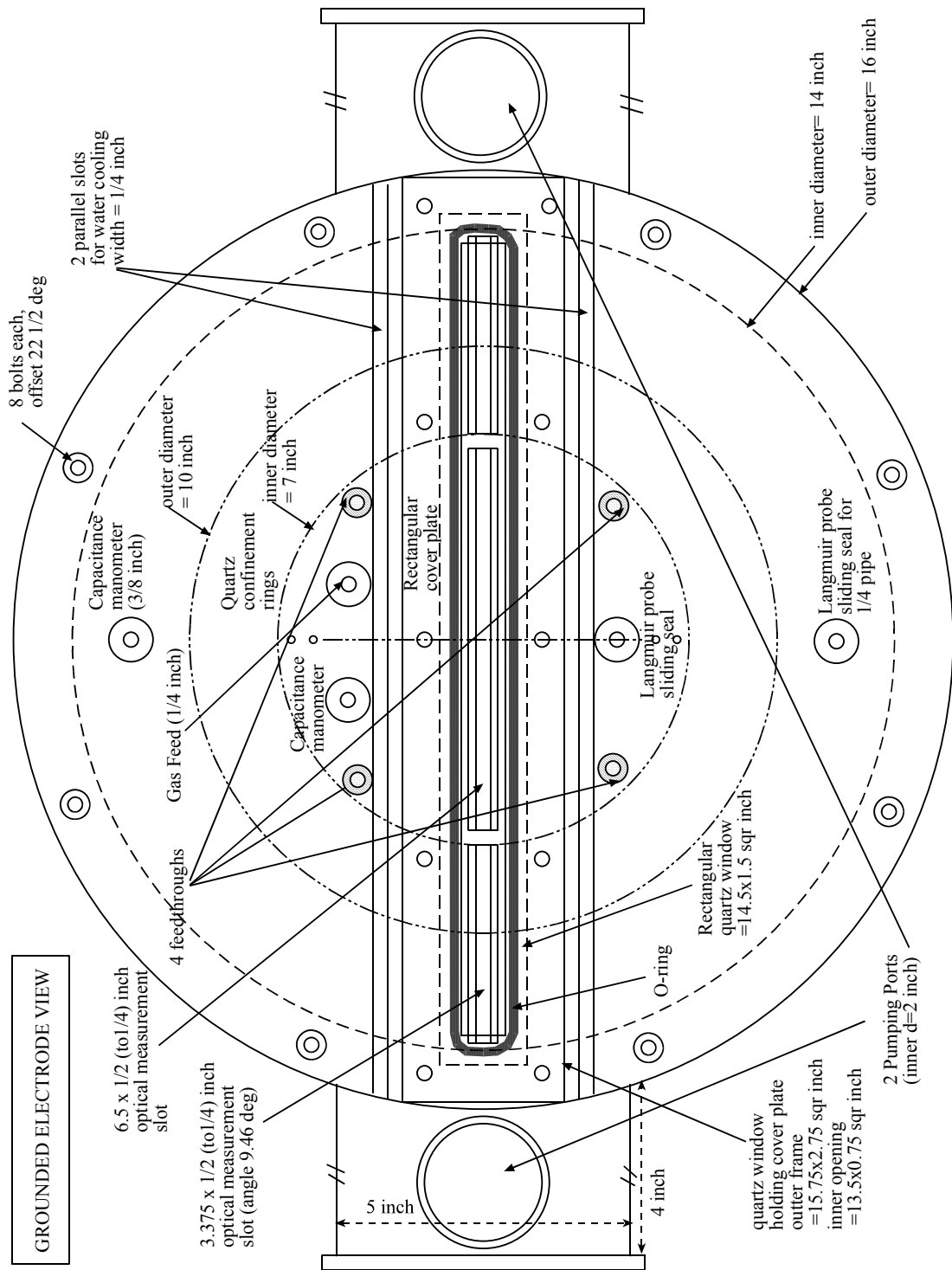


Figure 7.1 (a). A front view drawing of the experiment chamber (viewed from the ground electrode side) with descriptions of the components.

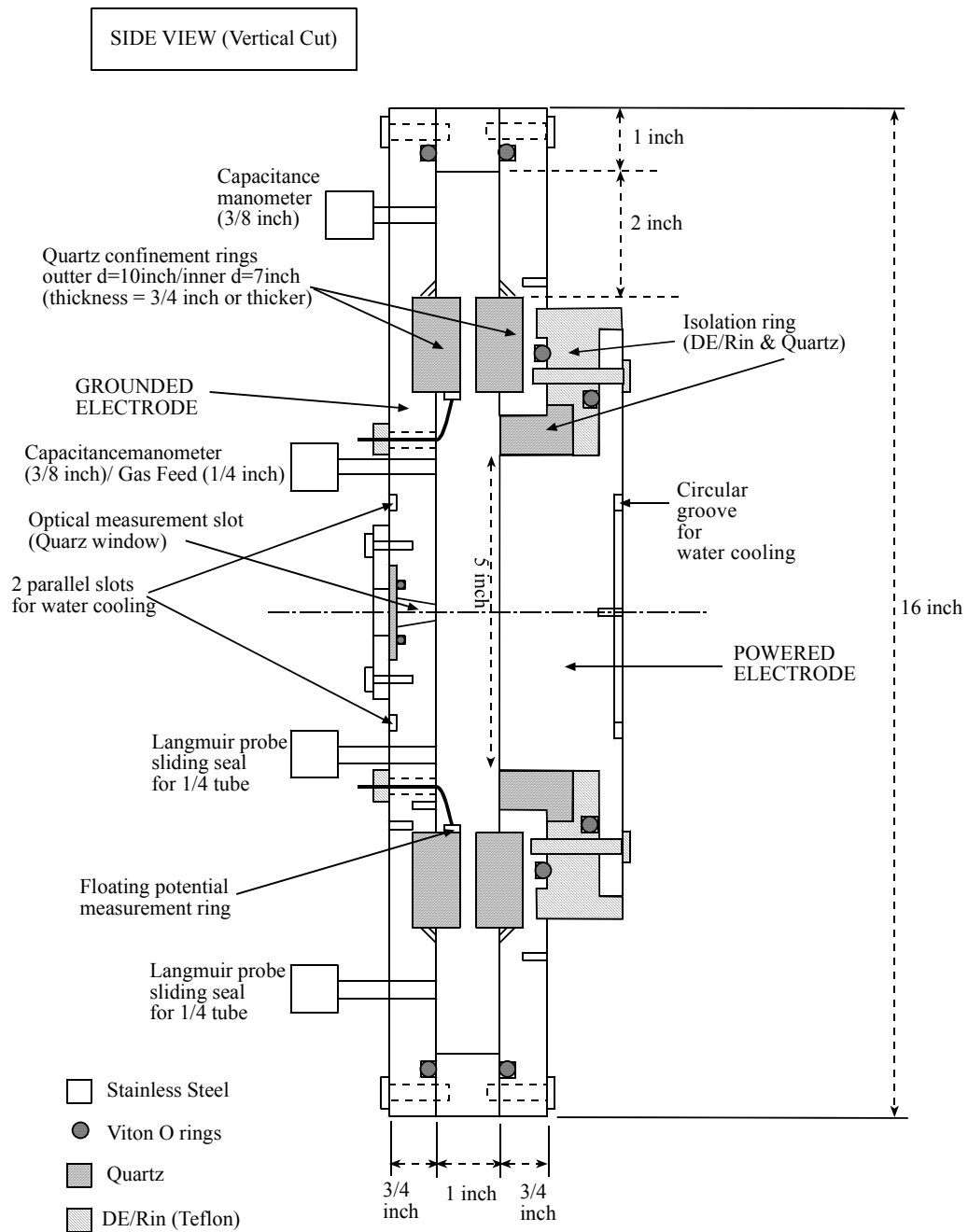


Figure 7.1 (b). A vertical-section drawing of the experiment chamber with descriptions of the components.

are located at both ends of the two side extensions for the vacuum pump connection to provide a side angle view into the peripheral region and the slot between the confinement rings. The chamber body is water-cooled by a loop of 1/4 inch cooling water pipe made of brass, which is soldered on the grounded electrode plate. The powered electrode is cooled by a closed loop filled with the de-ionized (DI) water with temperature and pressure controlled by a M&W Systems Flowrite Cooling System.

The gas flow into the chamber is controlled by Tylan PC-2900V flow controller calibrated for argon (0 - 100sccm). The pressure in the chamber is monitored with MKS Baratron capacitance manometers (model 127) connected to MKS Type PDR-C-2C power supply digital readouts. The gas pressure can be adjusted manually by changing the opening of the gate valve. The gases are pumped out through two 2 inch KF ports connected to a Leybold Turbotronik NT 340M turbomolecular pump (340 liter/sec) backed by a W.M. Welch rotary pump giving a base pressure of about 1×10^{-6} mTorr.

RF power is delivered to the powered electrode by a ENI A500 power amplifier (500 W maximum power output at 0.3 - 35 MHz) which amplifies the signal coming from an RF source. As a RF source we used a Protek 9301 Synthesized Function Generator (up to 31 MHz) through a Precision Attenuator (by Airborne Instruments Laboratory) with an analog knob, to adjust the RF power gradually without spiking (discontinuities) of the signals. Between the power amplifier and the powered electrode, an L-type matching network shown in figure 7.2, is designed to match the 50 ohm resistance of the power source to the powered electrode. The matching network consists of a variable shunt capacitor C_1 and a variable series capacitor C_2 and a 0.8 μ H inductor. C_2 is a vacuum Jennings capacitors operating in the range of 12 - 500 pF, and C_1 is a sum

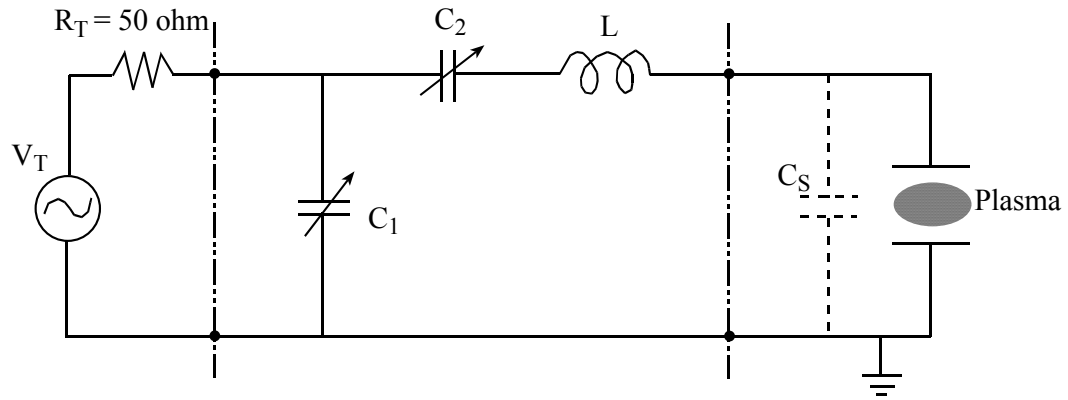


Figure 7.2. Schematic diagram of the matching network used for the experiment system.

of a fixed capacitor of 2100 pF and a vacuum Jennings capacitor (12 - 1000 pF) connected in parallel to operate in the range of 2112 - 3100 pF.

Figure 7.3 is a photograph of the experimental chamber viewed from the front and the side.

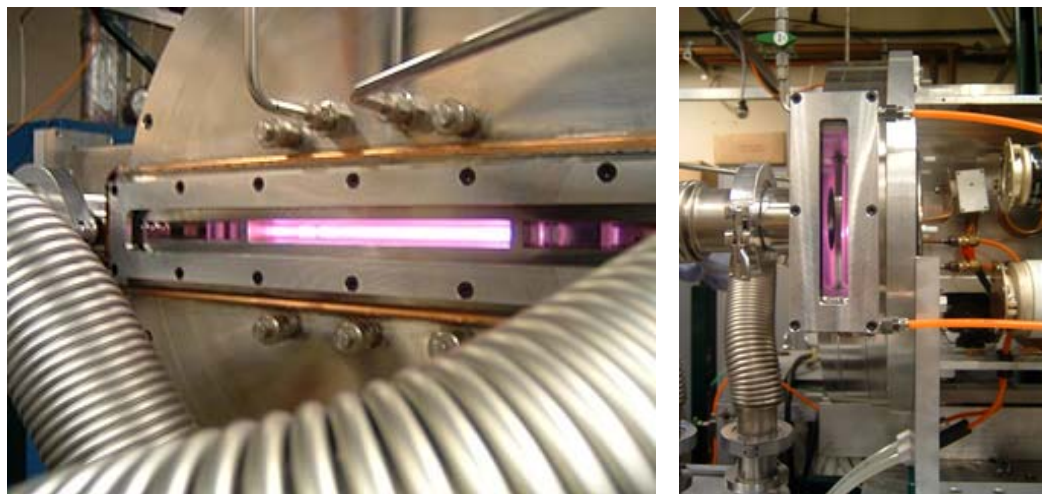


Figure 7.3. The capacitive discharge experimental setup. Left is a view from the front, and the right is a view from the side.

7.1.2. Diagnostics

The experimental setup has several diagnostics to investigate the parameters of the plasma in the chamber and the external electrical characteristics of the plasma system. The diagnostics include optical emission, electrical probes immersed in the plasma, and measurements for the external circuit parameters such as rf power, rf voltage, and currents.

The optical emission spectroscopy system detects the light emitted from the plasma in the main discharge, the gap between the confinement rings and the peripheral region. The system is equipped with a monochromator and an optical filter for argon to measure the argon emission (748.7 nm) line as a function of time. The optical emission signal can be monitored and recorded through a HP 54600B oscilloscope connected to a PC. The diagnostic yields quantitative visual evidence of the breakdown, maintenance and any instability of the main and peripheral discharges.

To measure the time-varying floating potential near the slot entrance, a floating potential ring probe is installed as shown in figure 7.4. A 7 inch diameter circular loop made of stainless steel strip with 1/4 inch width is installed around the inner diameter surface of the quartz confinement ring on the grounded electrode side. It has four 1 mm legs of wire extended to the outside of the chamber through the vacuum sealed feedthroughs. One of the wire extensions is connected to a Tektronix P5100 oscilloscope probe with 2.75 pF of capacitance, which detects the voltage from the probe and displays the time-varying floating potentials near the slot entrance on the oscilloscope. This method of floating potential measurement is based on the similar techniques developed by Godyak and Piejak [56]. The voltage measured from the probe differs from the

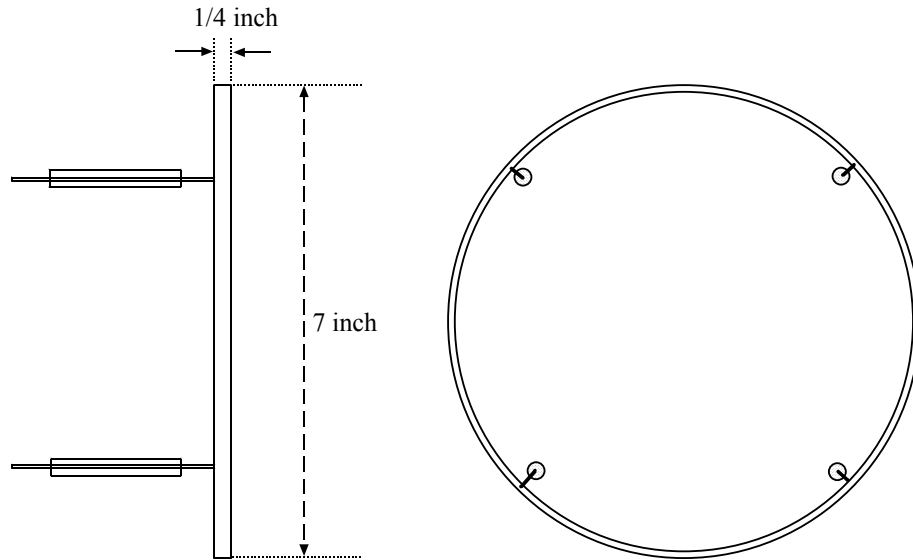


Figure 7.4. A drawing of the floating potential measurement ring probe.

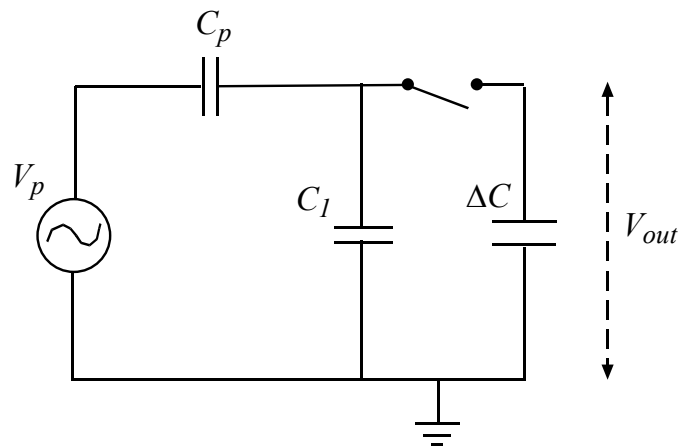


Figure 7.5. Equivalent circuit model of the potential measurement system.

actual plasma potential due to the capacitive coupling (C_p) between the plasma and the probe. As shown in figure 7.5, this coupling and the capacitance of the probe with respect

to the ground make the detecting system equivalent to a voltage divider, and the measured voltage V_{out} is proportional to plasma potential V_p as

$$V_{out} = \frac{C_p}{C_p + C_1} V_p, \quad (7.1)$$

where C_1 is the total capacitance of the measurement system to the ground including the stray capacitance of the ring probe and the input capacitance of the Tektronix P5100 probe. Because the values of the plasma potential V_p and the plasma capacitance C_p are unknown, it is impossible to find V_p by merely measuring V_{out} . However, V_p can be calculated if the measurement is performed for two different values of the capacitance C_1 and C_2 ($C_2 = C_1 + \Delta C$) by adding a small capacitor ΔC connected from the ring to the ground, as shown in figure 7.5. Then we have

$$V_{out} = V_1 = \frac{C_p}{C_p + C_1} V_p, \quad V_{out} = V_2 = \frac{C_p}{C_p + C_2} V_p. \quad (7.2)$$

Therefore,

$$C_p(V_p - V_1) = C_1 V_1, \quad C_p(V_p - V_2) = C_2 V_2. \quad (7.3)$$

Dividing the left and right hand side of the equations in (7.3), we get

$$\frac{V_p - V_1}{V_p - V_2} = \frac{C_1 V_1}{C_2 V_2}, \quad (7.4)$$

and we get

$$V_p = \frac{(C_2 - C_1)}{C_2 V_2 - C_1 V_1} V_1 V_2 \quad (7.5)$$

In our experiments, the stray capacitance of the ring probe was measured as 80 pF, and the input capacitance of the P5100 probe was 2.75pF. Therefore the total C_1 was 82.75 pF, and, by adding 23.7 pF of ΔC , C_2 was 106.45 pF.

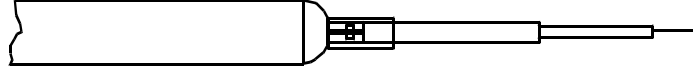


Figure 7.6. The Langmuir probe. The probe tip length is 2.5 mm and its radius is 65 μm (diameter = 0.13 mm).

To measure the plasma density in the discharge, we used a small cylindrical Langmuir probe (as shown in figure 7.6) made of a 0.13 mm diameter and 2.5 mm long platinum wire. The probe tip was placed on the midplane of the main discharge. With a cylindrical Langmuir probe, as explained in chapter 6 of [2], we can measure the ion saturation current I_{i_sat} by applying a high negative bias voltage V_B to the probe. The ion saturation current from the probe flows through a 2.4 k Ω resistor, and the voltage drop across this resistor is measured and displayed on a HP 54600B oscilloscope. By dividing the voltage drop by the resistance of the resistor, we can get the value of the ion saturation current I_{i_sat} . From this current, we can calculate the ion density n (or the plasma density for a electropositive plasma) using the relation [2]

$$I_{i_sat} = 2enad \left(\frac{2e |\Phi_p - V_B|}{M} \right)^{1/2}, \quad (7.6)$$

which yields

$$n = I_{i_sat} \left(\frac{M}{8e^2 a^2 d^2 |\Phi_p - V_B|} \right)^{1/2}, \quad (7.7)$$

where Φ_p is the plasma potential, a is the radius and d is the length of the probe tip.

An Advanced Energy Z-Scan RF Measurement probe, installed between the matching network and the powered electrode, is used to measure the rf voltage and current delivered to the discharge. For the measurement of delivered rf powers, we use a Bird Electronics Model 4522 Wattmeter installed between the rf amplifier and the matching network.

7.2 Experimental Measurements

In the experimental measurements presented in this work, we used a 27.12 MHz power source, using the widest gap spacing of 0.635 cm (1/4 inch). Varying the gap spacing would be a more complete test of the theory, but we couldn't reach the conditions of peripheral breakdown with the narrower (1/8, 1/16, and 1/32 inch) gap spacings with the 500W limit of the maximum output power from the rf amplifier. As discussed in the previous chapter, we predict that a higher rf voltage on the powered electrode is needed for the smaller gaps to ignite a peripheral plasma. Therefore, the fact that we couldn't get breakdown of the periphery at the narrower gaps is consistent with the theory developed in chapter 6.

In a set of measurements with a 27.12 MHz power source and the 0.635 cm gap spacing, we can see that a transition occurs from a centrally confined plasma to a plasma that exists also in the slot and peripheral regions with increasing rf power. As shown in figure 7.7, the plasma is stable and confined in the central region of the chamber inside the quartz confinement rings with lower rf powers. But, as the rf power is increased, a 'finger' of plasma extends into the gap between the quartz slot, and, finally at some point,

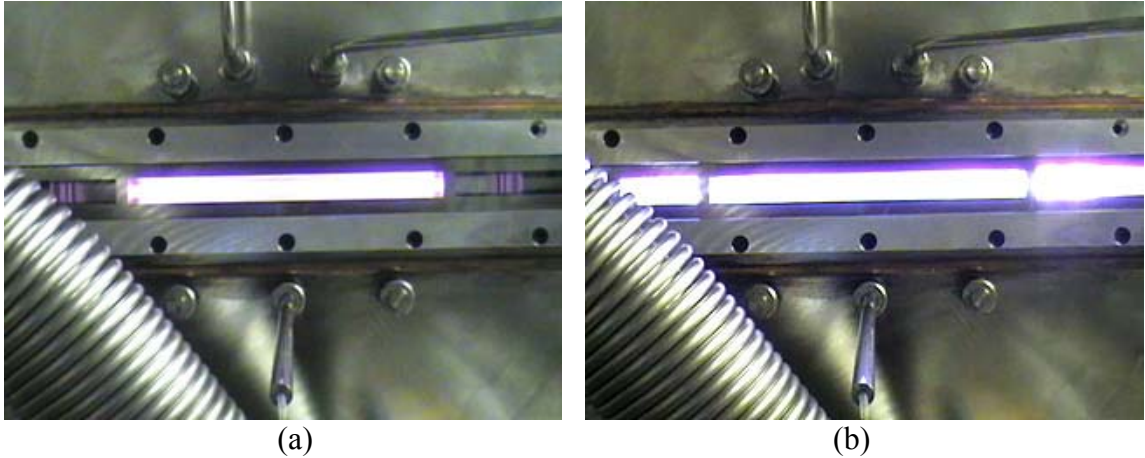
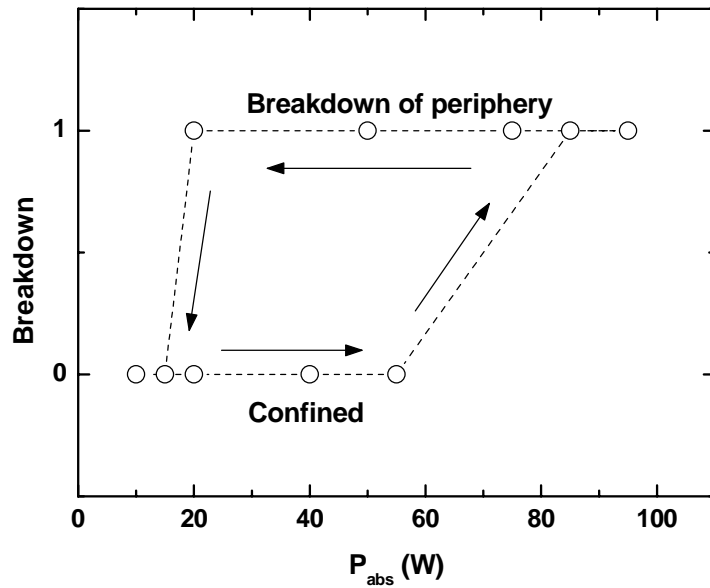


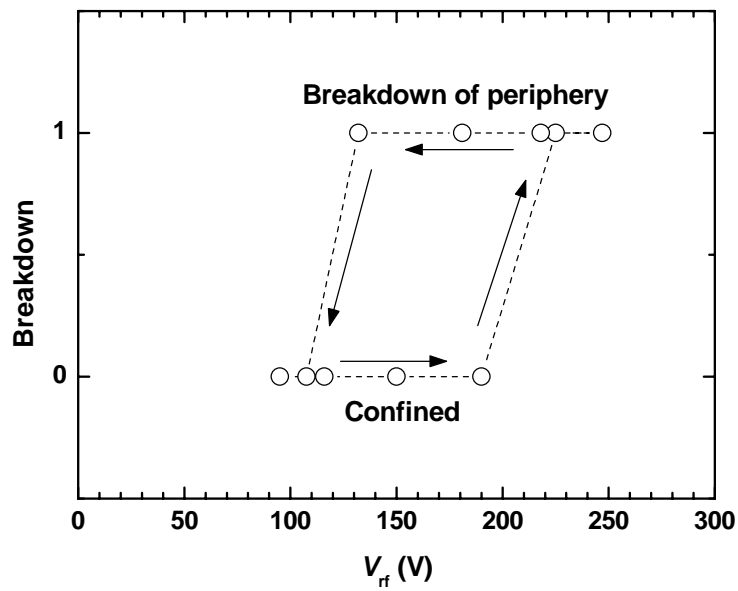
Figure 7.7. Comparison of the two different states: (a) the confined plasma inside the quartz ring, (b) the plasma ignited in the periphery showing unstable blinking.

the slot breaks down and a plasma is also ignited in the peripheral region. In general, ignited peripheral plasma is not stable, but visually blinks with a frequency of a few hertz. When viewed from the side view port, this blinking can be seen as several bright balls of light rotating in the peripheral region around the outside of the quartz confinement rings.

As shown in figure 7.8, we have observed that a hysteresis occurs such that the maintenance of the peripheral plasma occurs at a lower voltage, when decreasing the voltage, than that required to create the peripheral discharge. In figure 7.8, we can see that the peripheral plasma breaks down at $V_{rf} = 225$ V (absorbed rf power $P_{abs} = 85$ W). But this peripheral plasma is not extinguished when the rf voltage (or rf power) is decreased below the point of ignition, until V_{rf} is reduced down to 107 V ($P_{abs} = 15$ W). By increasing and decreasing the rf power repeatedly with several different pressures, we recorded the rf voltage where the peripheral breakdown started as well as the voltage where the confinement was restored. Measurements were performed at 50, 75, 100 and 198 mTorr in argon, with all pressures showing similar hysteresis behavior. But, we can



(a)



(b)

Figure 7.8. Hysteresis curves at 100 mTorr with upper level indicating breakdown of peripheral plasma and lower level indicating a confined plasma; (a) with respect to the absorbed rf powers, (b) with respect to the rf voltage V_{rf} measured with Z-scan.

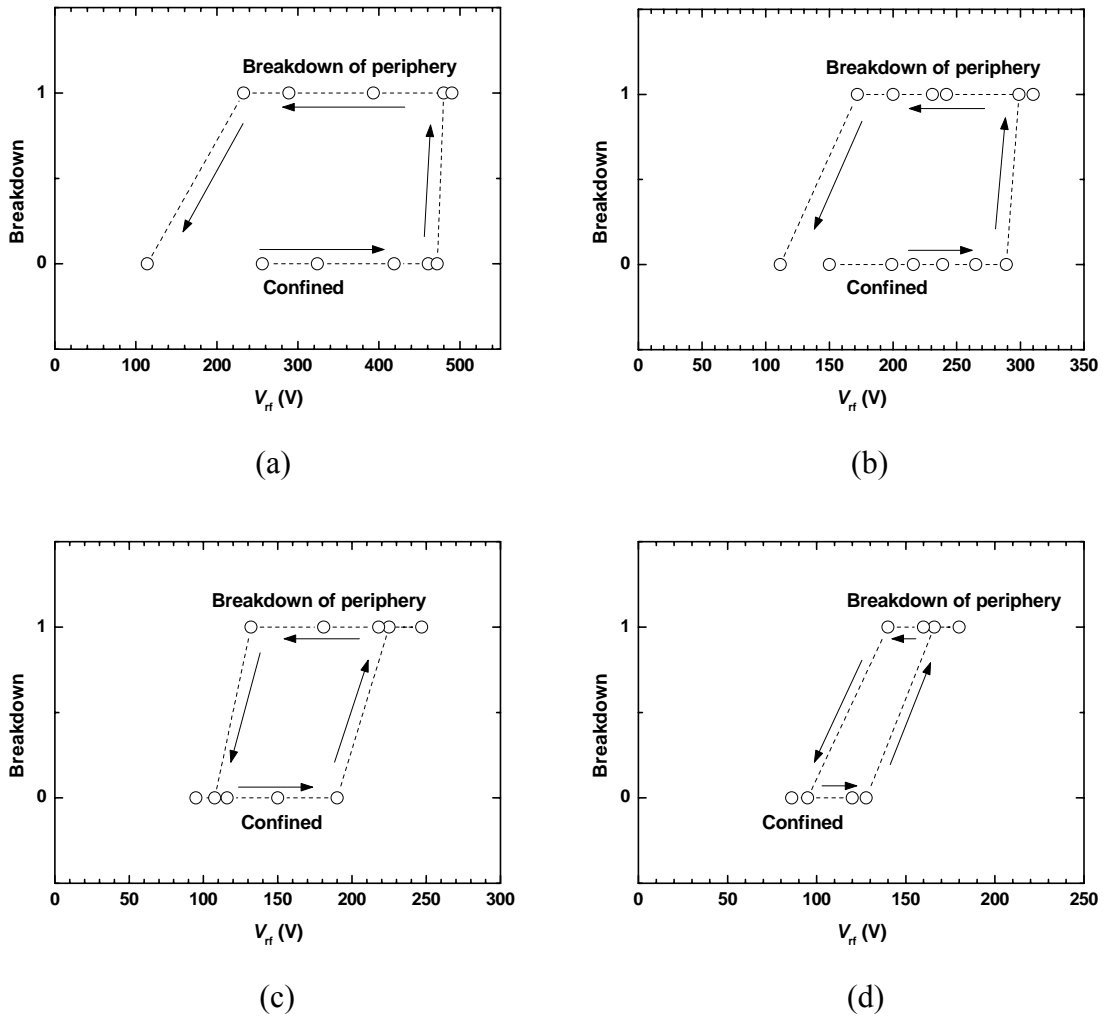


Figure 7.9. Hysteresis curves with respect to the rf voltage at four different pressures with upper level indicating breakdown of peripheral plasma and lower level indicating a confined plasma; the pressures are (a) 50 mTorr, (b) 75 mTorr, (c) 100 mTorr, and (d) 198 mTorr.

see that there are two kinds of pressure dependent effects in the conditions of ignition and quenching of the peripheral plasma. The first is that, as shown in figure 7.9, more rf voltage is required to ignite a peripheral plasma as the pressure is decreased. For pressures below 50 mTorr, we were not able to ignite the periphery up to the rf power maximum (500 W) of our amplifier. The second is that, as the pressure is decreased, the

area of the hysteresis loop increases. In other words, the difference between the rf voltages for ignition and quenching increases as the pressure is decreased. At the higher pressures such as 200mTorr, the difference between the ignition voltage and the quenching voltage is only about 30 volts. However, at 50 mTorr, the difference is more than 300 volts. These two pressure dependent hysteresis behaviors are qualitatively to be expected from our analysis, and will be discussed in the next section.

An unexpected phenomena was the observation, shown in figure 7.10 and 7.11, of both high frequency (kHz range in figure 7.10) and low frequency (Hz range in figure 7.11) relaxation oscillations, for conditions when plasma exists in the main discharge and slot regions (kHz range only), or in the entire system (main, slot, and peripheral discharge, kHz and Hz oscillations). The high frequency oscillation was found to occur within a narrow range of rf powers (or rf voltages), conditions near the slot ignition onset at a given pressure. Also, the high frequency oscillations occur when the system is not well matched, with the reflected rf power about 80% of the forward rf power. Our analysis indicates that this high frequency instability happens due to the combined effect of a slot plasma breakdown and a matching-network resonance. The model will be discussed in section 7.5. The low frequency oscillations are almost independent of power and pressure, and are presently not understood. The existence of these oscillations causes an instability in the main discharge, which is one of the causes of the deterioration of the performance of reactors exhibiting peripheral breakdown.

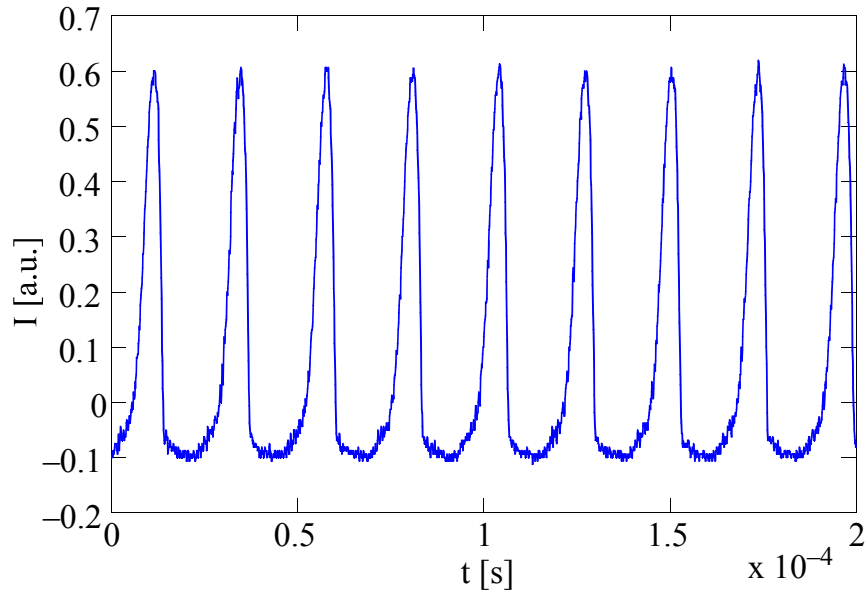


Figure 7.10. Time-varying optical emission I from the main discharge region, showing a high frequency (43.3 kHz) relaxation oscillation; 100 mTorr and 80 W absorbed power; argon emission at 748.7 nm was detected through a notch filter and a fiber optic cable; the zero of I is not calibrated

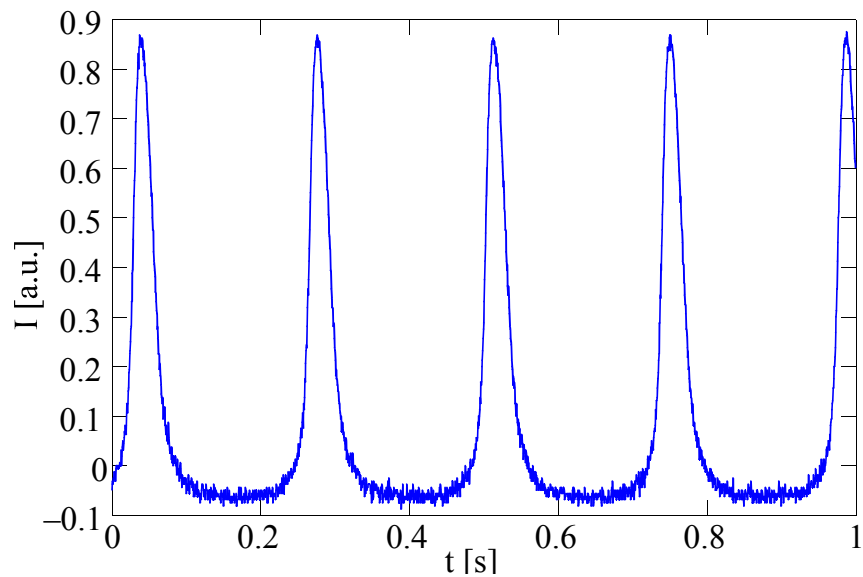


Figure 7.11. Time-varying optical emission I from the main discharge region, showing a low frequency (4.21 Hz) relaxation oscillation; 77 mTorr and 202 W absorbed power; the zero of I is not calibrated

7.3 Comparison of Experimental Maintenance Curves with Theory

In the previous section, we described the pressure dependent hysteresis behavior from the experimental results. As the pressure is decreased, more rf voltage was required to ignite a peripheral plasma and the area of the hysteresis loop increased. These effects are qualitatively to be expected from our analysis, as indicated below.

From the hysteresis curves in figure 7.9, we can measure the rf voltage \tilde{V}_{rf} on the powered electrode just prior to loss of confinement for each pressure. Also, the rf voltage \tilde{V}_{rf} of the quenching of the peripheral plasma at each pressure can be measured from the same data. The rf voltage \tilde{V}_{d} of the main discharge plasma with respect to ground is then determined using the scaling

$$\frac{\tilde{V}_{\text{rf}} - \tilde{V}_{\text{d}}}{\tilde{V}_{\text{d}}} \propto \frac{A_{\text{gnd}}^2}{A_{\text{pow}}^2} \quad (7.8)$$

consistent with the results given in [57] for an asymmetric configuration similar to our experiment, which has a powered electrode diameter of 5 inches and a grounded electrode diameter of approximately 7 inches. Formula (7.8) yields $\tilde{V}_{\text{d}} \approx 0.2\tilde{V}_{\text{rf}}$. Using this relation, we can plot these values of \tilde{V}_{d} versus pressure p together on figure 6.5 using the experimental value of \tilde{V}_{rf} from figure 7.9, and the result is shown in figure 7.12. The rf voltages just before ignition (denoted as upward triangles) yield a trace which is close to the curve (a) which indicates the maintenance voltage of the slot plasma with no ignited periphery. Also, the rf voltages of the quenching of the peripheral plasma (denoted as downward triangles) yields a trace that is close to the curve (b) which

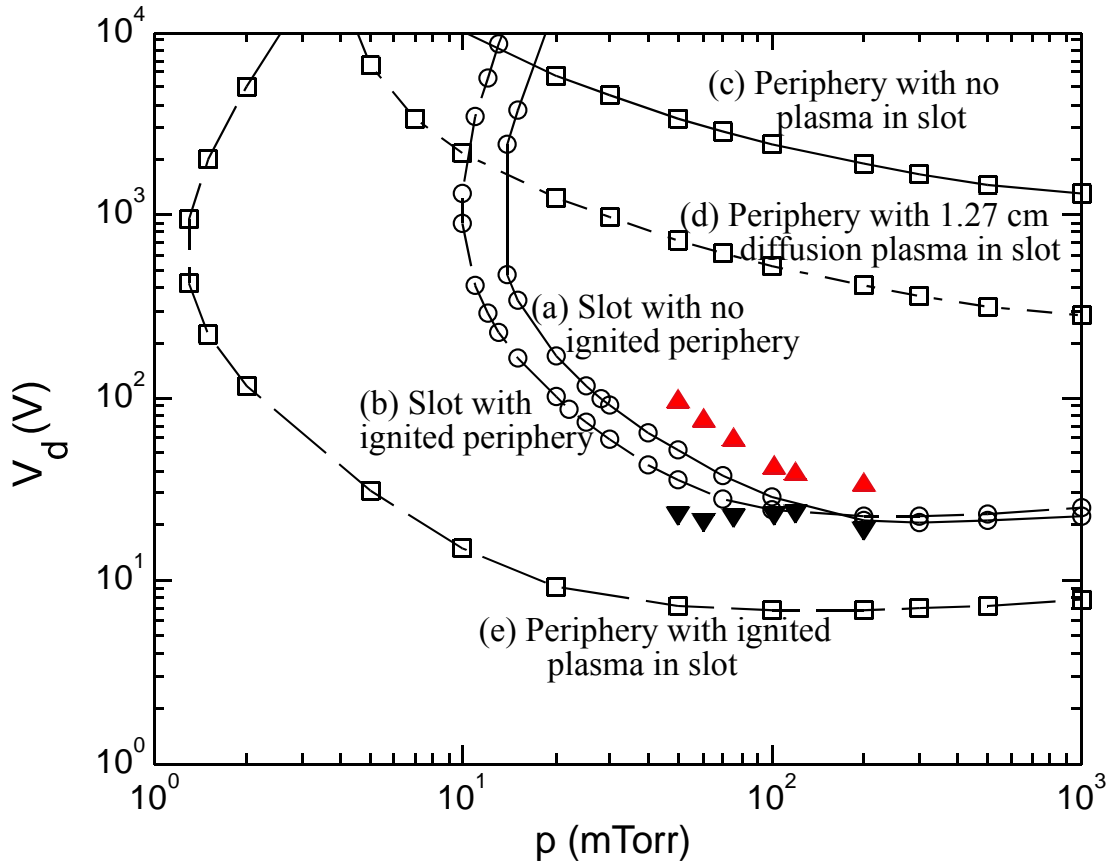


Figure 7.12. Comparison of experimental data (measured by Z-scan probe) with the maintenance curves for experimental conditions $f = 27.12$ MHz, $l = 2.54$ cm, $g = 0.635$ cm, $w = 3.8$ cm, and $w_{\text{per}} = 5.1$ cm; quartz dielectric confinement rings. The upward triangles (\blacktriangle) denote the rf voltage when the periphery ignites, and the downward triangles (\blacktriangledown) denote the rf voltage when the confinement is restored.

indicates the slot maintenance voltage with ignited periphery. These agreements of measured values with the theoretical results gives us confidence in the theoretical calculation of the maintenance curves, and they explain the pressure dependent hysteresis behaviors.

The measured hysteresis (see figure 7.9) between the voltage just prior to peripheral plasma ignition and the voltage for quenching of the peripheral plasma can be

assigned to the difference between the slot maintenance curves with no peripheral ignition (curve (a)) and with peripheral ignition (curve (b)). When the rf voltage \tilde{V}_d is lower than the values on curve (a) at a given pressure, the required rf voltage to maintain a plasma in the periphery is much higher than the \tilde{V}_d , so that the plasma cannot be ignited. If the \tilde{V}_d is increased to sit above the curve (a), the slot plasma ignites and the maintenance curve for the periphery falls down to curve (e) because of the ignited plasma in the slot. This makes the given \tilde{V}_d higher than the required rf voltage to maintain a plasma in the periphery, and the peripheral plasma can be sustained. Therefore, at a given pressure, the rf voltage of curve (a) can be understood as the rf voltage where peripheral plasma ignites. Because the maintenance voltage gets higher as the pressure is decreased in curve (a), the rf voltage to ignite a peripheral plasma needs to be increased as the experiment indicates. Also, at much lower pressures, there is no condition that satisfies the curve (a). This prevents the slot from ignition, so that the maintenance curve of the periphery stays very high like the curve (d). Therefore, a much higher \tilde{V}_d is required to ignite the periphery at lower pressures. This is probably the reason why we couldn't find a condition for peripheral breakdown at pressures lower than 50 mTorr due to the power limitations.

Once a peripheral plasma ignites, the maintenance curve of the slot plasma (a) shifts to curve (b) which is lower than the former one. Now, to extinguish the slot plasma, the rf voltage \tilde{V}_d must be decreased below this new condition which is a somewhat lower value than that of the ignition condition. When the \tilde{V}_d is lowered below the curve (b), the maintenance voltage of the periphery jumps back to a very high level so that the

peripheral plasma cannot be sustained. Therefore, at a given pressure, the rf voltage of curve (b) can be understood as the rf voltage where peripheral plasma gets extinguished. The difference between curve (a) and (b) appears as the hysteresis at a given pressure, and it gets bigger as the pressure is decreased, in qualitative agreement with the experimental results.

We have also measured \tilde{V}_d just prior to the ignition of periphery directly, by

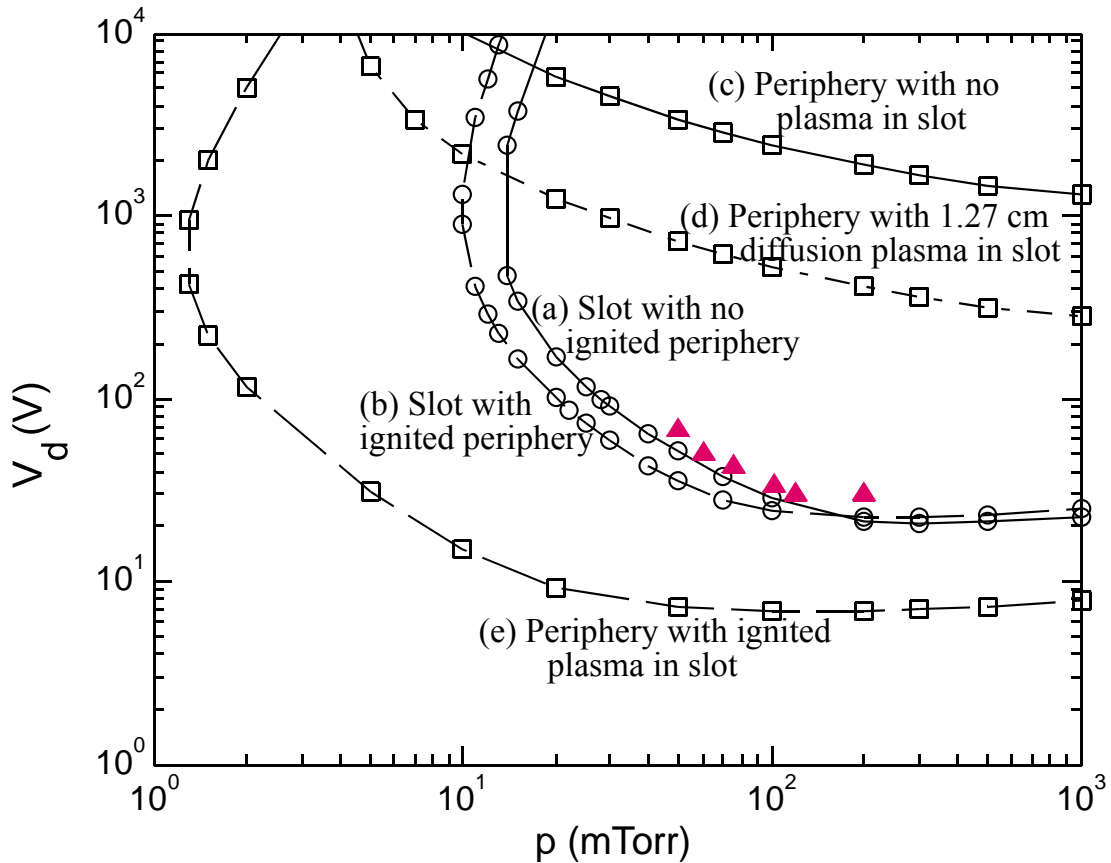


Figure 7.13. Comparison of experimental data (measured by floating potential ring) with the maintenance curves for experimental conditions $f = 27.12$ MHz, $l = 2.54$ cm, $g = 0.635$ cm, $w = 3.8$ cm, and $w_{\text{per}} = 5.1$ cm; quartz dielectric confinement rings. The filled triangles denote the rf voltage just prior to the periphery ignition.

measuring the plasma potential near the slot entrance with the potential ring probe. As shown in figure 7.13, these results show better agreement than the results which used the scaling of (7.8).

There may also be an effect, experimentally, from the difference between gas breakdown, which depends on secondary emission from surfaces, and the conditions of steady state discharge maintenance. The latter difference would not be expected to be large, as there are always significant numbers of nearby electrons in the slot to initiate ignition, in the absence of secondary electron emission.

7.4 Instabilities in Ar Plasma

Associated with the Peripheral Breakdown

As reported in section 7.2, we have observed relaxation oscillations at both high frequency (kHz range) and low frequency (Hz range). The low frequency oscillations can be observed in the peripheral region when the plasma exists there, and they were almost independent of rf power, matching condition, and pressure. This instability can be also observed directly by our eyes, as the visual fluctuation of light emissions in a few hertz. The nature of low frequency oscillations is currently not understood and an extensive effort would be required to understand it.

The instability of the high frequency oscillation was found to occur within a narrow range of absorbed rf power (or rf voltage \tilde{V}_{rf}) conditions which includes the slot ignition condition at a given pressure. As we increase the rf power (or \tilde{V}_{rf}) starting from a

stable confined plasma, the instability begins to occur in the main discharge at somewhat lower rf power than the peripheral breakdown condition. Right after the periphery ignites, this high frequency oscillation can be also found in the peripheral region, and the oscillation frequency is the same as that of the main discharge. When the absorbed power

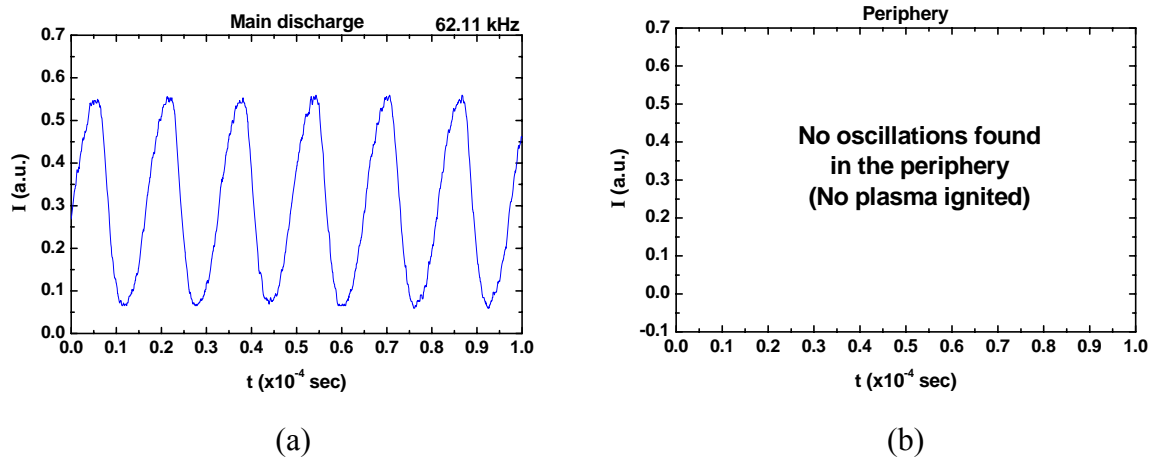


Figure 7.14. Time-varying optical emission I from the main discharge region (a) and the periphery (b), before the peripheral breakdown; 100 mTorr and 30 W absorbed power ($P_{\text{fwd}} = 200 \text{ W} / P_{\text{refl}} = 170 \text{ W}$); the zero of I is not calibrated.

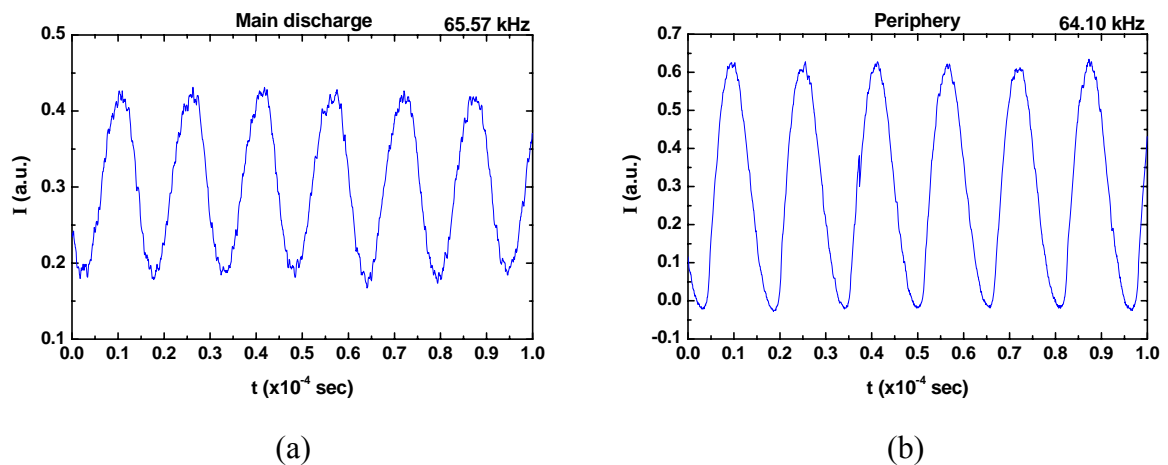


Figure 7.15. Time-varying optical emission I from the main discharge region (a) and the periphery (b), right after the peripheral breakdown has started; 100 mTorr and 38 W absorbed power ($P_{\text{fwd}} = 200 \text{ W} / P_{\text{refl}} = 162 \text{ W}$); the zero of I is not calibrated.

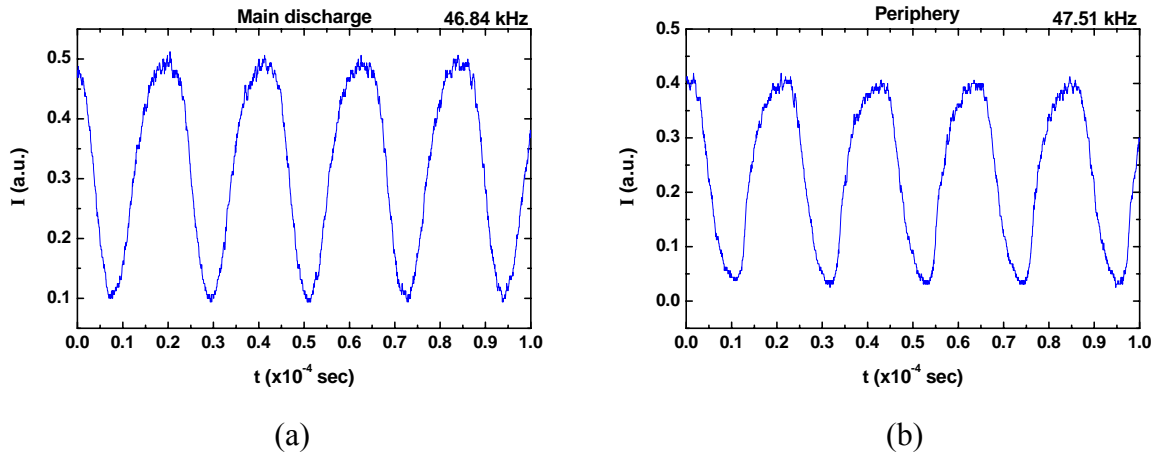


Figure 7.16. Time-varying optical emission I from the main discharge region (a) and the periphery (b), with a little higher absorbed power than the case of figure 7.15; 100 mTorr and 48 W absorbed power ($P_{\text{fwd}} = 200 \text{ W} / P_{\text{refl}} = 152 \text{ W}$); the zero of I is not calibrated.

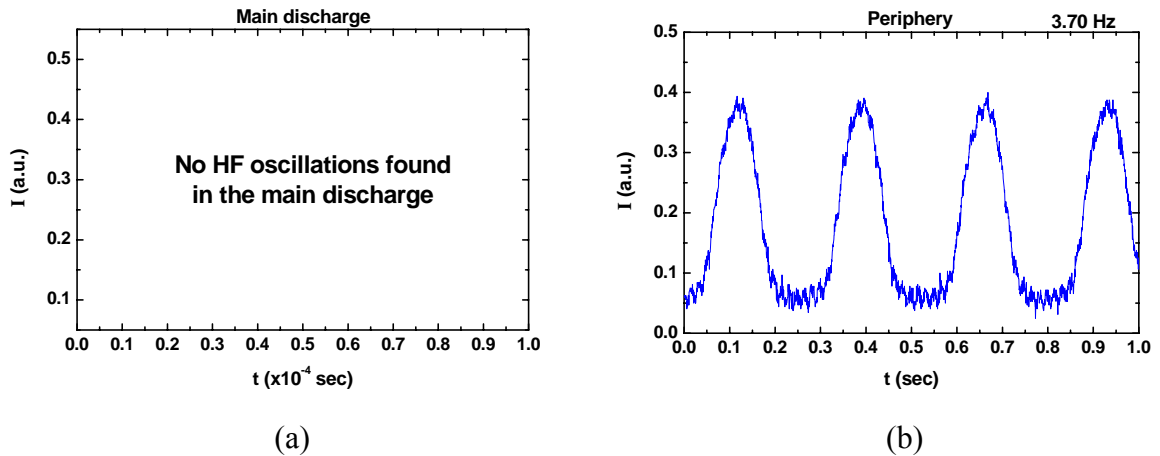


Figure 7.17. Time-varying optical emission I from the main discharge region (a) and the periphery (b), after the low frequency instability has started; 100 mTorr and 58 W absorbed rf power ($P_{\text{fwd}} = 200 \text{ W} / P_{\text{refl}} = 142 \text{ W}$); the zero of I is not calibrated.

(or \tilde{V}_{rf}) is increased more, the low frequency oscillation in the periphery begins and the high frequency oscillation disappears both in main discharge and the periphery. The measured OES from 100 mTorr experiments are shown in figures 7.14 - 7.17 as examples.

When a high frequency oscillation occurs, we can see that the rf plasma potential and the plasma density in the main discharge also oscillate with the same frequency, as shown in figures 7.18 and 7.19. The rf voltage plotted in figure 7.18 is the voltage output V_1 from the floating potential ring without an additional capacitor, which is proportional to the real rf plasma potential. In figure 7.18, the rf plasma potential, which oscillates with the 27.12 MHz driving V_{rf} , shows a periodic time variance in its amplitude of peak-to-peak voltage. Due to the signal delay in the OES system, a small phase difference between two oscillations appears in the plot. But, the frequency of the oscillation in peak-to-peak voltage is exactly the same as that of the oscillation of optical emission. At the

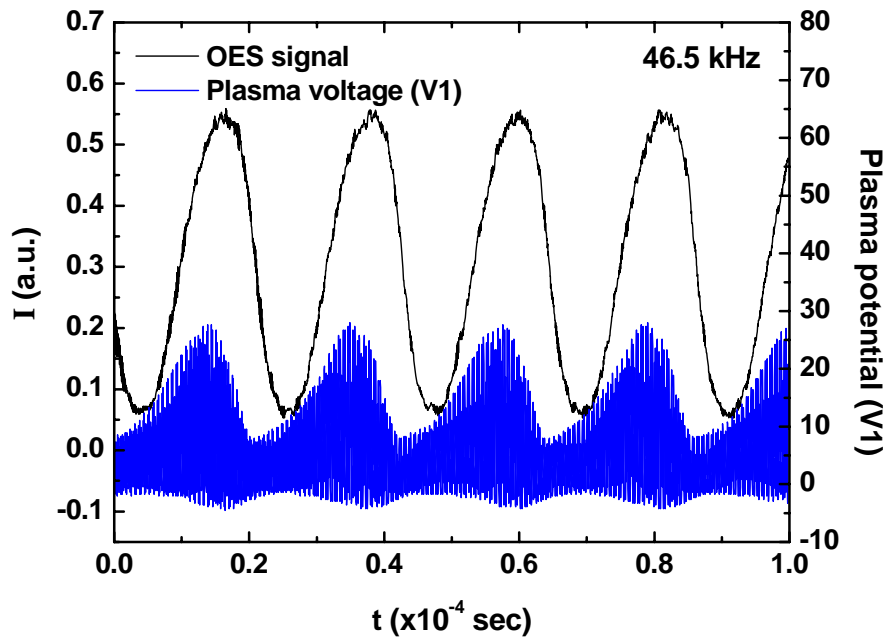


Figure 7.18. Time-varying optical emission I and time-varying rf plasma potential from the main discharge region oscillating together with a frequency of 46.5 kHz; 100mTorr and 15 W absorbed power ($P_{fwd} = 100 \text{ W} / P_{refl} = 85 \text{ W}$); the rf plasma potential shown here is the voltage V_1 measured by the floating potential ring without additional capacitance; the zero of I is not calibrated.

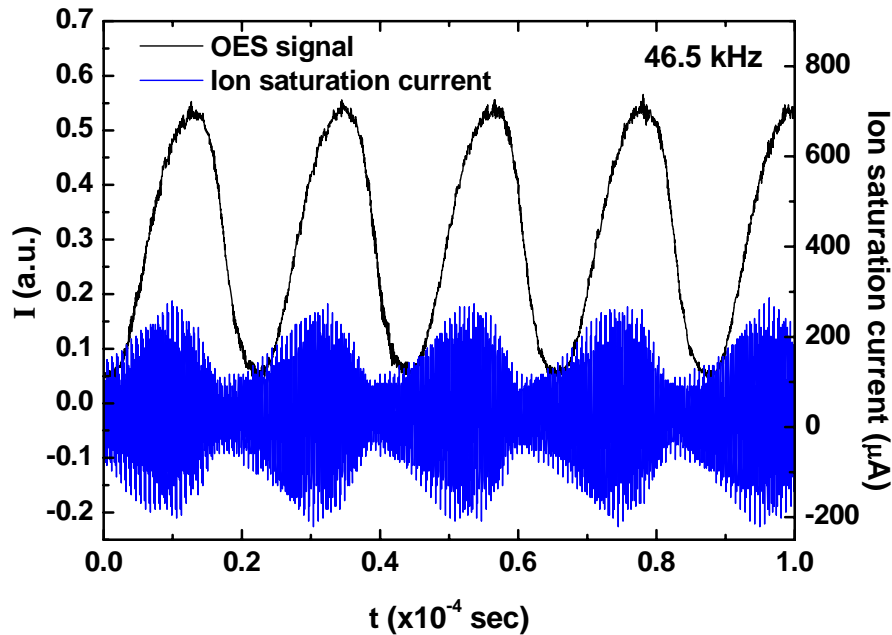


Figure 7.19. Time-varying optical emission I and time-varying Langmuir probe ion saturation current $I_{i, \text{sat}}$ from the main discharge region oscillating together with a frequency of 46.5 kHz; 100mTorr and 15 W absorbed power ($P_{\text{fwd}} = 100 \text{ W} / P_{\text{refl}} = 85 \text{ W}$); the zero of I is not calibrated.

frequency of 46.5 kHz, the rf plasma potential decreases to approximately 67% of its highest value. In the same way, as shown in figure 7.19, the raw data for the ion saturation current measured by a Langmuir probe shows an oscillation in its amplitude of peak-to-peak 27.12 MHz value at the same frequency as that of the OES signal, due to capacitive coupling of the plasma potential to the probe. Averaging the raw signal over many periods of the 27.12 MHz rf power, we obtain a 46.5 kHz oscillation of ion saturation current which can be interpreted as the fluctuation of plasma density at the same frequency. Figure 7.20 shows the fluctuation of plasma density calculated by taking this time-average over 40 periods of the 27.12 Mhz oscillation. With the same frequency

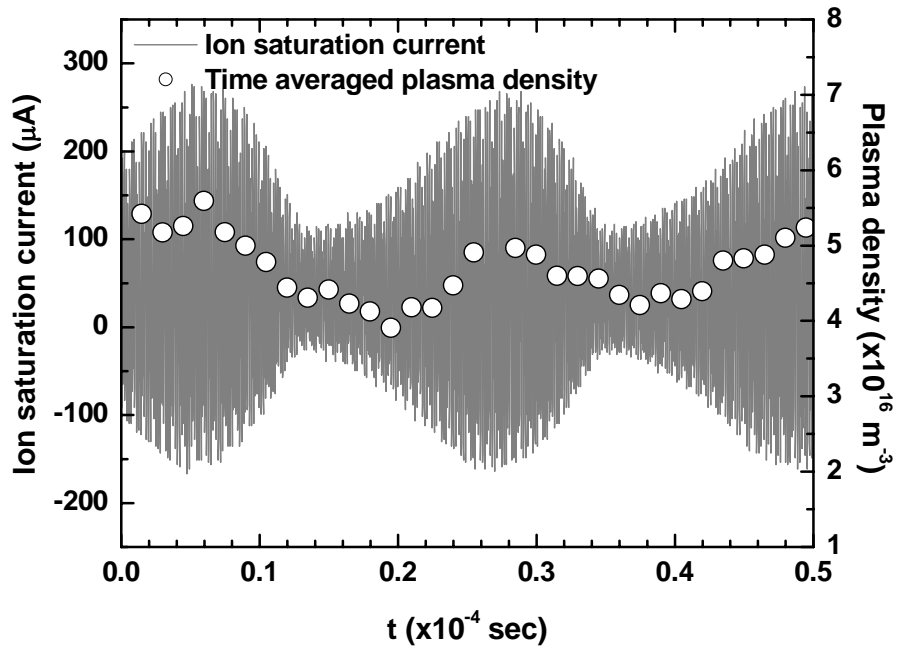


Figure 7.20. Time-varying Langmuir probe ion saturation current I_{i_sat} from the main discharge region and the calculated plasma density oscillating together with a frequency of 46.5 kHz; 100mTorr and 15W absorbed power ($P_{fwd} = 100 \text{ W} / P_{refl} = 85 \text{ W}$); plasma densities were calculated by taking the time-average of I_{i_sat} for each 40 periods of 27.12 MHz oscillation.

of 46.5 kHz, the plasma density is oscillating from $\sim 5 \times 10^{16} \text{ m}^{-3}$ to $\sim 4 \times 10^{16} \text{ m}^{-3}$, showing approximately a 20% reduction from the highest value.

As one can recognize from the rf power conditions for the above experimental results, the high frequency instability occurs only when the system is not well matched, with the reflected rf power nearly 80% of the forward rf power. The range of matching conditions where this instability can be found is quite narrow. This specific requirement on the matching condition implies that the matching network is interacting with the

discharge during the instability. Therefore, in the next section, we propose a model of the interaction between the slot plasma maintenance condition and the matching network condition, to explain this phenomenon.

7.5 A Model of High Frequency Instability

Ignition of slot plasma causes the main plasma voltage V_p to drop due to an increase of the grounded area seen by the main discharge. This will extinguish the slot discharge but may leave the main discharge ignited. However, additional detuning of the match and an overall lowering of the circuit Q can result in also extinguishing the main discharge. Because the formation of a slot plasma results in the propagation of a surface wave with significant phase shifts and resistive decays, an electromagnetic analysis in the slot is relevant. However, this requires some simplifications as described below.

7.5.1 Electromagnetic Analysis of the Slot Impedance

A circuit model of the system is illustrated in figure 7.21. The source is represented as a Thevenin-equivalent voltage with amplitude V_T in series with a source resistance R_T . The matching network with variable capacitance and inductance C_M and L_M are tuned appropriately to obtain the conditions for instability, as described below. The main discharge is modeled as a resistance R_D in series with sheath capacitances C_a at the powered electrode and C_b at the grounded electrode. The slot plasma is represented as an impedance Z_{sl} connected in parallel with C_b .

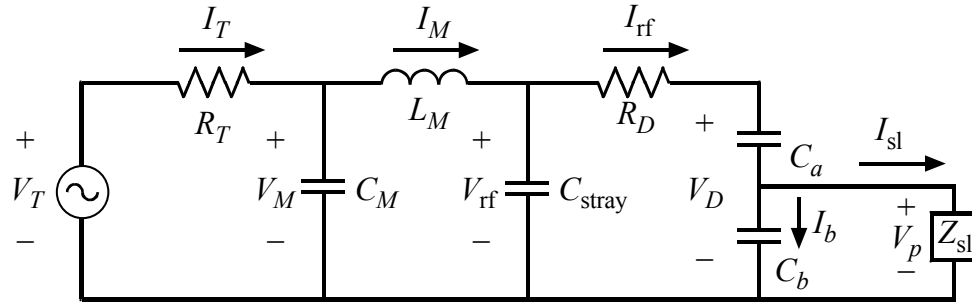


Figure 7.21. Circuit model of the rf power source, L-type matching network, main discharge region, and dielectric slot region.

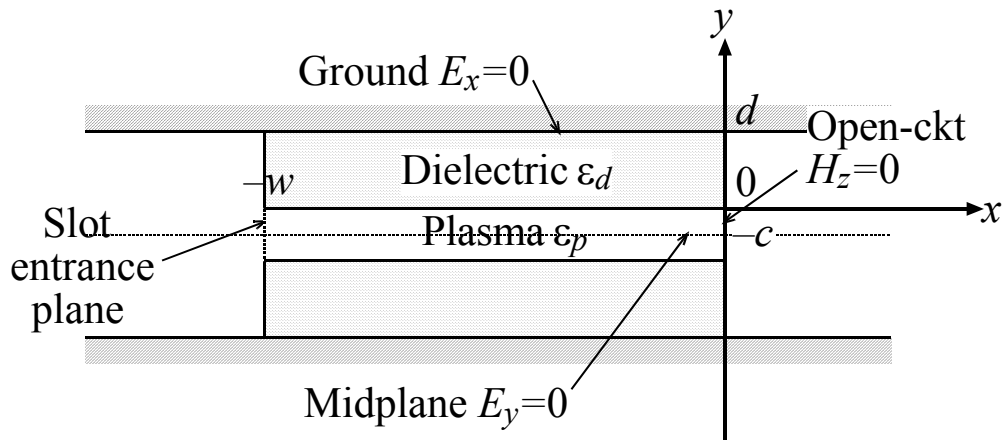


Figure 7.22. Model configuration used to determine the dispersion characteristics $k(\omega)$ and slot impedance Z_{sl} of the surface wave that propagates in the slot plasma.

The impedance Z_{sl} of the slot seen at the main discharge is determined by an electromagnetic analysis. As shown in figure 7.22, the slot plasma is driven at one end (its inner radius) by the rf voltage V_p of the main discharge plasma, with the top and bottom slot surfaces earthed through the quartz confinement rings. As was shown in [58,59], a transverse magnetic (TM) surface wave that propagates along the quartz-plasma interface is excited at the slot entrance. A rectangular coordinate model is used

determine the propagation and impedance characteristics, with x , y , and z corresponding respectively to the radial, axial, and circumferential directions in cylindrical geometry. The TM mode is independent of z . We assume open-circuit boundary conditions for the reflection of the wave at the slot exit. The Maxwell equations to determine the mode characteristics are

$$\frac{\partial E_y}{\partial x} - \frac{\partial E_x}{\partial y} = -j\omega\mu_0 H_z \quad (7.9)$$

$$\frac{\partial H_z}{\partial y} = j\omega\varepsilon E_x \quad (7.10)$$

$$-\frac{\partial H_z}{\partial x} = j\omega\varepsilon E_y \quad (7.11)$$

where $\varepsilon = \varepsilon_0\kappa_d$ in the dielectric and $\varepsilon = \varepsilon_0\kappa_p$ in the slot plasma, with

$$\kappa_p = 1 - \frac{\omega_p^2}{\omega(\omega - j\nu_m)} \quad (7.12)$$

the relative plasma dielectric constant, $\omega_p = (e^2 n_{sl} / \varepsilon_0 m)^{1/2}$ the plasma frequency, and ν_m the electron-neutral collision frequency. This approach ignores all losses except for those caused by collisions. This is probably reasonable, since the small potential drop existing between the slot dielectric and the plasma would produce only small additional stochastic electron heating and ion losses. Eliminating E_x and E_y from (7.9) - (7.11) yields the wave equation

$$\nabla^2 H_z + k_0^2 \kappa H_z = 0 \quad (7.13)$$

with $k_0 = \omega/c_0$, c_0 the speed of light in vacuum, and κ the appropriate relative dielectric constant. We assume $H_z \propto \sin kx$, corresponding to the open-circuit boundary condition

at $x = 0$, shown in figure 7.22, with k the complex propagation constant. Equation (7.13) then reduces to

$$\frac{d^2 H_z}{dy^2} = (k^2 - k_0^2 \kappa) H_z. \quad (7.14)$$

A solution of (7.14) in the dielectric that satisfies the conducting wall boundary condition $E_x = 0$ at $y = d$ is

$$H_{zd} = H_d \cosh \gamma_d (d - y) \sin kx \quad (7.15)$$

with

$$\gamma_d^2 = k^2 - k_0^2 \kappa_d. \quad (7.16)$$

Similarly, a solution of (7.14) in the plasma that satisfies the condition at $y = -c$ that the wave solution be symmetric with respect to the slot midplane $y = 0$ is

$$H_{zp} = H_p \sinh \gamma_p (c + y) \sin kx \quad (7.17)$$

with

$$\gamma_p^2 = k^2 - k_0^2 \kappa_p. \quad (7.18)$$

To determine the wave dispersion and the relation between H_{zd} and H_{zp} , the boundary conditions are used that $H_{zd} = H_{zp}$ and $E_{xd} = E_{xp}$ at the dielectric-plasma interface $y = 0$.

The first condition yields

$$H_{zd} \cosh \gamma_d d = H_{zp} \sinh \gamma_p c. \quad (7.19)$$

Using (7.10) to determine E_x from (7.15) and (7.17), the second equation yields

$$-H_{zd} \gamma_d \kappa_p \sinh \gamma_d d = H_{zp} \gamma_p \kappa_d \cosh \gamma_p c. \quad (7.20)$$

Dividing (7.20) by (7.19) yields the wave dispersion

$$-\gamma_d \kappa_p \tanh \gamma_d d = \gamma_p \kappa_d \coth \gamma_p c. \quad (7.21)$$

For specified plasma and dielectric properties ω , ω_p , v_m and κ_d , (7.21) along with (7.16) and (7.18) can be solved numerically to determine k , γ_d , γ_p , and the fields. The solutions are given below.

The impedance Z_{sl} seen at the slot entrance $x = -w$ can be determined from the current and the time-average complex power flowing into the slot. The surface current flowing into the upper ground plane at $y = d$ and $x = -w$ is found from the wave magnetic field to be $K_x = H_d \sin kw$ (A/m). Including the lower ground plane and using the inner circumference $2\pi R_b$ of the quartz rings, we obtain the current flowing into the slot

$$I_{sl} = 4\pi R_b H_d \sin kw. \quad (7.22)$$

The power is found by integrating the complex Poynting vector $S_x = \frac{1}{2} E_y H_z^*$ over the slot entrance area

$$P_x = 2\pi R_b \cdot 2 \int_{-c}^d dy S_x(-w, y). \quad (7.23)$$

Finally, the slot impedance is

$$Z_{sl} = R_{sl} + jX_{sl} = \frac{2P_x}{|I_{sl}|^2}. \quad (7.24)$$

In figure 7.23, we show kw and Z_{sl} for the surface wave as functions of the plasma density n_{sl} in the slot, for the 27.12 MHz, 100 mTorr base case used in subsequent calculations of the kilohertz instability mechanism. The slot was chosen to be half-filled with plasma, with the remaining sheath widths in the slot absorbed into the dielectric width, such that the half-width of the slot plasma is $c = 0.16$ cm and the quartz dielectric thickness is $d = 1.1$ cm. The plasma width, as well as the electron temperature from

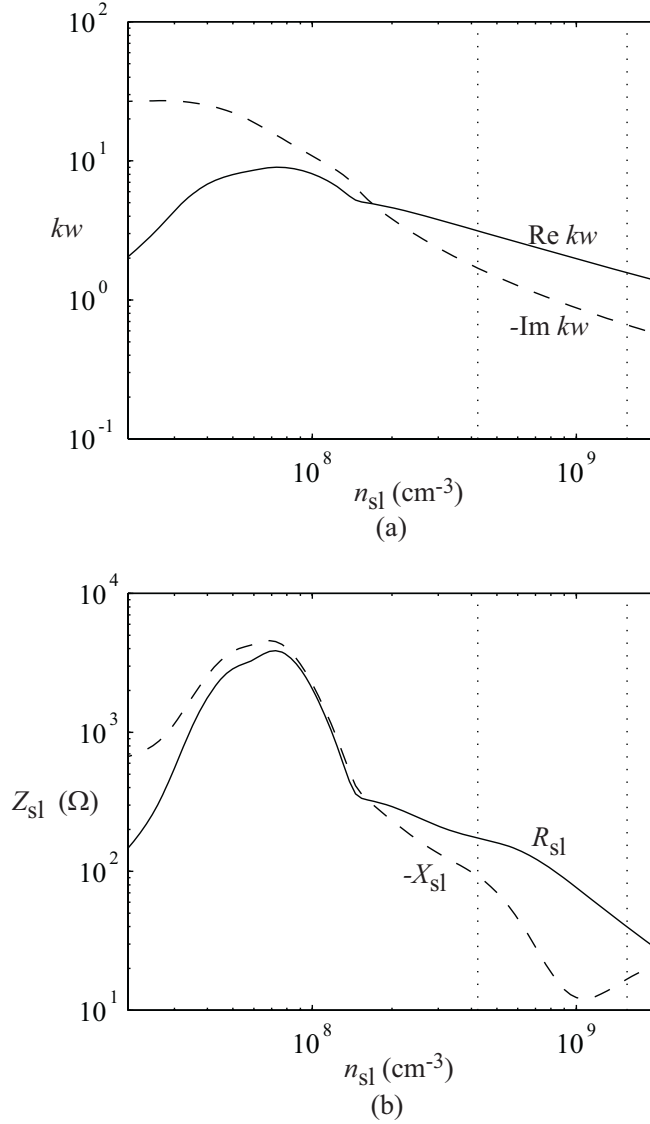


Figure 7.23. (a) Real and imaginary part of the axial wavenumber k versus slot density n_{sl} , and (b) slot impedance Z_{sl} versus n_{sl} , for the base case described in the text.

which ν_m is calculated, change with the slot plasma conditions. Provided the electron temperature does not fall to very low values, which will be seen to be the case, ν_m remains fairly constant. Modification of the assumed plasma width c also does not lead to qualitative changes in the results. At 100 mTorr, the minimum voltage V_p required to maintain a discharge in the slot is approximately $V_{bd} = 29$ V, as found in section 7.3

theoretically and from measurements (see figure 7.13). At this voltage, the central plasma density sustained in the slot is approximately $n_{\text{sl}0} = 2 \times 10^9 \text{ cm}^{-3}$, the highest density shown in figure 7.23. At this pressure and frequency, the collision frequency $\nu_m = 1.5 \times 10^8 \text{ s}^{-1}$ is comparable to the radian frequency ω . This leads to a $k\omega$ that has significant real and imaginary parts at high densities. The expected wave resonances at $\text{Re } k\omega = \pi/2$ and π , shown by the two right-most vertical dotted lines in figure 7.23 (a), are totally washed-out due to the high collisionality, but are clearly seen in calculations done at lower pressures (not shown). Below $n_{\text{sl}} \sim 10^8 \text{ cm}^{-3}$, $\text{Re } k\omega \ll |\text{Im } k\omega|$, and the wave x -variation is essentially evanescent. The corresponding slot impedances are shown in figure 7.23 (b). The slot resistance R_{sl} increases with a decrease in n_{sl} and equals or exceeds the capacitive slot reactance $-X_{\text{sl}}$ down to very low densities. Hence, the slot is mainly resistive at this pressure.

7.5.2 Interaction of the Matching Network and Discharge

As described in section 7.4, the kilohertz oscillation is found by increasing the source voltage V_T supplying rf power to the main discharge. As the voltage is increased, the matching network elements C_M and L_M are adjusted to achieve a mismatch of typically 75% in reflected power near the transition. For the lower voltages, the main discharge appears steady and the slot appears to be dark, except for a “finger” of plasma that diffuses about a half-centimeter into the slot. When V_T is increased above a certain threshold value, the kilohertz main discharge oscillation appears, and the slot lights up. For the calculation we take the reflected power to be 75% near the transition. The

periphery usually remains dark during the oscillation, which will be assumed in the following calculation.

To determine the interaction of the source and matching network with the main discharge and slot during the transition, we solve the ladder-network shown in figure 7.21 to obtain the source voltage V_T as a function of the plasma voltage V_p on the main discharge. For a linear network, V_T would be a linear function of V_p for any chosen slot density, but the main discharge and slot nonlinearities significantly modify this property. The most important nonlinearities, which we retain in the analysis below, are the voltage-dependent main discharge sheath capacitances $C_a(V_a)$ and $C_b(V_p)$. Here $V_a = V_D - V_p$ is the voltage across the powered electrode sheath, and V_p is the voltage across the grounded electrode sheath. We use a collisional (constant mean free path) sheath model ([2], p 411 - 413) to determine these capacitances

$$C_a = K_{\text{cap}} A_a / |V_a|^{3/5}; \quad C_b = K_{\text{cap}} A_b / |V_p|^{3/5} \quad (7.25)$$

where

$$K_{\text{cap}} = 1.25 \epsilon_0 \left(\frac{en_s u_B}{\epsilon_0} \right)^{2/5} \left(\frac{M}{e\lambda_i} \right)^{1/5} \quad (7.26)$$

with n_s the density at the plasma-sheath edge. The sheath edge density was taken to be $n_s = 2 \times 10^9 \text{ cm}^{-3}$, consistent with the value of V_{bd} determined from the breakdown model, and the electron temperature was taken to be $T_e = 2 \text{ V}$. The matching network capacitance was measured just prior to the transition to kilohertz oscillations to be $C_M \approx 2500 \text{ pF}$. We have chosen the discharge resistance to be consistent with this measurement, obtaining a quite reasonable value $R_D = 1.2 \Omega$, which is held fixed in the calculation. The procedure for solving the ladder-network of figure 7.21 is as follows:

Choosing a real V_p and a slot density n_{sl} , then $I_{sl} = V_p/Z_{sl}$, C_b is determined by (7.25) for the given V_p , $I_b = j\omega C_b V_p$, $I_{rf} = I_b + I_{sl}$, and we obtain the equation $|V_a|\omega C_a(|V_a|) = |I_{rf}|$, which can be solved to determine $|V_a|$ and C_a using (7.25). Then $V_a = I_{rf}/j\omega C_a$, $V_D = V_a + V_p$, $V_{rf} = V_D + I_{rf}R_D$, $I_M = I_{rf} + j\omega C_{stray}V_{rf}$, $V_M = j\omega L_M I_M + V_{rf}$, $I_T = j\omega C_M V_M + I_M$, and, finally, $V_T = I_T R_T + V_M$.

Figure 7.24 shows $|V_T|$ versus V_p for six different slot densities, which we use below to provide a plausible explanation for the kilohertz oscillation that is observed experimentally. We discuss first the situation at the very lowest density of 10^7 cm^{-3} shown in the figure, where the slot plasma is essentially absent. For the chosen value of $|V_T|$, shown as the horizontal dashed line $V_{T0} = 44.7 \text{ V}$, there are three solutions for V_p ,

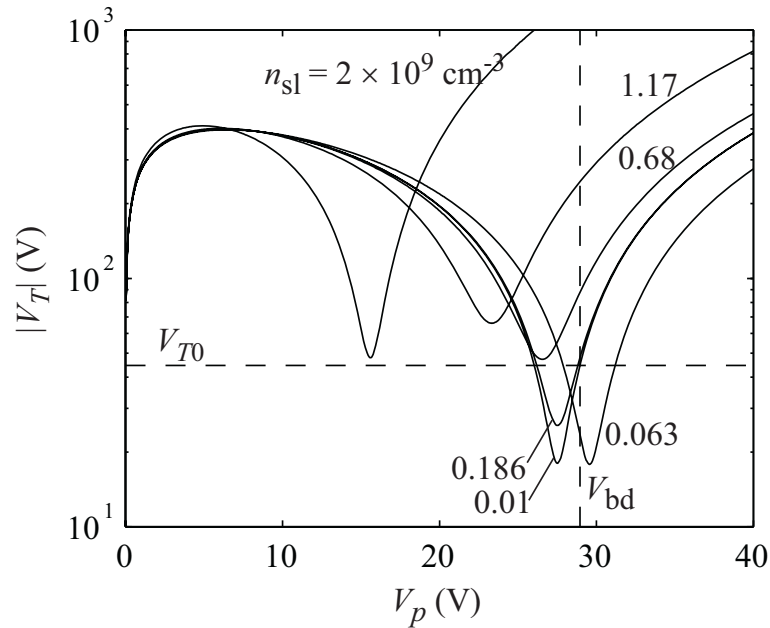


Figure 7.24. Magnitude of the source voltage $|V_T|$ versus main discharge grounded electrode sheath voltage V_p , for six different slot plasma densities, for the base case conditions described in the text.

due to the high-Q resonance just below the breakdown voltage $V_{bd} = 29$ V of the slot. The largest solution for V_p corresponds to an operating point of the main discharge without slot ignition, the smallest V_p near zero corresponds to an extinguished main discharge, and the intermediate value is unstable. However, the matching elements L_M and C_M , and source voltage V_{T0} have been chosen such that the value of V_p at $|V_{T0}|$ just exceeds the breakdown voltage of the slot, $V_{bd} = 29$ V, with a 73% reflected power. In that case, the slot density increases on a fast (ionization) timescale to its maintenance value of $2 \times 10^9 \text{ cm}^{-3}$, determined from the condition of maintenance of plasma in the slot discussed in chapter 6. For this new slot density, as shown in figure 7.24, the only solution for V_p at the chosen $|V_T|$ is the extinguished main discharge state near $V_p = 0$. Hence the voltages V_a and V_p decrease rapidly to zero. Since V_p now lies below V_{bd} , the slot plasma density decays. Referring to figure 7.24, the main discharge remains extinguished until the slot density falls to a value just below $6.8 \times 10^8 \text{ cm}^{-3}$, when the high-Q resonance dips below the horizontal dashed line V_{T0} . At this point the main discharge re-ignites. The slot density continues to decay until $n_{sl} \approx 1.86 \times 10^8 \text{ cm}^{-3}$, when V_p at V_{T0} again exceeds V_{bd} . At this point the slot re-ignites, and the cycle repeats.

The resonance minimum $V_{T_{res}}$, V_p and V_a are plotted versus n_{sl} in figure 7.25. The region at high densities in figure 7.25 (a) where $V_{T_{res}}$ exceeds V_{T0} corresponds to the extinguished state of the main discharge, the region below, to the ignited state. In figure 7.25 (b), the high density region lying below V_{bd} corresponds to the density oscillation in the slot. We see that V_p is near, but below V_{bd} at the lower densities during the slot oscillation, but drops to zero at the higher densities. The same trend is seen for V_a , the rf

voltage amplitude across the powered electrode sheath. Since the electron power deposited into the main discharge mainly depends of the time variation of V_a , we expect a significant oscillation in the main discharge plasma density due to this effect, which we explore below.

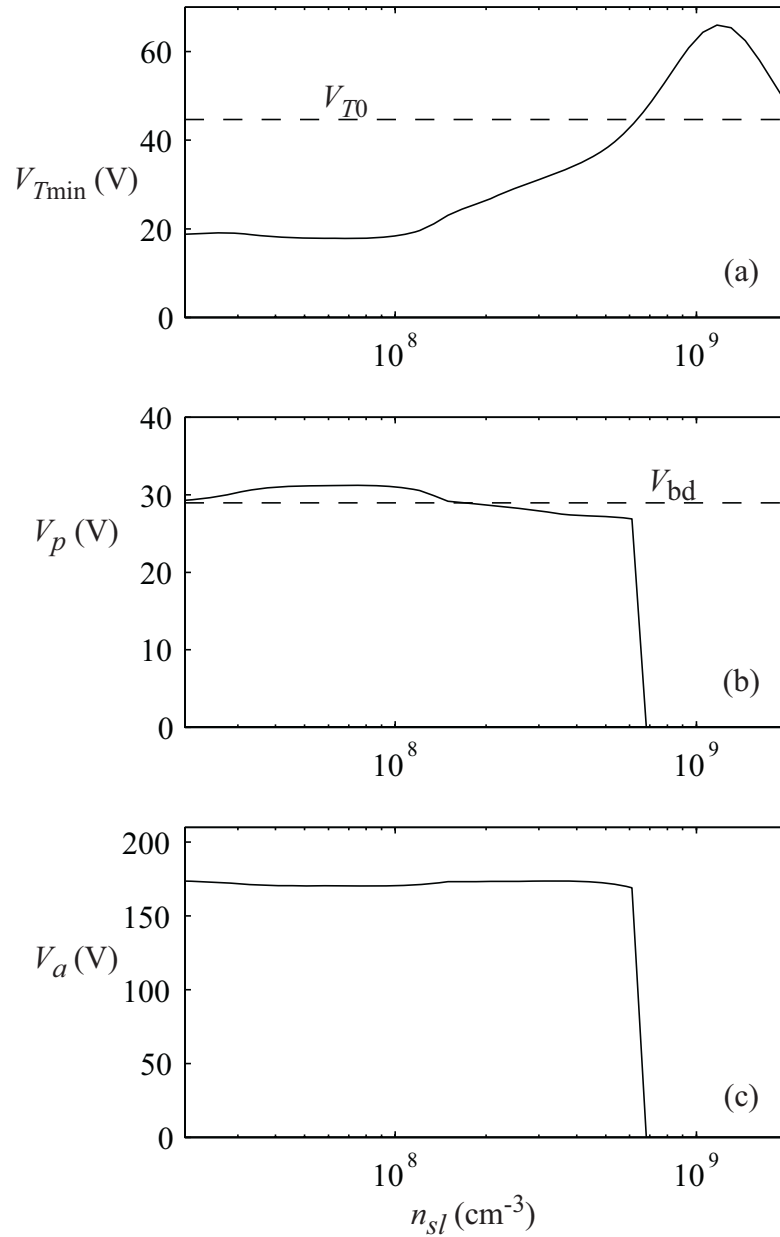


Figure 7.25. Voltages $V_{T\text{res}}$ (a), V_p (b), and V_a (c) versus slot density n_{sl} , for the base case conditions.

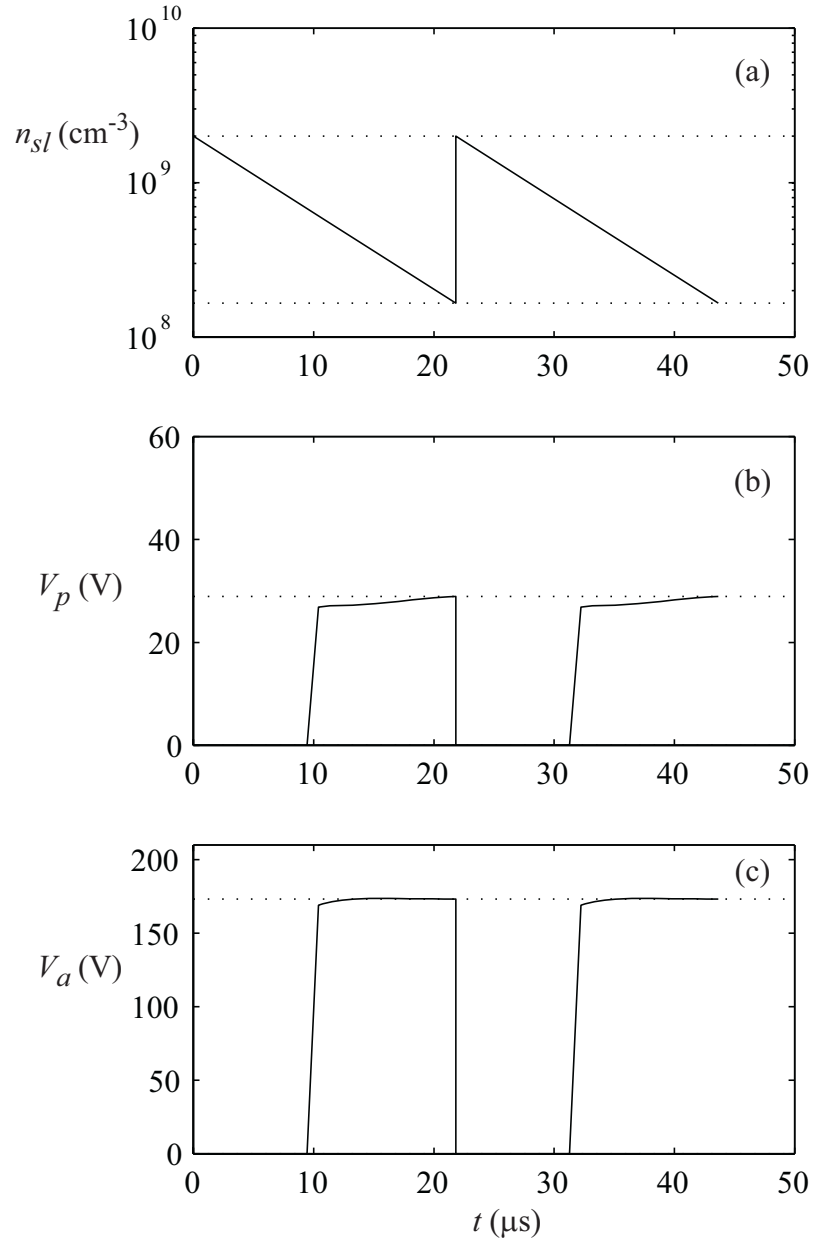


Figure 7.26. (a) Slot plasma density, (b) grounded sheath voltage V_p , and (c) powered sheath voltage V_a versus time, for the base conditions.

The time variations of n_{sl} , V_p and V_a are shown in figure 7.26. We have used a simple exponential model for the slot plasma density decay, with the timescale determined from diffusion theory to be

$$\tau_{\text{sl}} = \frac{g}{2h_{\text{gsl}}u_{\text{Bsl}}} \quad (7.27)$$

with

$$h_{\text{gsl}} = \frac{0.86}{(3 + g/\lambda_i)^{1/2}} \quad (7.28)$$

the edge-to-center density ratio in the slot. Using a reasonable slot temperature during the decay of $T_{\text{esl}} = 1$ V, we obtain $\tau_{\text{sl}} = 8.8 \mu\text{s}$. With a density decay from $n_1 = 2 \times 10^9 \text{ cm}^{-3}$ to $n_2 = 1.86 \times 10^8 \text{ cm}^{-3}$, we obtain an oscillation frequency

$$f = \frac{1}{\tau_{\text{sl}} \ln n_1/n_2} \approx 46 \text{ kHz} \quad (7.29)$$

as is seen experimentally for this case. The voltages V_p and V_a have the appearance of rectangular waveforms, with somewhat longer on-times than off-times, which depends on the particular mismatch at slot ignition.

7.5.3 Time Variations in the Main Discharge

An approximate dynamics of the main discharge can be obtained from a pulsed spatially-averaged (global) model that we have developed in part I. Using the results found in figure 7.26, a pulsed-power input can be applied, with the pulse period and on- and off-times corresponding to those calculated, and the applied power taken to be proportional to V_a . Figure 7.27 shows the calculated results for (a) the optical emission, (b) the plasma density, and (c) the electron temperature. The electron temperature rises rapidly during the on-time and decays significantly during the off-time. The average temperature during the decay is somewhat over 1 V. Corresponding to this decay in

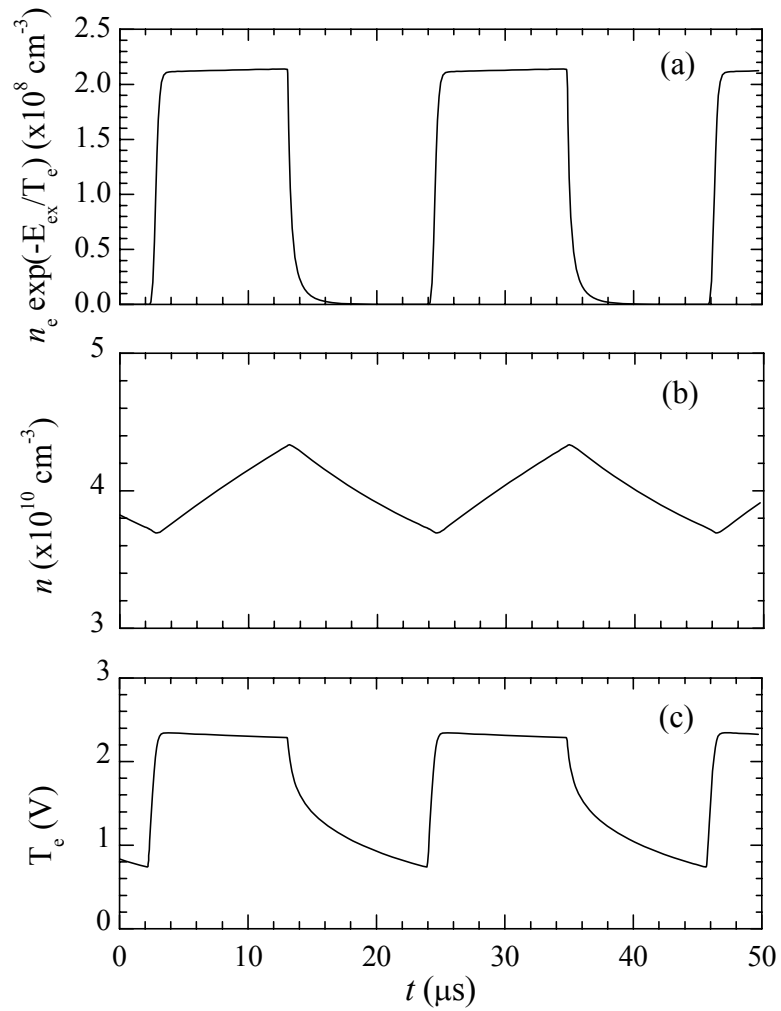


Figure 7.27. Pulsed-power calculation of (a) main discharge optical emission, (b) plasma density, and (c) electron temperature versus time, for the base case conditions.

temperature, which we take to be the common temperature in both the main discharge and the slot, the central plasma density oscillates by about 20%. The optical emission signal, taken to be proportional to $n_e \exp(-\mathcal{E}_{\text{ex}}/T_e)$ with $\mathcal{E}_{\text{ex}} \sim 11 \text{ V}$, is quite sensitive to the electron temperature, dropping to near zero during the off-time, as seen

experimentally in section 7.4. The central density is oscillating in a similar pattern as that of the experimental result for n , showing approximately a 15% reduction from the highest value. In figure 7.28, the experimental time variances of OES, central density n , and V_p measured at the corresponding condition are shown for a comparison with figure 7.27. The optical emission signal as well as the plasma density, obtained from the model,

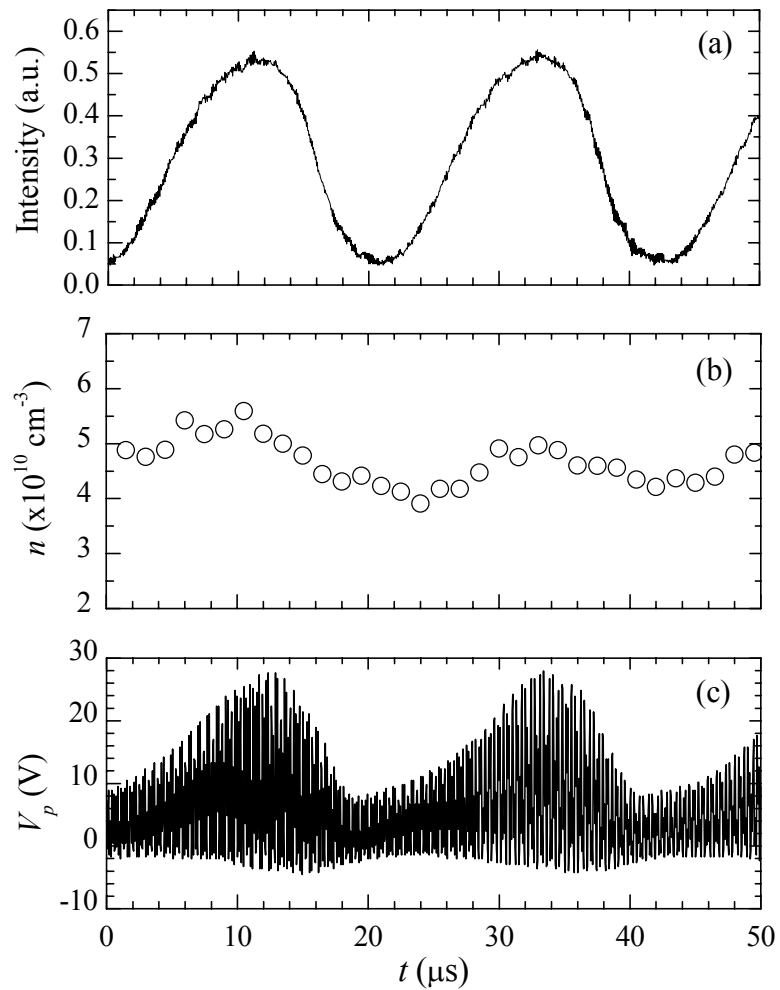


Figure 7.28. Time variations for a 46.5 kHz relaxation oscillation; $p = 100 \text{ mTorr}$, $P_{\text{fwd}} = 100 \text{ W}$, $P_{\text{refl}} = 85 \text{ W}$; (a) optical emission signal; (b) plasma density n_e ; (c) plasma potential V_p .

agree quite well with the experimental observations. Therefore, the model presented in this section qualitatively explains the experimentally observed high frequency instability.

Chapter 8

Conclusions to Part II

We have developed theories to describe plasma diffusion from a capacitive discharge into a slot, and the breakdown and maintenance of plasma in the grounded slot and a grounded peripheral pumping region. We showed that the main discharge plasma diffuses into the slot between the quartz confinement rings, forming a “finger” of plasma of length w_{po} . We found that $w_{po} \propto g$, the gap spacing, and weakly depends on the other discharge parameters. For nominal discharge conditions with $g = 0.5$ cm, an approximately 1 cm finger of plasma forms in the slot. We modified the standard one-dimensional global model for capacitive discharges to treat discharge maintenance, incorporating the additional physics required at low rf driving voltages, including both rf and dc parts to the sheath and resistive voltage drops across the sheaths and bulk plasma. We compared the maintenance condition from the modified model with measurements for a conventional 13.56 MHz discharge, finding reasonable agreement.

We examined the two-dimensional effects present in a confined dual frequency geometry, including wave propagation, radial rf current flows, and capacitive voltage drops across the width of the quartz confinement rings. We incorporated these into the model, and used it to determine the maintenance conditions for the slot and peripheral plasma at 27.12 MHz. We found that, depending on the discharge conditions, either

maintenance of the slot plasma or of the periphery plasma determines the loss of confinement in the system.

We designed and constructed a capacitive discharge with quartz confinement ring to experimentally measure the conditions for loss of confinement. The experimental setup includes diagnostics such as optical emission spectroscopy, Langmuir probe, floating potential ring probe, and Z-Scan RF probe. Measurements at 27.12 MHz and a relatively wide gap spacing of 0.635 cm gave results in reasonable agreement with the theory. A significant voltage hysteresis exists in the loss of confinement, i.e., between the ignition of the peripheral and slot plasmas and the recovery of the confinement, which are understandable from the theory. We believe that the theory qualitatively explains the observations, made both in our experiment and in a commercial reactor of a similar configuration, of transitions between conditions in which the plasma is confined to the central discharge, and conditions in which plasma also exists in the peripheral grounded regions.

We also discovered instabilities associated with the loss of confinement in both the kilohertz and hertz frequency range. We conclude that the kilohertz oscillations observed in the central plasma and in the slot connected to the peripheral chamber, at voltages below that at which the peripheral plasma ignites, are essentially understood as an instability induced by the increased resistance and capacitance of the discharge when the slot plasma ignites. The transient ignition of the slot plasma increases the capacitance of the plasma to ground and lowers the system Q in such a way that the overall equilibrium is lost. This causes the voltage across the discharge to drop dramatically, causing the electron temperature to also drop. The main discharge density

correspondingly decays but at a slower rate, until the faster decay of the slot plasma density re-ignites the discharge, repeating the scenario. The oscillation frequency as well as the shapes of the light emission signal and plasma density, obtained from the model, agree reasonably well with the corresponding experimental observations.

Chapter 9

Discussions and Suggestions for Future Work

The improved global model for electronegative discharges developed in this work showed good agreement with the experimental results in steady state oxygen discharges. Also the solutions for pulsed-power discharges suggests that the ratio of neutral flux to positive ion flux (Γ_0/Γ_+) can be controlled by varying the pulse period and the duty ratio of the modulation pulse. This controllability of the flux ratio calculated from the model should be verified by comparison to experimental results.

Using the techniques we applied in this work for an oxygen discharge, global models for other electronegative gases can also be developed. Accurate data for chemical reaction sets, the rate coefficients of each reaction, and wall recombination rates are required to make the model and its simulated results agree with experimental results. With the appropriate data, the global model can be applied to most of the plasma processing applications used in semiconductor processing.

The experimental results presented in this work show reasonable agreement with the theory for peripheral ignition at 27.12 MHz and a relatively wide gap spacing of 0.635 cm. However, we couldn't reach the breakdown condition with the narrower gap

spacings due to the limitation of rf power supply. Although this could be considered as consistent with the theory, it makes the experimental verification of theory incomplete. To verify the effect of gap spacing on the ignition conditions of slot and periphery, experiments on the discharge ignition and maintenance with the narrower gap spacings must be carried out using an rf source capable of higher power output. Systematic experiments might also be performed with a commercial chamber equipped with the confinement rings.

A range of behavior associated with the ignition of peripheral plasma has been found experimentally, and have also been seen theoretically in the model. These include, in the range of kilohertz frequencies, cases in which the main plasma does not fully extinguish. The observation of kilohertz oscillations in the peripheral region, but without fully sustaining a peripheral plasma, has also been observed experimentally. We have not analyzed this situation, which only occurs over a narrow range of parameters, but the phenomenon can be qualitatively understood within the theory.

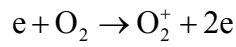
The relaxation oscillations, which depend nonlinearly on having two states for the discharge, have some resemblance to the relaxation oscillations which have been reported in previous studies in electronegative discharges [60,61]. In that situation there was a separation of timescales of the electrons and negative ions that controlled the frequency and amplitude of the instability, with the slowest timescale for decay of the negative ion density essentially controlling the frequency. For the configuration under study here, there is also a separation of timescales, with an assumed fast ionization time for ignition of the slot plasma, and with a slower timescale for plasma decay in the slot controlling the oscillation frequency. In both situations, the matching network dynamics has been

found to play an important role in the instability dynamics. A systematic study of the instability associated with the peripheral plasma, as a function of the degree of matching, needs to be undertaken to fully understand the detailed mechanisms involved.

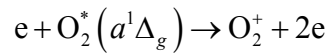
Appendix A

Reactions and Rate Coefficients for Oxygen

Electron impact ionization of the oxygen molecule in the ground state



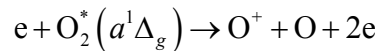
has a rate coefficient (m^3/s) of $2.34 \times 10^{-15} T_e^{1.03} \exp(-12.29/T_e)$, which is calculated from the cross section measured by Krishnakumar and Srivastava [31]. For electron impact ionization of the metastable oxygen molecule $O_2^*(a^1\Delta_g)$



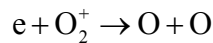
we assume that the same process takes place except the threshold energy is lowered by 0.98 eV. Electron impact dissociative ionization of the oxygen molecule



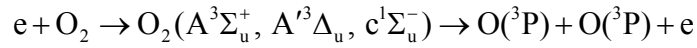
has rate coefficient of $1.88 \times 10^{-16} T_e^{1.699} \exp(-16.81/T_e)$, which is calculated from the cross section measured Krishnakumar and Srivastava [31]. For electron impact dissociative ionization of the metastable oxygen molecule $O_2^*(a^1\Delta_g)$



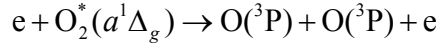
we assume that the same process takes place except the threshold energy is lowered by 0.98 eV. The rate coefficient for the recombination of O_2^+ ions with electrons



is determined by assuming a rate coefficient of the form $K = K_0 T_e^{-0.5}$ and fitting to the data measured by Mehr and Biondi [62] from 1700 K to 5000 K. We propose a rate coefficient of $2.2 \times 10^{-14} T_e^{-0.5}$ for the conditions $1 < T_e < 7$ V expected in processing discharges. We use a dissociation cross section that is inferred from the electronic excitation cross sections. Excitation from the ground state favors a process leading to dissociation via an electronic transition to the Herzberg states

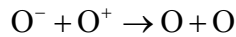


which has a threshold of 6.0 V and rate coefficient of $6.86 \times 10^{-15} \exp(-6.29/T_e)$. The rate coefficient for dissociation of the metastable oxygen molecule $O_2^*(a^1\Delta_g)$ by electron impact



is found by applying threshold reduction.

Recent measurements of the mutual neutralization cross sections in oxygen have suggested that the rate coefficients commonly used are significantly overestimated [63,64]. For mutual neutralization of O^+ by O^-



we use the cross section recently measured by Hayton and Peart [63]. Their measurement is supported by a recent theoretical calculation of the cross section by Zhou and Dickinson [65] that is in excellent agreement with the cross section measured. Unfortunately, the measured and calculated data do not go below 1 eV. Therefore, we assume that the scaling with T_i of the theoretical value calculated by Olson [66] is qualitatively correct for energies below 1 eV. This scaling is consistent with the classical

Coulomb focusing expected at low energies. Thus, we use the cross section calculated by Olson [66] and scale it down by a factor of 6.4 to fit the measured data of Hayton and Peart [63]. We then extrapolate the cross section down to 0.001 eV. Using this cross section we calculate a rate coefficient by assuming a Maxwellian energy distribution of the ions in the range $300 \text{ K} \leq T_i \leq 1200 \text{ K}$. The rate coefficient for the mutual neutralization of $\text{O}^- + \text{O}^+$ is thus found to be $4.0 \times 10^{-14} (300/T_i)^{0.43}$, with T_i in kelvins.

For mutual neutralization of O_2^+ by O^-



and

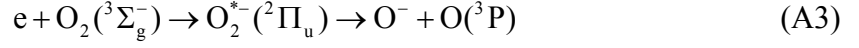


we use recent measurements of the cross section by Padgett and Peart [64]. Their measurements indicate that reactions (A1) and (A2) each contribute roughly 50% at 120 eV. Since their measurements are made for energies above 6 eV, we use the cross section calculated by Olson [66] and scale it down by a factor of 5.0 to fit the measured data of Padgett and Peart [64]. We then extrapolate the cross section down to 0.001 eV. Using this cross section we calculate a rate coefficient by assuming Maxwellian energy distribution of the ions. The total rate coefficient for the mutual neutralization of $\text{O}^- + \text{O}_2^+$ is thus $5.2 \times 10^{-14} (300/T_i)^{0.44}$ and is valid in the range $300 \text{ K} \leq T_i \leq 1200 \text{ K}$.

The data of Eliasson and Kogelshatz [28] indicates a 50–70% range as the ratio of reactions (A1) and (A2). Based on this and the data of Padgett and Peart [64], we assume that each reaction contributes 50% to the reaction rate, we propose a rate coefficient of $2.6 \times 10^{-14} (300/T_i)^{0.44}$ for each of the reactions (A1) and (A2).

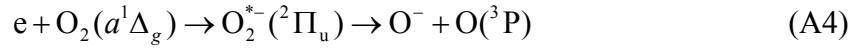
The rate coefficients for the dissociative electron attachment to the oxygen molecule are calculated from the cross sections measured by Jaffke *et al.* [32]

Dissociative electron attachment to the ground state oxygen molecule



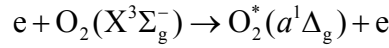
has a rate coefficient $1.07 \times 10^{-15} T_e^{-1.391} \exp(-6.26/T_e)$. Dissociative electron attachment to

the singlet delta state oxygen molecule

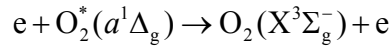


has a rate coefficient $4.19 \times 10^{-15} T_e^{-1.376} \exp(-5.19/T_e)$.

The electronic excitation to the metastable oxygen molecule $O_2^*(a^1\Delta_g)$ from the ground state

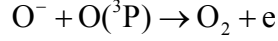


has a rate coefficient of $1.37 \times 10^{-15} \exp(-2.14/T_e)$, which is calculated from the cross section data compiled by Phelps [29]. The rate coefficient for deexcitation of metastable oxygen molecule $O_2^*(a^1\Delta_g)$ by electron impact



is estimated using the principle of detailed balancing. The ground state of molecular oxygen is $^3\Sigma_g^-$ and has $3 \times 1 = 3$ degenerate states and the $a^1\Delta_g$ state has $1 \times 2 = 2$ degenerate states. The threshold energy for the reverse process is 0.977 eV. Thus $(3/2) \times 1.37 \times 10^{-15} \exp(-2.14/T_e) \exp(0.977/T_e)$ gives a rate coefficient of $2.06 \times 10^{-15} \exp(-1.163/T_e)$.

The rate coefficient for associative detachment by oxygen atom



was recently measured by Belostotsky *et al.* [33] as $(1.6 \pm 0.3) \times 10^{-16}$. The rate coefficient for the detachment by collision of oxygen ion O^- with metastable oxygen molecules $\text{O}_2^*(a^1\Delta_g)$



is taken to be 3.3×10^{-17} from the measurements of Upschulte *et al.* [34]. This rate coefficient was more recently measured by Belostotsky *et al.* [33] as $(1.3 \pm 0.3) \times 10^{-16}$. This value is somewhat lower than the earlier measurements of Fehsenfeld *et al.* [67] which reported a value of 3×10^{-16} . We assume that the products in (A5) are either $\text{O}_3 + \text{e}$ or $\text{O}_2^- + \text{O}$, with subsequent rapid reactions for dissociation of O_3 to produce $\text{O}_2 + \text{O}$ and for detachment of O_2^- to produce $\text{O}_2 + \text{O}$. Thus we assign a rate coefficient 3.3×10^{-17} to the overall reaction



Appendix B

An Analysis on the Propagation Characteristics in the Slot

We use a simple quasistatic analysis to determine the propagation characteristics in the slot. Quasistatic wave analysis is a good approximation if the transverse wavenumber is large compared to the neglected free space wavenumber. We consider a uniform density plasma slab of thickness $2l_p$ lying between two dielectric slabs, each having thickness l_q . Choosing the x -axis to lie along the plasma-dielectric interface, with the plasma located at $0 > z > -l_p$ and the top dielectric at $0 < z < l_q$, then the potentials for a single, symmetrically-excited quasistatic wave propagating along x are

$$\Phi_p = A_p e^{-jkx} \cosh k(l_p + z), \quad \Phi_q = A_q e^{-jkx} \sinh k(l_q - z), \quad (\text{B1})$$

where k is the (complex) propagation constant for the wave. The wave amplitude has its maximum value at the plasma-dielectric interface $z = 0$, decaying both into the plasma and into the dielectric, and is therefore known as a *surface wave*. The z -components of the electric fields are

$$E_{zp} = -kA_p e^{-jkx} \sinh k(l_p + z), \quad E_{zq} = kA_q e^{-jkx} \cosh k(l_q - z). \quad (\text{B2})$$

Using the boundary conditions at $z = 0$ that $\Phi_p = \Phi_q$ and that $\kappa_p E_{zp} = \kappa_q E_{zq}$, where κ_p and κ_q are the relative dielectric constants of the plasma and insulator, we obtain the dispersion relation for the waves

$$-\kappa_p \tanh kl_p = \kappa_q \coth kl_q. \quad (\text{B3})$$

Assuming that the characteristic wavelength $2\pi/|k|$ is long compared to plasma and dielectric thicknesses, we can expand the cosh and sinh functions to obtain

$$k^2 = -\frac{\kappa_p}{\kappa_q} \frac{1}{l_q l_p}. \quad (\text{B4})$$

For $p \geq 100$ mTorr and $f = 27.12$ MHz, the plasma is collisional ($\nu_m \gg \omega$), and from (6.29) we approximate $\kappa_p \approx -j\omega_p^2/\omega\nu_m$. Inserting this into (B4), we obtain

$$k = \frac{1+j}{\sqrt{2}} \left(\frac{\kappa_q}{l_p l_q} \frac{\omega\nu_m}{\omega_p^2} \right)^{1/2}. \quad (\text{B5})$$

Consider a situation in which a plasma is maintained in the slot with the peripheral plasma not ignited. This corresponds to an open-circuited boundary condition at the slot exit $x = 0$. The incident wave then excites a reflected wave at the slot exit. The sum of incident and reflected waves yields a standing wave along x , for which the exponential factor e^{-jkx} in (B1) is replaced by the factor $\cos kx$, corresponding to a zero-derivative of the voltage with respect to x at the open circuit. Then the ratio of the exit-to-entrance voltage is $|\sec kw|$, with k still given by (B5).

As an example, we estimate the voltage ratio for maintenance of a slot plasma of length $w = 3$ cm under open-circuited conditions at 200 mTorr. The maintenance density is $n \approx 10^9$ cm⁻³, the collision frequency is $\nu_m \approx 3.3 \times 10^8$ s⁻¹, and the radian frequency is 1.76×10^8 s⁻¹, yielding $\omega_p^2/\omega\nu_m \approx 55.1$. We assume a slot thickness of 0.5 cm that is half-filled with plasma, corresponding to $l_p = 0.125$ cm, and we take $l_q = l/2 = 1.5$ cm. Then (B5) yields $k \approx 0.44(1+j)$ cm⁻¹, and the voltage ratio is $|\sec kw| \approx 0.57$. At 100 mTorr,

n is about a factor of two higher, and ν_m is a factor of two lower, yielding $k \approx 0.22(1+j)\text{cm}^{-1}$, and $|\sec kw| \approx 0.94$. Hence for this example the voltage is reasonably uniform in the slot for pressures less than about 200 mTorr.

The preceding results are for a quasistatic analysis. We have compared this analysis to a more complete analysis based on the full set of electromagnetic equations. Considering the symmetrically-excited wave, rather than the antisymmetrically-excited wave, but proceeding as in Lieberman *et al.* [59], the dispersion relation (B3) becomes

$$-\alpha_q \kappa_p \tanh \alpha_p l_p = \alpha_p \kappa_q \coth \alpha_q l_q \quad (\text{B6})$$

with

$$\alpha_p^2 = k^2 - k_0^2 \kappa_p, \quad (\text{B7})$$

$$\alpha_q^2 = k^2 - k_0^2 \kappa_q, \quad (\text{B8})$$

where α_p and α_q are the transverse wavenumbers in the plasma and quartz dielectric, and $k_0 = \omega/c$ is the free space wavenumber. Equation (B6) for the symmetric wave is analogous to the antisymmetric wave result (17) of [59], with (B7) and (B8) identical to (13) and (14) in [59]. Taking the quasistatic ($c \rightarrow \infty$) limit $k \gg k_0 \sqrt{-\kappa_p}$, $k_0 \sqrt{\kappa_q}$ in (B6)–(B8) yields (B3). Using the estimates of k from the preceding paragraph, we find that the quasistatic limit is well-satisfied for the range of parameters of interest.

Equation (B3) (or (B6)–(B8) if the quasistatic approximation is not valid) can also be applied to estimate the radial non-uniformity of the voltage in the peripheral region. However, the peripheral density is typically $\gtrsim 10^{10} \text{cm}^{-3}$, at least one order of magnitude larger than the maintenance density in the slot, yielding, from (B5), smaller values of k , and hence weaker radial nonuniformities. For example, evaluating (B5) with

$n_{\text{per}} = 10^{10} \text{ cm}^{-3}$, $l_p = 1.5 \text{ cm}$, $\kappa_q = 1$, and $l_q = 0.3 \text{ cm}$ (the vacuum sheath region) yields $k \sim 0.045(1+j) \text{ cm}^{-1}$ at 200 mTorr. With $w_{\text{per}} = 3 \text{ cm}$, the radial voltage drop in the periphery is about one order of magnitude lower than in the slot.

Radial standing waves, skin effects, and various edge effects can also exist in the high density main discharge [47,59,68-70]. Field [59] or transmission line [47,68-70] analyses can be used to estimate the radial voltage non-uniformities. At 27.12 MHz and for typical silicon processing discharge radii ($R \sim 12 \text{ cm}$), the non-uniformities are not large. In any case, the rf voltage to be used for the breakdown analysis presented in this work is that at the slot entrance at $r = R$. The reader should consult the works referenced above for a treatment of possible voltage non-uniformities in the main discharge.

Appendix C

MATLAB Codes for Simulations

File name: New_model_ODE.m

```
%%%%%%%%%%%%%%%%%%%%%%%%%%%%%%%%%%%%%%%%%%%%%%%%%%%%%%%%%%%%%%%%%%%%%%%%%
% Integrate ODE's for global oxygen with new h_l factors
% Using the differential equations with average densities
% assumption of parabolic profiles for neutrals
% including O2, O2+, O+, O-, O & O2*
% Reaction coefficients have been corrected.
% Code to compare with Kimura's steady state exp data
% decreasing gamma_O & localized ionization
% Last modification 11-30-2005
% by Sungjin Kim
% Department of Electrical Engineering and Computer Sciences
% University of California, Berkeley
%%%%%%%%%%%%%%%%%%%%%%%%%%%%%%%%%%%%%%%%%%%%%%%%%%%%%%%%%%%%%%%%%%%%%%%%%
clear all
global ee me MO MO2 ng Tg Ti l_p gamma0 gamma02m
global Efactor_O2 Efactor_O EnergyO2 sigO2 EnergyO sigO
global Krec Krec2 Krec3 Krec4 Kdet Kch Rlambda hl0 Rrec alphabar
global pabs R area volume QtorrLit Qmolec Kpump scat_Xsec
ee=1.6022E-19;
me=9.1095E-31;           % mass of electron
MO=1836*16*me;          % mass of an Oxygen atom
MO2=2*MO;               % mass of an Oxygen Molecule
Tg=0.052;               % 600K in volts
Ti=Tg;
gamma02m=0.007          % wall recombination rate of meta-stable Oxygen
R=0.08                  % reactor radius
L=0.075                % reactor length
l_p=L/2;               % half length
area=2*pi*R*(R+L);     % total surface area
volume=pi*R^2*L;       % reactor volume
Efactor_O=2+0.5*(1+log(MO/(2*pi*me))); % (E_e+E_i_O)/Te
Efactor_O2=2+0.5*(1+log(MO2/(2*pi*me))); % (E_e+E_i_O2)/Te
% Loading all cross-section data to calculate Kel & Ec
load o2cross.txt -ASCII;
EnergyO2 = o2cross(:,2);
sigmaO2 = o2cross(:,3);
sigO2 = sigmaO2 * 1e-20;
load Ocross.txt -ASCII;
EnergyO = Ocross(:,1);
sigmaO = Ocross(:,2);
sigO = sigmaO * 1e-20;
% power input
Pabs=180                % total absorbed power in watts [adjustable]
```

```

pabs=Pabs/(ee*volume);
% starting pressures in mTorr (180W)
ppvec=[6.02 13.06 21.81 30.60 34.86 43.64 52.09 60.75]
Qvec=[40 50 50 50 50 50 50 50] % O2 flow rate in sccm
% atomic oxygen surface recombination rate
gammaOvec=[0.5 0.43 0.33 0.27 0.23 0.2 0.15 0.13]
allresults=zeros(35,length(ppvec)); % number of items to save=35
for ii=1:length(ppvec)
gamma0=gammaOvec(ii)
p=ppvec(ii)
Qsccm=Qvec(ii)
QtorrLit=Qsccm/79.05; % sccm to Torr-Liter/sec
Qmolec=4.483e17*Qsccm; % sccm to molecules/sec
Kpump=2*QtorrLit/(p*volume); % Pumping Rate coefficient
ng0=3.3E19*p*0.026/Tg; % m^-3
ng0_cm=ng0*1e-6 % cm^-3
scat_Xsec=7.5e-19; % elastic scattering cross-section for Oxygen in m^2
% heavy particle reaction rates
Krec=2.6E-14*sqrt(0.026/Tg);
Krec2=2.6E-14*sqrt(0.026/Tg);
Krec3=4.0E-14*sqrt(0.026/Tg);
Krec4=3.3E-17;
Kdet=1.6E-16;
Kch=2.0E-17*sqrt(0.026/Tg);
%
t0=0;
tf=90;
nO2plusbar0=2E16
nOplusbar0=1E16
nOminusbar0=3E15
nObar0=2E17
nO2mbar0=0.01*ng0
nO20=ng0-nObar0-nO2mbar0
Te0=2
pe0=1.5*(nO2plusbar0+nOplusbar0-nOminusbar0)*Te0
v0=[nO20 nO2plusbar0 nOplusbar0 nOminusbar0 nObar0 nO2mbar0 pe0];
[t v]=ode23s('new_oxys_diss_iz', [t0 tf], v0);
nO2=v(:,1);
nO2plusbar=v(:,2);
nOplusbar=v(:,3);
nOminusbar=v(:,4);
ne0=nO2plusbar+nOplusbar-nOminusbar;
nObar=v(:,5);
nO2mbar=v(:,6);
Te=v(:,7)./(1.5.*ne0);
% getting the data at the final equilibrium
final_nO2=nO2(end);
n_O2=final_nO2*1e-6 % in cm^-3
final_nO2plusbar=nO2plusbar(end);
n_O2plus_bar=final_nO2plusbar*1e-6 % in cm^-3
final_nOplusbar=nOplusbar(end);
n_Oplus_bar=final_nOplusbar*1e-6 % in cm^-3
final_nOminusbar=nOminusbar(end);
n_Ominus_bar=final_nOminusbar*1e-6 % in cm^-3
final_ne0=ne0(end);
n_e0=final_ne0*1e-6 % in cm^-3
n_e0_2=n_e0/1e10;

```

```

final_nObar=nObar(end);
n_0_bar=final_nObar*1e-6 % in cm^-3
final_nO2mbar=nO2mbar(end);
n_O2m_bar=final_nO2mbar*1e-6 % in cm^-3
final_ng=final_nO2+final_nObar+final_nO2mbar;
n_g=final_ng*1e-6 % in cm^-3
final_Te=Te(end)
final_Ti=Ti
final_Ec_O2=o2_ec(final_Te)
final_Ec_O=o_ec(final_Te)
final_p=final_ng/3.3e19*(Tg/0.026) % final pressure in mTorr
% ratio for density weighting
nOp_ratio=final_nOplusbar/(final_nO2plusbar+final_nOplusbar);
% plotting the results
figure(ii)
subplot(7,1,1)
plot(t,nO2plusbar,t, ne0,'--')
ylabel('n_{O_2}^{+}, n_{e0} (m^{-3})')
axis([0 inf 0 final_nO2plusbar*1.5])
title(['Flowrate=',num2str(Qscm),'scm, P_{abs}=',num2str(Pabs),...
      'W, p_0=',num2str(p),'mTorr, p_f=',num2str(round(final_p)),...
      'mTorr'])
subplot(7,1,2)
plot(t,nOplusbar)
ylabel('n_{O^{+}} (m^{-3})')
axis([0 inf 0 final_nOplusbar*1.5])
subplot(7,1,3)
plot(t,nOminusbar)
ylabel('n_{O^{-}} (m^{-3})')
axis([0 inf 0 final_nOminusbar*1.5])
subplot(7,1,4)
plot(t,nObar)
ylabel('n_O (m^{-3})')
axis([0 inf 0 final_nObar*1.5])
subplot(7,1,5)
plot(t,nO2mbar)
ylabel('n_{O_2}^{*} (m^{-3})')
axis([0 inf 0 final_nO2mbar*1.5])
subplot(7,1,6)
plot(t,nO2)
ylabel('n_{O_2} (m^{-3})')
axis([0 inf 0 final_nO2*1.5])
subplot(7,1,7)
plot(t,Te)
xlabel('t (sec)')
ylabel('T_e (m^{-3})')
axis([0 inf 0 final_Te*1.5])
% caculating values for O neutral & O2m
lambda=1/(final_ng*scat_Xsec) % lambda in m
vbarO=sqrt(8*ee*Ti/(pi*MO)) % average thermal velocity of O neutral
vbarO2m=sqrt(8*ee*Ti/(pi*MO2)) % average thermal velocity of O2m
DO=ee*Tg*lambda/vbarO/MO % Diffusion coefficient of O neutral
DO2m=ee*Tg*lambda/vbarO2m/MO2 % Diffusion coefficient of O2m
dO=sqrt(4*DO*1_p*(2-gammaO)/vbarO/gammaO + 1_p^2);
dO2m=sqrt(4*DO2m*1_p*(2-gammaO2m)/vbarO2m/gammaO2m + 1_p^2);
hAO=1/(1 + 1_p*vbarO*gammaO/4/DO/(2-gammaO))
hAO2m=1/(1 + 1_p*vbarO2m*gammaO2m/4/DO2m/(2-gammaO2m))

```

```

vol_0=volume*(1 - l_p^2/(3*d0^2))*(1 - (2/3)*l_p^3/(R*d0^2)...
    + l_p^4/(6*R^2*d0^2));
vol_02m=volume*(1 - l_p^2/(3*d02m^2))*(1 - (2/3)*l_p^3/(R*d02m^2)...
    + l_p^4/(6*R^2*d02m^2));
vr_0=vol_0/volume
vr_02m=vol_02m/volume
% calculation of the final alpha0
Tplusf=Ti;
Tminusf=Ti;
gamma_plusf=final_Te/Tplusf;
gamma_minusf=final_Te/Tminusf;
etaf=2*Tplusf/(Tplusf+Tminusf);
hl0=0.86/sqrt(3+etaf*l_p/lambda);
Rlambda=sqrt(2*pi/gamma_plusf)*lambda/l_p/etaf;
final_uB_02=sqrt(ee*final_Te/MO2);
final_uB_0=sqrt(ee*final_Te/MO);
% density-weighted Bohm velocity in m/s
final_uB_dw=final_uB_02*(1-nOp_ratio)+final_uB_0*nOp_ratio;
% density-weighted Recombination rate coefficient
Krec_dw_f=(Krec+Krec2)*(1-nOp_ratio)+Krec3*nOp_ratio;
Rrec=Krec_dw_f*final_ne0*l_p/final_uB_dw;
alphabar=final_nOminusbar/final_ne0
alpha0=fzero('alpha0find',[1e-2 1e2]) % final alpha0
volumeminus=vol_minus(alpha0);
final_nOminus=final_nOminusbar*volume/volumeminus;
final_nplus=final_nOminus + final_ne0;
final_nOplus=final_nplus*nOp_ratio;
final_nO2plus=final_nplus-final_nOplus;
final_nO=final_nObar*volume/vol_0;
final_nO2m=final_nO2mbar*volume/vol_02m;
n_02plus=final_nO2plus*1e-6 % in cm^-3
n_Oplus=final_nOplus*1e-6 % in cm^-3
n_Ominus=final_nOminus*1e-6 % in cm^-3
n_0=final_nO*1e-6 % in cm^-3
n_02m=final_nO2m*1e-6 % in cm^-3
% calculation of final hl factor
% density weighted positive ion mass
Mplus_dw=MO2*(1-nOp_ratio)+MO*nOp_ratio;
nstarf=15/56*sqrt(8*ee*Tplusf/pi/Mplus_dw)*(etaf^2)/(Krec_dw_f*lambda);
hpar2f=hl0*1/(1+alpha0);
hpar1f=1/(gamma_minusf^0.5 + (gamma_plusf^0.5)...
    *(etaf*l_p/sqrt(2*pi)/lambda))*(alpha0/(1+alpha0));
hflat1f=1/(gamma_minusf^0.5 + (gamma_plusf^0.5)*(nstarf^0.5)...
    /(final_nOminus^0.5));
%overall hl factor by "linear ansatz"
final_hl=hpar2f + hpar1f + hflat1f
% size of EN core (lminus & rminus)
final_lminus=lminus(alpha0); %in m
lminus=final_lminus*1e2 % in cm
final_rminus=R - l_p + final_lminus; %in m
rminus=final_rminus*1e2 % in cm
lminus_over_l_p=final_lminus/l_p
vratio=volumeminus/volume;
vol_rec=(2*pi*final_lminus/(1+alpha0))*(8/15*alpha0*...
    (final_rminus^2 - 14/15*final_rminus*final_lminus...
    + 4/15*final_lminus^2) + 2/3*(final_rminus^2 - 2/3...
    *final_rminus*final_lminus + 1/6*final_lminus^2));

```

```

vrec_ratio=vol_rec/volume;
% ion flux
dissociation_rate = final_nObar/final_ng
nplus_flux=final_hl*final_nplus*final_uB_dw*1e-4 % in /cm^2/s
nO_flux=hA0*final_nO*vbarO/4*1e-4 % in /cm^2/s
flux_ratio=nO_flux/nplus_flux
lambda_cm=lambda/1e-2 % in cm
% save results
allresults(:,ii)=[p;final_p;Pabs;ng0_cm;n_g;n_O2plus;n_Oplus;...
n_Ominus;n_e0;n_e0_2;n_O;n_O2m;n_O2plus_bar;n_Oplus_bar;...
n_Ominus_bar;n_O_bar;n_O2m_bar;n_O2;final_Te;final_Ec_O2;...
final_Ec_O; alpha0;alphabar;gamma_plusf;final_hl;...
lminus_over_l_p;Rminus;Lminus;vratio;vrec_ratio;...
lambda_cm;dissociation_rate;nplus_flux;nO_flux;flux_ratio];
end
% save results to a file
filename=[num2str(Pabs),'W_results.txt']
save(filename,'allresults','-ASCII','-double');

```

File name: new_oxys_diss_iz.m

```

%%%%%%%%%%%%%%%%%%%%%%%%%%%%%%%%%%%%%%%%%%%%%%%%%%%%%%%%%%%%%%%%%%%%%%%%
% Differential equations with average densities
% Integrate ODE's for global oxygen with new h_l factors
% Using the differential equations with average densities
% assumption of parabolic profiles for neutrals
% including O2, O2+, O+, O-, O & O2*
% Reaction coefficients have been corrected.
% decreasing gamma_O & localized ionization
% Last modification 11-30-2005
% by Sungjin Kim
% Department of Electrical Engineering and Computer Sciences
% University of California, Berkeley
%%%%%%%%%%%%%%%%%%%%%%%%%%%%%%%%%%%%%%%%%%%%%%%%%%%%%%%%%%%%%%%%%%%%%%%%
function vdot=new_oxys_diss_iz(t,v)
global ee me MO MO2 ng Tg Ti l_p gamma0 gammaO2m Efactor_O2
global Efactor_O EnergyO2 sigO2 EnergyO sigO
global Krec Krec2 Krec3 Krec4 Kdet Kch Rlambda hl0 Rrec alphabar
global pabs R area volume QtorrLit Qmolec Kpump scat_Xsec
vdot=zeros(7,1);
nO2=v(1);
nO2plusbar=v(2);
nOplusbar=v(3);
nOminusbar=v(4);
nObar=v(5);
nO2mbar=v(6);
pe=v(7);
ng=nO2+nObar+nO2mbar;
ne0=nO2plusbar+nOplusbar-nOminusbar;
Te=pe/(1.5*ne0);
Tplus=Ti;
Tminus=Ti;
gamma_plus=Te/Tplus;
gamma_minus=Te/Tminus;
% ratio for density weighting

```

```

nOplus_ratio=nOplusbar/(nO2plusbar+nOplusbar);
% calculating lambda
% old way --> lambda=1/(330*p*1e-3)*1e-2; % in m
lambda=1/(ng*scat_Xsec); % lambda in m
% caculating values for O neutral & O2m
vbarO=sqrt(8*ee*Ti/(pi*MO)); % average thermal velocity of O neutral
vbarO2m=sqrt(8*ee*Ti/(pi*MO2)); % average thermal velocity of O2m
DO=ee*Tg*lambda/vbarO/MO; % Diffusion coefficient of O neutral
DO2m=ee*Tg*lambda/vbarO2m/MO2; % Diffusion coefficient of O2m
dO=sqrt(4*DO*1_p*(2-gammaO)/vbarO/gammaO + 1_p^2);
dO2m=sqrt(4*DO2m*1_p*(2-gammaO2m)/vbarO2m/gammaO2m + 1_p^2);
hAO=1/(1 + 1_p*vbarO*gammaO/4/DO/(2-gammaO));
hAO2m=1/(1 + 1_p*vbarO2m*gammaO2m/4/DO2m/(2-gammaO2m));
% wall recombination loss rate for O neutral
KO=hAO*vbarO*2*gammaO/(2-gammaO)*area/volume/4;
% wall recombination loss rate for O2m
KO2m=hAO2m*vbarO2m*2*gammaO2m/(2-gammaO2m)*area/volume/4;
vol_O=volume*(1 - 1_p^2/(3*dO^2))*(1 - (2/3)*1_p^3/(R*dO^2)...
+ 1_p^4/(6*R^2*dO^2));
vol_O2m=volume*(1 - 1_p^2/(3*dO2m^2))*(1 - (2/3)*1_p^3/(R*dO2m^2)...
+ 1_p^4/(6*R^2*dO2m^2));
%finding alpha0
eta=2*Tplus/(Tplus+Tminus);
hl0=0.86/sqrt(3+eta*1_p/lambda);
Rlambda=sqrt(2*pi/gamma_plus)*lambda/1_p/eta;
uB_O2=sqrt(ee*Te/MO2);
uB_O=sqrt(ee*Te/MO);
% density-weighted Bohm velocity
uB_dw=uB_O2*(1-nOplus_ratio)+uB_O*nOplus_ratio;
% density-weighted Recombination rate coefficient
Krec_dw=(Krec+Krec2)*(1-nOplus_ratio)+Krec3*nOplus_ratio;
Rrec=Krec_dw*ne0*1_p/uB_dw;
alphabar=nOminusbar/ne0;
alpha0=fzero('alpha0find',[1e-2 1e2]);
volminus=vol_minus(alpha0);
%calculating peak(center) densities
nOminus=nOminusbar*volume/volminus;
nplus=nOminus+ne0;
nOplus=nplus*nOplus_ratio;
nO2plus=nplus-nOplus;
nO=nObar*volume/vol_O;
nO2m=nO2mbar*volume/vol_O2m;
% calculation of hl factors with 3 models
% density weighted positive ion mass
Mplus_dw=MO2*(1-nOplus_ratio)+MO*nOplus_ratio;
nstar=15/56*sqrt(8*ee*Tplus/pi/Mplus_dw)*(eta^2)/(Krec_dw*lambda);
hpar2=hl0*1/(1+alpha0);
hpar1=1/(gamma_minus^0.5 +
(gamma_plus^0.5)*(eta*1_p/sqrt(2*pi)/lambda))*(alpha0/(1+alpha0));
hflat1=1/(gamma_minus^0.5 +
(gamma_plus^0.5)*(nstar^0.5)/(nOminus^0.5));
hl=hpar2 + hpar1 + hflat1; %overall hl factor by "linear ansatz"
% size of EN core (lminus & rminus)
l_minus=lminus(alpha0);
r_minus=R - 1_p + l_minus;
% Effective volume for recombination losses
vol_rec=(2*pi*1_minus/(1+alpha0))*(8/15*alpha0*(r_minus^2...

```

```

- 14/15*r_minus*l_minus + 4/15*l_minus^2) + 2/3*(r_minus^2...
- 2/3*r_minus*l_minus + 1/6*l_minus^2));
% Surface loss of electron-ion pair
Kion=hl*uB_dw*area/volume;
% other reaction coefficients
%Kiz1=2.34E-15*Te^(1.03)*exp(-12.29/Te);
Kei=2.2E-14*Te^(-0.5);
Katt=1.07E-15*Te^(-1.391)*exp(-6.26/Te);
Kiz2=9E-15*Te^(0.7)*exp(-13.6/Te);
Kdiss=6.09*6.86E-15*exp(-6.29/Te);
Kiz3=7.1E-17*Te^0.5*exp(-17/Te);
Kiz4=1.88E-16*Te^(1.699)*exp(-16.81/Te);
Kex=1.37E-15*exp(-2.14/Te);
Kizm=2.34E-15*Te^(1.03)*exp(-11.31/Te);
Kattm=4.19E-15*Te^(-1.376)*exp(-5.19/Te);
Kdeex=2.06E-15*exp(-1.163/Te);
Kdism=6.09*6.86E-15*exp(-5.31/Te);
% calculating Ec
Ec_O=o_ec(Te);
Ec_O2=o2_ec(Te);
Eei_O=Efactor_O*Te;
Eei_O2=Efactor_O2*Te;
% calculating reduction factor for volume of ionization
Kel=rateconstant( EnergyO2, sigO2, Te );
vbare=sqrt(8*ee*Te/(pi*me)); % average thermal velocity of electron
lambda_E=vbare/ng/sqrt(3*Kel*Kex);
vr_iz=1/(1 + 2*l_p/lambda_E);
Kiz1=vr_iz*2.34E-15*Te^(1.03)*exp(-12.29/Te); % reduced Kiz1
% differential EQ's
% for nO2
vdot(1)=Qmolec/volume + Krec*nO2plus*nOminus*vol_rec/volume...
+ Kdet*nOminusbar*nObar + Kdeex*nO2mbar*ne0...
+ Krec4*nO2mbar*nOminusbar + Kion*nO2plus + KO2m*nO2m...
+ 0.5*KO*nO - (Kiz1 + Katt + Kdiss + Kiz3 + Kiz4 + Kex)*nO2*ne0...
- Kch*nOplusbar*nO2 - Kpump*nO2;
% for nO2plus
vdot(2)=Kiz1*nO2*ne0 + Kizm*nO2mbar*ne0 + Kch*nOplusbar*nO2...
-(Krec + Krec2)*nO2plus*nOminus*vol_rec/volume...
- Kei*ne0*nO2plusbar - Kion*nO2plus;
% for nOplus
vdot(3)=Kiz2*nObar*ne0 + (Kiz3 + Kiz4)*nO2*ne0...
- Krec3*nOplus*nOminus*vol_rec/volume - Kch*nOplusbar*nO2...
- Kion*nOplus;
% for nOminus
vdot(4)=(Katt+Kiz3)*nO2*ne0 + Kattm*nO2mbar*ne0...
- ((Krec+Krec2)*nO2plus*nOminus+Krec3*nOplus*nOminus)...
*vol_rec/volume - Kdet*nOminusbar*nObar - Krec4*nOminusbar*nO2mbar;
% for nO
vdot(5)=2*Kei*ne0*nO2plusbar + (2*Kdiss+Katt+Kiz4)*ne0*nO2...
+ (Krec+3*Krec2)*nO2plus*nOminus*vol_rec/volume...
+ 2*Krec3*nOplus*nOminus*vol_rec/volume + Kch*nOplusbar*nO2...
+ (Kattm+2*Kdism)*nO2mbar*ne0 + Krec4*nOminusbar*nO2mbar...
+ Kion*nOplus - Kiz2*nObar*ne0 - Kdet*nOminusbar*nObar...
- KO*nO - Kpump*nObar;
% for nO2m
vdot(6)=Kex*nO2*ne0 - (Kizm+Kattm+Kdeex+Kdism)*nO2mbar*ne0...
- Krec4*nO2mbar*nOminusbar - KO2m*nO2m - Kpump*nO2mbar;

```

```

% for power balance
vdot(7)=pabs - Ec_O2*Kiz1*nO2*ne0 - Ec_O*Kiz2*nObar*ne0...
- Eei_O*Kion*nOplus - Eei_O2*Kion*nO2plus;

```

File name: alpha0find.m

```

%%%%%%%%%%%%%%%%%%%%%%%%%%%%%%%%%%%%%%%%%%%%%%%%%%%%%%%%%%%%%%%%%%%%%%%%
% Calculations to find alpha0 for given alpha_bar
% Last modification 11-30-2005
% by Sungjin Kim
% Department of Electrical Engineering and Computer Sciences
% University of California, Berkeley
%%%%%%%%%%%%%%%%%%%%%%%%%%%%%%%%%%%%%%%%%%%%%%%%%%%%%%%%%%%%%%%%%%%%%%%%
function G=alpha0find(alpha)
global volume alphabar;
alpha_bar=alphabar;
volm=volume;
G=alpha.*vol_minus(alpha) - alpha_bar*volm;

```

File name: vol_minus.m

```

%%%%%%%%%%%%%%%%%%%%%%%%%%%%%%%%%%%%%%%%%%%%%%%%%%%%%%%%%%%%%%%%%%%%%%%%
% Subroutine for alpha0find
% Calculations to find vol_minus
% Last modification 11-30-2005
% by Sungjin Kim
% Department of Electrical Engineering and Computer Sciences
% University of California, Berkeley
%%%%%%%%%%%%%%%%%%%%%%%%%%%%%%%%%%%%%%%%%%%%%%%%%%%%%%%%%%%%%%%%%%%%%%%%
function vmin=vol_minus(alpha)
vmin=4*pi/3.*(rminus(alpha).^2 - rminus(alpha).*lminus(alpha)*2/3...
+ (lminus(alpha).^2)/6).*lminus(alpha);

```

File name: rminus.m

```

%%%%%%%%%%%%%%%%%%%%%%%%%%%%%%%%%%%%%%%%%%%%%%%%%%%%%%%%%%%%%%%%%%%%%%%%
% Subroutine for alpha0find
% Calculations to find r_minus
% Last modification 11-30-2005
% by Sungjin Kim
% Department of Electrical Engineering and Computer Sciences
% University of California, Berkeley
%%%%%%%%%%%%%%%%%%%%%%%%%%%%%%%%%%%%%%%%%%%%%%%%%%%%%%%%%%%%%%%%%%%%%%%%
function rmin=rminus(alpha)
global l_p R
rmin=R - l_p + lminus(alpha);

```

File name: lminus.m

```

%%%%%%%%%%%%%%%%%%%%%%%%%%%%%%%%%%%%%%%%%%%%%%%%%%%%%%%%%%%%%%%%%%%%%%%%
% Subroutine for alpha0find

```

```

% Calculations to find l_minus
% Last modification 11-30-2005
% by Sungjin Kim
% Department of Electrical Engineering and Computer Sciences
% University of California, Berkeley
%%%%%%%%%%%%%%%%%%%%%%%%%%%%%%%%%%%%%%%%%%%%%%%%%%%%%%%%%%%%%%%%%%%%%%%%
function lmin=lminus(alpha)
global l_p Rlambda Rrec
Rlam=Rlambda;
Rrc=Rrec;
beta1=max((heff(alpha)-alpha*Rlam)/Rrc./Ffn(alpha), 0);
beta2=max(1-sqrt(alpha*Rlam./heff(alpha)), 0);
lmin=l_p*(1-(beta1.^(-3) + beta2.^(-3)).^(-1/3));

```

File name: heff.m

```

%%%%%%%%%%%%%%%%%%%%%%%%%%%%%%%%%%%%%%%%%%%%%%%%%%%%%%%%%%%%%%%%%%%%%%%%
% Subroutine for alpha0find
% Calculations to find h_effective
% Last modification 11-30-2005
% by Sungjin Kim
% Department of Electrical Engineering and Computer Sciences
% University of California, Berkeley
%%%%%%%%%%%%%%%%%%%%%%%%%%%%%%%%%%%%%%%%%%%%%%%%%%%%%%%%%%%%%%%%%%%%%%%%
function heffective=heff(alpha)
global Rlambda h10
h_10=h10;
Rlam=Rlambda;
heffective=h_10 + (1 - h_10)*alpha*Rlam;

```

File name: Ffn.m

```

%%%%%%%%%%%%%%%%%%%%%%%%%%%%%%%%%%%%%%%%%%%%%%%%%%%%%%%%%%%%%%%%%%%%%%%%
% Subroutine for alpha0find
% Calculations for Ffunc
% Last modification 11-30-2005
% by Sungjin Kim
% Department of Electrical Engineering and Computer Sciences
% University of California, Berkeley
%%%%%%%%%%%%%%%%%%%%%%%%%%%%%%%%%%%%%%%%%%%%%%%%%%%%%%%%%%%%%%%%%%%%%%%%
function Ffunc=Ffn(alpha)
Ffunc=(alpha.^2)*8/15 + alpha*2/3;

```

File name: o_ec.m

```

%%%%%%%%%%%%%%%%%%%%%%%%%%%%%%%%%%%%%%%%%%%%%%%%%%%%%%%%%%%%%%%%%%%%%%%%
% Calculations of Ec for Oxygen Neutral
% Last modification 11-30-2005
% by Sungjin Kim
% Department of Electrical Engineering and Computer Sciences
% University of California, Berkeley
%%%%%%%%%%%%%%%%%%%%%%%%%%%%%%%%%%%%%%%%%%%%%%%%%%%%%%%%%%%%%%%%%%%%%%%%
function oEc=o_ec(Te);

```

```

global me MO Energy0 sig0
Tel=Te;
Energy=Energy0;
sig=sig0;
Kel=rateconstant( Energy, sig, Tel );
kiz = 9e-15 * (Tel^0.7) * exp(-13.6/Tel);
k1D = 4.54e-15 * exp(-2.36/Tel);
k1S = 7.86e-16 * exp(-4.489/Tel);
k3P0 = 2.53e-15 * exp(-17.34/Tel);
k5S0 = 9.67e-16 * exp(-9.97/Tel);
k3S0 = 3.89e-15 * exp(-9.75/Tel);
kh = 4.31e-14 * exp(-18.59/Tel);
oEc = 13.61 + k1D/kiz*1.96 + k1S/kiz*4.18 + k5S0/kiz*9.14...
      + k3S0/kiz*9.51 + k3P0/kiz*15.65 + kh/kiz*12 + Kel/kiz*3*me/MO*Tel;

```

File name: o2_ec.m

```

%%%%%%%%%%%%%%%%%%%%%%%%%%%%%%%%%%%%%%%%%%%%%%%%%%%%%%%%%%%%%%%%%%%%%%%%
% Calculations of Ec for O2
% Last modification 11-30-2005
% by Sungjin Kim
% Department of Electrical Engineering and Computer Sciences
% University of California, Berkeley
%%%%%%%%%%%%%%%%%%%%%%%%%%%%%%%%%%%%%%%%%%%%%%%%%%%%%%%%%%%%%%%%%%%%%%%%
function o2Ec=o2_ec(Te);
global me MO2 Energy02 sig02
Tel=Te;
Energy=Energy02;
sig=sig02;
Kel=rateconstant( Energy, sig, Tel );
kiz = 2.34e-15*(Tel^1.03)*exp(-12.29/Tel);
krot = 1.8736e-17 * exp(-2.9055/Tel);
kv1 = 2.8e-15 * exp(-3.72/Tel);
kv2 = 1.28e-15 * exp(-3.67/Tel);
ka1D = 1.37e-15 * exp(-2.14/Tel);
kb1S = 3.24e-16 * exp(-2.218/Tel);
kex1 = 1.13e-15 * exp(-3.94/Tel);
k1dis = 6.86e-15 * exp(-6.29/Tel);
k2dis = 3.4879e-14 * exp(-5.92/Tel);
k3dis = 1.443e-16 * exp(-17.25/Tel);
kex2 = 1.13e-15 * exp(-18.35/Tel);
o2Ec = 12.14 + krot/kiz*0.02 + kv1/kiz*0.19 + kv2/kiz*0.38...
      + ka1D/kiz*0.977 + kb1S/kiz*1.627 + kex1/kiz*4.5...
      + k1dis/kiz*6 + k2dis/kiz*8.4 + k3dis/kiz*9.97...
      + kex2/kiz*14.7 + Kel/kiz*3*me/MO2*Tel;

```

File name: rateconstant.m

```

%%%%%%%%%%%%%%%%%%%%%%%%%%%%%%%%%%%%%%%%%%%%%%%%%%%%%%%%%%%%%%%%%%%%%%%%
% Subroutine for Calculations of rate constants
% Last modification 11-30-2005
% by Sungjin Kim
% Department of Electrical Engineering and Computer Sciences
% University of California, Berkeley

```

```

%%%%%%%%%%%%%%%%%%%%%%%%%%%%%%%%%%%%%%%%%%%%%%%%%%%%%%%%%%%%%%%%%%%%%%%%
function K=rateconstant( Energy, sig, Tel );
global ee me
nefnul1 = (2 * ee .* Energy /me).^(1/2) .* sig;
q0 = Energy.^0.5.*2/sqrt(pi).*(1/Tel)^(3/2).*exp(-Energy/Tel).*nefnul1;
qq=0;qqq=0;
for ii=1:1:max(size(Energy))-1
    qq = (q0(ii) + q0(ii+1)) .* (Energy(ii+1) - Energy(ii))/2;
    qqq = qq + qqq;
end
K = qqq;

```

File name: Ocross.txt (A text data file for Oxygen atom cross section calculation)

0.136	1.82	1.82
0.544	3.04	3.04
1.224	4.7	4.7
1.28	5	5
1.66	6	6
2.63	7	7
4	7.17	7.5
5	7.45	8
6.25	7.5	8.03
8	7.45	8
10	7.2	7.6
20	6	7.36
30	5	7
50	4	6.4
60	3.4	6.3
100	2.4	6.2

File name: O2cross.txt (A text data file for O2 cross section calculation)

1	0.0000	0.3500
2	0.0010	0.3500
3	0.0020	0.3600
4	0.0030	0.4000
5	0.0050	0.5000
6	0.0070	0.5800
7	0.0085	0.6400
8	0.0100	0.7000
9	0.0150	0.8700
10	0.0200	0.9900
11	0.0300	1.2400
12	0.0400	1.4400
13	0.0500	1.6000
14	0.0700	2.1000
15	0.1000	2.5000
16	0.1200	2.8000
17	0.1500	3.1000
18	0.1700	3.3000
19	0.2000	3.6000
20	0.2500	4.1000
21	0.3000	4.5000
22	0.3500	4.7000
23	0.4000	5.2000

24	0.5000	5.7000
25	0.7000	6.1000
26	1.0000	7.2000
27	1.2000	7.9000
28	1.3000	7.9000
29	1.5000	7.6000
30	1.7000	7.3000
31	1.9000	6.9000
32	2.1000	6.6000
33	2.2000	6.5000
34	2.5000	6.1000
35	2.8000	5.8000
36	3.0000	5.7000
37	3.3000	5.5000
38	3.6000	5.4500
39	4.0000	5.5000
40	4.5000	5.5500
41	5.0000	5.6000
42	6.0000	6.0000
43	7.0000	6.6000
44	8.0000	7.1000
45	10.0000	8.0000
46	12.0000	8.5000
47	15.0000	8.8000
48	17.0000	8.7000
49	20.0000	8.6000
50	25.0000	8.2000
51	30.0000	8.0000
52	50.0000	7.7000
53	75.0000	6.8000
54	100.0000	6.5000
55	150.0000	6.7000
56	200.0000	6.0000
57	300.0000	4.9000
58	500.0000	3.6000
59	700.0000	2.9000
60	1000.0000	2.1200
61	1500.0000	1.4800
62	2000.0000	1.1400
63	3000.0000	0.7900
64	5000.0000	0.5100
65	7000.0000	0.3800
66	10000.0000	0.2800

File name: New_OxygenODE_p.m

```

%%%%%%%%%%%%%%%%%%%%%%%%%%%%%%%%%%%%%%%%%%%%%%%%%%%%%%%%%%%%%%%%%%%%%%%%
% Integrate ODE's for global oxygen with new h_l factors
% Using the differential equations with average densities
% assumption of parabolic profiles for neutrals
% including O2, O2+, O+, O-, O & O2*
% Reaction coefficients have been corrected.
% Code to simulate pulsed-power discharges
% Last modification 11-30-2005

```

```

% by Sungjin Kim
% Department of Electrical Engineering and Computer Sciences
% University of California, Berkeley
%%%%%%%%%%%%%%%%%%%%%%%%%%%%%%%%%%%%%%%%%%%%%%%%%%%%%%%%%%%%%%%%%%%%%%%%
clear all
global ee me MO MO2 ng Tg Ti l_p gamma0 gamma02m Efactor_O2
global Efactor_O EnergyO2 sigO2 EnergyO sigO
global Krec Krec2 Krec3 Krec4 Kdet Kch Rlambda hl0 Rrec alphabar
global Pw_peak f dutyratio risetime R area volume
global QtorrLit Qmolec Kpump scat_Xsec
ee=1.6022E-19;
me=9.1095E-31;           % mass of electron
MO=1836*16*me;          % mass of an Oxygen atom
MO2=2*MO;                % mass of an Oxygen Molecule
Tg=0.052;                % 600K in volts
Ti=Tg;
gamma0=0.5                % wall recombination rate of Oxygen neutrals
gamma02m=0.007           % wall recombination rate of meta-stable Oxygen
R=0.15                    % reactor radius
L=0.30                    % reactor length
l_p=L/2;                  % half length
area=2*pi*R*(R+L);        % total surface area
volume=pi*R^2*L;          % reactor volume
Efactor_O=2+0.5*(1+log(MO/(2*pi*me))); % (E_e+E_i_O)/Te
Efactor_O2=2+0.5*(1+log(MO2/(2*pi*me))); % (E_e+E_i_O2)/Te
% Loading all cross-section data to calculate Kel & Ec
load o2cross.txt -ASCII;
EnergyO2 = o2cross(:,2);
sigmaO2 = o2cross(:,3);
sigO2 = sigmaO2 * 1e-20;
load Ocross.txt -ASCII;
EnergyO = Ocross(:,1);
sigma0 = Ocross(:,2);
sig0 = sigma0 * 1e-20;
%
p0=10;                    % starting pressures in mTorr
Qsccm=50;                  % O2 flow rate in sccm
QtorrLit=Qsccm/79.05;     % sccm to Torr-Liter/sec
Qmolec=4.483e17*Qsccm;    % sccm to molecules/sec
Kpump=QtorrLit/(p0*volume); % Pumping Rate coefficient
ng0=3.3E19*p0*0.026/Tg;  % m^-3
ng0_cm=ng0*1e-6          % cm^-3
% elastic scattering cross-section for Oxygen in m^2
scat_Xsec=7.5e-19;
% heavy particle reaction rates
Krec=2.6E-14*sqrt(0.026/Tg);
Krec2=2.6E-14*sqrt(0.026/Tg);
Krec3=4.0E-14*sqrt(0.026/Tg);
Krec4=3.3E-17;
Kdet=1.6E-16;
Kch=2.0E-17*sqrt(0.026/Tg);
%
Tpvec=[3e-4]              % pulse period in sec
tavg_results=zeros(30,length(Tpvec)); % number of items to save=30
%
for ii=1:length(Tpvec)
T_p=Tpvec(ii);           % pulse period in sec

```

```

f=1/T_p; % pulse frequency
risetime=0.45*T_p/1e-6; % rise time in micro-sec (50% of period)
% duty ratio ( for CW, =1; for 50%, =0.5 ; for 25%, =0.05 )
dutyratio=0.05;
Pw_peak=1600; % watts
%
t0=0;
tf=0.02;
nO2plusbar0=2E16
nOplusbar0=6.4E14
nOminusbar0=8.4E15
nObar0=2E18
nO2mbar0=1.5e19
nO20=ng0-nObar0-nO2mbar0
Te0=3.3
pe0=1.5*(nO2plusbar0+nOplusbar0-nOminusbar0)*Te0
v0=[nO20 nO2plusbar0 nOplusbar0 nOminusbar0 nObar0 nO2mbar0 pe0];
%options=odeset('MaxStep', T_p*0.01*2)
[t v]=ode23s('new_oxys_p', [t0 tf], v0);%, options);
nO2=v(:,1);
nO2plusbar=v(:,2);
nOplusbar=v(:,3);
nOminusbar=v(:,4);
ne0=nO2plusbar+nOplusbar-nOminusbar;
nObar=v(:,5);
nO2mbar=v(:,6);
Te=v(:,7)./(1.5.*ne0);
%
% take data of last 10 periods
%
last_10=find(t >(tf-10*1/f));
last10=last_10(1);
t_final=t(last10:end);
nO2_final=nO2(last10:end);
nO2plus_final=nO2plusbar(last10:end);
nOplus_final=nOplusbar(last10:end);
nOminus_final=nOminusbar(last10:end);
ne_final=ne0(last10:end);
nO_final=nObar(last10:end);
nO2m_final=nO2mbar(last10:end);
Te_final=Te(last10:end);
pw_final=pulse(t_final);
final_data=[t_final nO2_final nO2plus_final nOplus_final...
            nOminus_final ne_final nO_final nO2m_final Te_final];
% save results to a file
filename=[num2str(T_p*1e6), 'uSec.txt']
save(filename, 'final_data', '-ASCII', '-double');
%
% calculate time averaged values of last 10 periods
%
tavg_nO2=time_avg(t_final, nO2_final);
n_O2=tavg_nO2*1e-6; % in cm^-3
tavg_power=time_avg(t_final, pw_final);
tavg_nO2plus=time_avg(t_final, nO2plus_final);
n_O2plus_bar=tavg_nO2plus*1e-6; % in cm^-3
tavg_nOplus=time_avg(t_final, nOplus_final);
n_Oplus_bar=tavg_nOplus*1e-6; % in cm^-3

```

```

tavg_nOminus=time_avg(t_final,nOminus_final);
n_Ominus_bar=tavg_nOminus*1e-6;      % in cm^-3
tavg_ne=time_avg(t_final,ne_final);
n_e0=tavg_ne*1e-6;      % in cm^-3
tavg_nO=time_avg(t_final,nO_final);
n_O_bar=tavg_nO*1e-6;      % in cm^-3
tavg_nO2m=time_avg(t_final,nO2m_final);
n_O2m_bar=tavg_nO2m*1e-6;      % in cm^-3
tavg_Te=time_avg(t_final,Te_final);
tavg_ng=tavg_nO2+tavg_nO+tavg_nO2m;
n_g=tavg_ng*1e-6;      % in cm^-3
tavg_p=tavg_ng/3.3e19*(Tg/0.026); % final pressure in mTorr
% ratio for density weighting
nOp_ratio=tavg_nOplus/(tavg_nO2plus+tavg_nOplus);
%
% plotting the results
%
figure(ii)
subplot(8,1,1)
plot(t_final,nO2plus_final,t_final, ne_final,'--')
ylabel('n_{O_2}^{+}, n_{e0} (m^{-3})')
axis([t_final(1) inf 0 tavg_nO2plus*1.5])
title(['Flowrate=',num2str(Qscm),'sccm, P_{peak}=',...
      num2str(Pw_peak),'W, p_0=',num2str(p0),'mTorr,...
      p_f=',num2str(round(tavg_p)),'mTorr'])
subplot(8,1,2)
plot(t_final,nOplus_final)
ylabel('n_{O^{+}} (m^{-3})')
axis([t_final(1) inf 0 tavg_nOplus*1.5])
subplot(8,1,3)
plot(t_final,nOminus_final)
ylabel('n_{O^{-}} (m^{-3})')
axis([t_final(1) inf 0 tavg_nOminus*1.5])
subplot(8,1,4)
plot(t_final,nO_final)
ylabel('n_O (m^{-3})')
axis([t_final(1) inf 0 tavg_nO*1.5])
subplot(8,1,5)
plot(t_final,nO2m_final)
ylabel('n_{O_2}^{*} (m^{-3})')
axis([t_final(1) inf 0 tavg_nO2m*1.5])
subplot(8,1,6)
plot(t_final,nO2_final)
ylabel('n_{O_2} (m^{-3})')
axis([t_final(1) inf 0 tavg_nO2*1.5])
subplot(8,1,7)
plot(t_final,Te_final)
xlabel('t (sec)')
ylabel('T_e (Volt)')
axis([t_final(1) inf 0 6])
subplot(8,1,8)
plot(t_final,pw_final)
xlabel('t (sec)')
ylabel('Power (W)')
axis([t_final(1) inf 0 1000])
%
% caculating values for O neutral & O2m

```

```

%
lambda=1/(tavg_ng*scat_Xsec); % lambda in m
vbar0=sqrt(8*ee*Ti/(pi*MO)); % average thermal velocity of O neutral
vbarO2m=sqrt(8*ee*Ti/(pi*MO2)); % average thermal velocity of O2m
DO=ee*Tg*lambda/vbar0/MO; % Diffusion coefficient of O neutral
DO2m=ee*Tg*lambda/vbarO2m/MO2; % Diffusion coefficient of O2m
d0=sqrt(4*DO*1_p*(2-gamma0)/vbar0/gamma0 + 1_p^2);
dO2m=sqrt(4*DO2m*1_p*(2-gammaO2m)/vbarO2m/gammaO2m + 1_p^2);
hAO=1/(1 + 1_p*vbar0*gamma0/4/DO/(2-gamma0));
hAO2m=1/(1 + 1_p*vbarO2m*gammaO2m/4/DO2m/(2-gammaO2m));
vol_0=volume*(1 - 1_p^2/(3*d0^2))*(1 - (2/3)*1_p^3/(R*d0^2)...
+ 1_p^4/(6*R^2*d0^2));
vol_O2m=volume*(1 - 1_p^2/(3*dO2m^2))*(1 - (2/3)*1_p^3/(R*dO2m^2)...
+ 1_p^4/(6*R^2*dO2m^2));
% calculation of the final alpha0
Tplusf=Ti;
Tminusf=Ti;
gamma_plusf=tavg_Te/Tplusf;
gamma_minusf=tavg_Te/Tminusf;
etaf=2*Tplusf/(Tplusf+Tminusf);
hl0=0.86/sqrt(3+etaf*1_p/lambda);
Rlambda=sqrt(2*pi/gamma_plusf)*lambda/1_p/etaf;
tavg_uB_O2=sqrt(ee*tavg_Te/MO2);
tavg_uB_0=sqrt(ee*tavg_Te/MO);
% density-weighted Bohm velocity in m/s
tavg_uB_dw=tavg_uB_O2*(1-nOp_ratio)+tavg_uB_0*nOp_ratio;
% density-weighted Recombination rate coefficient
Krec_dw_f=(Krec+Krec2)*(1-nOp_ratio)+Krec3*nOp_ratio;
Krec=Krec_dw_f*tavg_ne*1_p/tavg_uB_dw;
alphabar=tavg_nOminus/tavg_ne; % t_avg alpha_bar
alpha0=fzero('alpha0find',[1e-3 1e3]); % t_avg alpha0
volumeminus=vol_minus(alpha0);
tavg_nOminus0=tavg_nOminus*volume/volumeminus;
tavg_nplus0=tavg_nOminus0 + tavg_ne;
tavg_nOplus0=tavg_nplus0*nOp_ratio;
tavg_nO2plus0=tavg_nplus0-tavg_nOplus0;
tavg_nO0=tavg_nO*volume/vol_0;
tavg_nO2m0=tavg_nO2m*volume/vol_O2m;
n_O2plus0=tavg_nO2plus0*1e-6; % in cm^-3
n_Oplus0=tavg_nOplus0*1e-6; % in cm^-3
n_Ominus0=tavg_nOminus0*1e-6; % in cm^-3
n_O0=tavg_nO0*1e-6; % in cm^-3
n_O2m0=tavg_nO2m0*1e-6; % in cm^-3
% calculation of final hl factor
% density weighted positive ion mass
Mplus_dw=MO2*(1-nOp_ratio)+MO*nOp_ratio;
nstarf=15/56*sqrt(8*ee*Tplusf/pi/Mplus_dw)*(etaf^2)/(Krec_dw_f*lambda);
hpar2f=hl0*1/(1+alpha0);
hpar1f=1/(gamma_minusf^0.5 +
(gamma_plusf^0.5)*(etaf*1_p/sqrt(2*pi)/lambda))*(alpha0/(1+alpha0));
hflat1f=1/(gamma_minusf^0.5 + (gamma_plusf^0.5)*(nstarf^0.5)...
/(tavg_nOminus0^0.5));
%overall hl factor by "linear ansatz"
final_hl=hpar2f + hpar1f + hflat1f
% size of EN core (lminus & rminus)
%final_lminus=lminus(alpha0); %in m
%Lminus=final_lminus*1e2 % in cm

```

```

%final_rminus=R - l_p + final_lminus; %in m
%Rminus=final_rminus*1e2 % in cm
%lminus_over_l_p=final_lminus/l_p
%vratio=volumeminus/volume;
% ion flux
dissociation_rate = tavg_n0/tavg_ng;
tavg_nplus_flux=final_hl*tavg_nplus0*tavg_uB_dw*1e-4 % in /cm^2/s
tavg_n0_flux=hA0*tavg_n00*vbar0/4*1e-4 % in /cm^2/s
flux_ratio=tavg_n0_flux/tavg_nplus_flux
lambda_cm=lambda/1e-2; % in cm
% save results
tavg_results(:,ii)=[p0;tavg_p;Pw_peak;dutyratio;tavg_power;T_p;...
    ng0_cm;n_g;n_O2plus0;n_Oplus0;n_Ominus0;n_e0;n_O0;n_O2m0;...
    n_O2plus_bar;n_Oplus_bar;n_Ominus_bar;n_O_bar; n_O2m_bar;...
    n_O2;tavg_Te;alpha0;alphabar;gamma_plusf;final_hl;lambda_cm;...
    dissociation_rate;tavg_nplus_flux;tavg_n0_flux;flux_ratio];
end
% save results to a file
filename2=[num2str(Pw_peak),'W_AR1.txt']
save(filename2,'tavg_results','-ASCII','-double');

```

File name: new_oxys_p.m

```

%%%%%%%%%%%%%%%%%%%%%%%%%%%%%%%%%%%%%%%%%%%%%%%%%%%%%%%%%%%%%%%%%%%%%%%%
% Differential equations with average densities
% Integrate ODE's for global oxygen with new h_l factors
% Using the differential equations with average densities
% assumption of parabolic profiles for neutrals
% including O2, O2+, O+, O-, O & O2*
% Reaction coefficients have been corrected.
% Code to simulate pulsed-power discharges
% Last modification 11-30-2005
% by Sungjin Kim
% Department of Electrical Engineering and Computer Sciences
% University of California, Berkeley
%%%%%%%%%%%%%%%%%%%%%%%%%%%%%%%%%%%%%%%%%%%%%%%%%%%%%%%%%%%%%%%%%%%%%%%%
function vdot=new_oxys_p(t,v)
global ee me MO MO2 ng Tg Ti l_p gamma0 gamma02m
global Efactor_O2 Efactor_O EnergyO2 sigO2 EnergyO sigO
global Krec Krec2 Krec3 Krec4 Kdet Kch Rlambda hl0 Rrec alphabar
global Pw_peak f dutyratio risetime R area volume
global QtorrLit Qmolec Kpump scat_Xsec
vdot=zeros(7,1);
nO2=v(1);
nO2plusbar=v(2)
nOplusbar=v(3)
nOminusbar=v(4)
nObar=v(5);
nO2mbar=v(6);
pe=v(7)
ng=nO2+nObar+nO2mbar;
ne0=nO2plusbar+nOplusbar-nOminusbar
Te=pe/(1.5*ne0)
Tplus=Ti;
Tminus=Ti;

```

```

gamma_plus=Te/Tplus;
gamma_minus=Te/Tminus;
% ratio for density weighting
nOplus_ratio=nOplusbar/(nO2plusbar+nOplusbar);
% calculating lambda
lambda=1/(ng*scat_Xsec); % lambda in m
% caculating values for O neutral & O2m
vbarO=sqrt(8*ee*Ti/(pi*MO)); % average thermal velocity of O neutral
vbarO2m=sqrt(8*ee*Ti/(pi*MO2)); % average thermal velocity of O2m
DO=ee*Tg*lambda/vbarO/MO; % Diffusion coefficient of O neutral
DO2m=ee*Tg*lambda/vbarO2m/MO2; % Diffusion coefficient of O2m
dO=sqrt(4*DO*1_p*(2-gammaO)/vbarO/gammaO + 1_p^2);
dO2m=sqrt(4*DO2m*1_p*(2-gammaO2m)/vbarO2m/gammaO2m + 1_p^2);
hAO=1/(1 + 1_p*vbarO*gammaO/4/DO/(2-gammaO));
hAO2m=1/(1 + 1_p*vbarO2m*gammaO2m/4/DO2m/(2-gammaO2m));
% wall recombination loss rate for O neutral
KO=hAO*vbarO*2*gammaO/(2-gammaO)*area/volume/4;
% wall recombination loss rate for O2m
KO2m=hAO2m*vbarO2m*2*gammaO2m/(2-gammaO2m)*area/volume/4;
vol_O=volume*(1 - 1_p^2/(3*dO^2))*(1 - (2/3)*1_p^3/(R*dO^2)...
+ 1_p^4/(6*R^2*dO^2));
vol_O2m=volume*(1 - 1_p^2/(3*dO2m^2))*(1 - (2/3)*1_p^3/(R*dO2m^2)...
+ 1_p^4/(6*R^2*dO2m^2));
%finding alpha0
eta=2*Tplus/(Tplus+Tminus);
hl0=0.86/sqrt(3+eta*1_p/lambda);
Rlambda=sqrt(2*pi/gamma_plus)*lambda/1_p/eta;
uB_O2=sqrt(ee*Te/MO2);
uB_O=sqrt(ee*Te/MO);
% density-weighted Bohm velocity
uB_dw=uB_O2*(1-nOplus_ratio)+uB_O*nOplus_ratio;
% density-weighted Recombination rate coefficient
Krec_dw=(Krec+Krec2)*(1-nOplus_ratio)+Krec3*nOplus_ratio;
Rrec=Krec_dw*ne0*1_p/uB_dw;
alphabar=nOminusbar/ne0
alpha0=fzero('alpha0find',[1e-3 1e5]);
volminus=vol_minus(alpha0);
%calculating peak(center) densities
nOminus=nOminusbar*volume/volminus;
nplus=nOminus+ne0;
nOplus=nplus*nOplus_ratio;
nO2plus=nplus-nOplus;
nO=nObar*volume/vol_O;
nO2m=nO2mbar*volume/vol_O2m;
% calculation of hl factors with 3 models
% density weighted positive ion mass
Mplus_dw=MO2*(1-nOplus_ratio)+MO*nOplus_ratio;
nstar=15/56*sqrt(8*ee*Tplus/pi/Mplus_dw)*(eta^2)/(Krec_dw*lambda);
hpar2=hl0*1/(1+alpha0);
hpar1=1/(gamma_minus^0.5 + (gamma_plus^0.5)...
*(eta*1_p/sqrt(2*pi)/lambda))*(alpha0/(1+alpha0));
hflat1=1/(gamma_minus^0.5 + (gamma_plus^0.5)...
*(nstar^0.5)/(nOminus^0.5));
hl=hpar2 + hpar1 + hflat1; % overall hl factor by "linear ansatz"
% size of EN core (lminus & rminus)
l_minus=lminus(alpha0);
r_minus=R - 1_p + l_minus;

```

```

% Effective volume for recombination losses
vol_rec=(2*pi*l_minus/(1+alpha0))*(8/15*alpha0*(r_minus^2...
    - 14/15*r_minus*l_minus + 4/15*l_minus^2) + 2/3*(r_minus^2...
    - 2/3*r_minus*l_minus + 1/6*l_minus^2));
% Surface loss of electron-ion pair
Kion=hl*uB_dw*area/volume;
% other reaction coefficients
Kiz1=2.34E-15*Te^(1.03)*exp(-12.29/Te);
Kei=2.2E-14*Te^(-0.5);
Katt=1.07E-15*Te^(-1.391)*exp(-6.26/Te);
Kiz2=9E-15*Te^(0.7)*exp(-13.6/Te);
Kdiss=6.86E-15*exp(-6.29/Te);
Kiz3=7.1E-17*Te^0.5*exp(-17/Te);
Kiz4=1.88E-16*Te^(1.699)*exp(-16.81/Te);
Kex=1.37E-15*exp(-2.14/Te);
Kizm=2.34E-15*Te^(1.03)*exp(-11.31/Te);
Kattm=4.19E-15*Te^(-1.376)*exp(-5.19/Te);
Kdeex=2.06E-15*exp(-1.163/Te);
Kdism=6.86E-15*exp(-5.31/Te);
% calculating Ec
Ec_O=o_ec(Te);
Ec_O2=o2_ec(Te);
Eei_O=Efactor_O*Te;
Eei_O2=Efactor_O2*Te;
% absorbed Power
pabs=pulse(t)/(ee*volume)
% differential EQ's
% for nO2
vdot(1)=Qmolec/volume + Krec*nO2plus*nOminus*vol_rec/volume...
    + Kdet*nOminusbar*nObar + Kdeex*nO2mbar*ne0...
    + Krec4*nO2mbar*nOminusbar + Kion*nO2plus + KO2m*nO2m...
    + 0.5*KO*nO - (Kiz1 + Katt + Kdiss + Kiz3 + Kiz4 + Kex)*nO2*ne0...
    - Kch*nOplusbar*nO2 - Kpump*nO2;
% for nO2plus
vdot(2)=Kiz1*nO2*ne0 + Kizm*nO2mbar*ne0 + Kch*nOplusbar*nO2...
    - (Krec + Krec2)*nO2plus*nOminus*vol_rec/volume...
    - Kei*ne0*nO2plusbar - Kion*nO2plus;
% for nOplus
vdot(3)=Kiz2*nObar*ne0 + (Kiz3 + Kiz4)*nO2*ne0...
    - Krec3*nOplus*nOminus*vol_rec/volume - Kch*nOplusbar*nO2...
    - Kion*nOplus;
% for nOminus
vdot(4)=(Katt+Kiz3)*nO2*ne0 + Kattm*nO2mbar*ne0...
    - ((Krec+Krec2)*nO2plus*nOminus+Krec3*nOplus*nOminus)...
    *vol_rec/volume - Kdet*nOminusbar*nObar...
    - Krec4*nOminusbar*nO2mbar;
% for nO
vdot(5)=2*Kei*ne0*nO2plusbar + (2*Kdiss+Katt+Kiz4)*ne0*nO2...
    + (Krec+3*Krec2)*nO2plus*nOminus*vol_rec/volume...
    + 2*Krec3*nOplus*nOminus*vol_rec/volume + Kch*nOplusbar*nO2...
    + (Kattm+2*Kdism)*nO2mbar*ne0 + Krec4*nOminusbar*nO2mbar...
    + Kion*nOplus - Kiz2*nObar*ne0 - Kdet*nOminusbar*nObar...
    - KO*nO - Kpump*nObar;
% for nO2m
vdot(6)=Kex*nO2*ne0 - (Kizm+Kattm+Kdeex+Kdism)*nO2mbar*ne0...
    - Krec4*nO2mbar*nOminusbar - KO2m*nO2m - Kpump*nO2mbar;
% for power balance

```

```

vdot(7)=pabs - Ec_O2*Kiz1*nO2*ne0 - Ec_O*Kiz2*nObar*ne0...
- Eei_O*Kion*nOplus - Eei_O2*Kion*nO2plus;

```

File name: time_avg.m

```

%%%%%%%%%%%%%%%%%%%%%%%%%%%%%%%%%%%%%%%%%%%%%%%%%%%%%%%%%%%%%%%%%%%%%%%%
% Subroutine for Calculations of time-averages
% Last modification 11-30-2005
% by Sungjin Kim
% Department of Electrical Engineering and Computer Sciences
% University of California, Berkeley
%%%%%%%%%%%%%%%%%%%%%%%%%%%%%%%%%%%%%%%%%%%%%%%%%%%%%%%%%%%%%%%%%%%%%%%%
function result=time_avg(ts,var)
x_f=size(ts,1);
var_sum=0;
for x=2:x_f
    var_sum = var_sum + var(x)*(ts(x)-ts(x-1));
end
result=var_sum / (ts(x_f)-ts(1));

```

File name: pulse.m

```

%%%%%%%%%%%%%%%%%%%%%%%%%%%%%%%%%%%%%%%%%%%%%%%%%%%%%%%%%%%%%%%%%%%%%%%%
% Function for pulse shape generations
% Last modification 11-30-2005
% by Sungjin Kim
% Department of Electrical Engineering and Computer Sciences
% University of California, Berkeley
%%%%%%%%%%%%%%%%%%%%%%%%%%%%%%%%%%%%%%%%%%%%%%%%%%%%%%%%%%%%%%%%%%%%%%%%
function pw=pulse(t)
global Pw_peak f risetime dutyratio
F=f; % pulse frequency
rt=risetime; % rise time in micro-sec
dr=dutyratio; % duty ratio (on-time/pulse period; for CW, dr=1)
W_0=2*pi*F;
P0=Pw_peak;
DR=2*dr-1; % DR=(on-time - off-time)/(on-time+off-time)
RT=1/(F*rt*1E-6);
offset=asin(-DR)/(2*pi*F);
pw=P0.*(tanh(RT.*(sin(W_0.*(t+offset))+DR))...
+tanh(RT.*(1-DR)))./(tanh(RT.*(1+DR))+tanh(RT.*(1-DR)));

```

Bibliography

- [1] V. A. Godyak, *Soviet radio frequency discharge research* (Delphic Associates, Falls Church, VA, 1986)
- [2] M. A. Lieberman and A. J. Lichtenberg, *Principles of Plasma Discharges and Materials Processing*, 2nd ed. (Wiley-Interscience, Hoboken, N.J., 2005)
- [3] C. Lee, D. B. Graves, M. A. Lieberman, and D. W. Hess, *J. Electrochem. Soc.* **141**, 1546 (1994)
- [4] C. Lee and M. A. Lieberman, *J. Vac. Sci. Technol. A* **13**, 368 (1995)
- [5] E. Stoffels, W. W. Stoffels, D. Vender, M. Kando, G. M. W. Kroesen, and F. J. Dehoog, *Phys. Rev. E* **51**, 2425 (1995)
- [6] T. Kimura and K. Ohe, *Plasma Sources Sci. Technol.* **8**, 553 (1999)
- [7] E. Meeks and J. W. Shon, *IEEE Trans. Plasma Sci.* **23**, 539 (1995)
- [8] M. Meyyappan, *J. Vac. Sci. Technol. A* **14**, 2122 (1996)
- [9] S. Ashida and M. A. Lieberman, *Jpn. J. Appl. Phys. Pt. I* **36**, 854 (1997)
- [10] M. Meyyappan, *Jpn. J. Appl. Phys. Pt. I* **36**, 4820 (1997)
- [11] S. Panda, D. J. Economou, and M. Meyyappan, *J. Appl. Phys.* **87**, 8323 (2000)
- [12] H. J. Yoon and T. H. Chung, *J. Korean. Phys. Soc.* **39**, 271 (2001)
- [13] Y. T. Lee, M. A. Lieberman, A. J. Lichtenberg, F. Bose, H. Baltès, and R. Patrick, *J. Vac. Sci. Technol. A* **15**, 113 (1997)
- [14] A. J. Lichtenberg, V. Vahedi, M. A. Lieberman, and T. Rognlien, *J. Appl. Phys.* **75**, 2339 (1994)

- [15] A. J. Lichtenberg, V. Vahedi, M. A. Lieberman, and T. Rognlien, *J. Appl. Phys.* **76**, 625 (1994)
- [16] J. T. Gudmundsson, A. M. Marakhtanov, K. K. Patel, V. P. Gopinath, and M. A. Lieberman, *J. Phys. D: Appl. Phys.* **33**, 1323 (2000)
- [17] J. T. Gudmundsson, I. G. Kouznetsov, K. K. Patel, and M. A. Lieberman, *J. Phys. D: Appl. Phys.* **34**, 1100 (2001)
- [18] T. Kimura, A. J. Lichtenberg, and M. A. Lieberman, *Plasma Sources Sci. Technol.* **10**, 430 (2001)
- [19] I. G. Kouznetsov, A. J. Lichtenberg, and M. A. Lieberman, *Plasma Sources Sci. Technol.* **5**, 662 (1996)
- [20] W. Tsai, G. Mueller, R. Lindquist, B. Frazier, and V. Vahedi, *J. Vac. Sci. Technol. B* **14**, 3276 (1996)
- [21] E. A. Hudson, T. Choi, O. Turmel, T. Zheng, K. Takeshita, S. Lee, A. M. Marakhtanov, and Cirigliano, in *Proceedings of the 26th International Symposium on Dry Process (DPS 2004)*, Tokyo, Japan, 2004
- [22] L. D. Tsendin, *Sov. Phys.-Tech. Phys.* **34**, 11 (1989)
- [23] A. J. Lichtenberg, I. G. Kouznetsov, Y. T. Lee, M. A. Lieberman, I. D. Kaganovich, and L. D. Tsendin, *Plasma Sources Sci. Technol.* **6**, 437 (1997)
- [24] A. J. Lichtenberg, M. A. Lieberman, I. G. Kouznetsov, and T. H. Chung, *Plasma Sources Sci. Technol.* **9**, 45 (2000)
- [25] I. G. Kouznetsov, A. J. Lichtenberg, and M. A. Lieberman, *J. Appl. Phys.* **86**, 4142 (1999)
- [26] P. J. Chantry, *J. Appl. Phys.* **62**, 1141 (1987)

- [27] J. T. Gudmundsson, J. Phys. D: Appl. Phys. **37**, 2073 (2004)
- [28] B. Eliasson and U. Kogelschatz, *Basic data for modelling of electrical discharges in gases : Oxygen* (ABB Asea Brown Boveri, Baden, 1986)
- [29] A. V. Phelps (compilation of electron cross sections used.)
ftp://jila.colorado.edu/collision_data/electronneutral/electron.txt
- [30] A. V. Phelps, Tabulations of cross sections and calculated transport and reaction coefficients for electron collisions with O₂, JILA Information Center Report (University of Colorado, Boulder, 1985).
- [31] E. Krishnakumar and S. K. Srivastava, Int. J. Mass Spectrom. Ion Processes **113**, 1 (1992)
- [32] T. Jaffke, M. Meinke, R. Hashemi, L. G. Christophorou, and E. Illenberger, Chem. Phys. Lett. **193**, 62 (1992)
- [33] S. G. Belostotsky, D. J. Economou, D. V. Lopaev, and T. V. Rakhimova (private communication)
- [34] B. L. Upschulte, W. J. Marinelli, and B. D. Green, J. Phys. Chem. **98**, 837 (1994)
- [35] S. Gomez, P. G. Steen, and W. G. Graham, Appl. Phys. Lett. **81**, 19 (2002)
- [36] R. L. Sharpless and T. G. Slinger, J. Chem. Phys. **91**, 7947 (1989)
- [37] J. T. Gudmundsson, J. Phys. D: Appl. Phys. **35**, 328 (2002)
- [38] J. T. Gudmundsson (electron excitation rate coefficients for oxygen discharge used.)
<http://www.raunvis.hi.is/reports/2002/RH-21-2002.html>
- [39] L. D. Thomas and R. K. Nesbet, Phys. Rev. A **11**, 170 (1975)
- [40] Y. Itikawa and A. Ichimura, J. Phys. Chem. Ref. Data **19**, 637 (1990)
- [41] R. R. Laher and F. R. Gilmore, J. Phys. Chem. Ref. Data **19**, 277 (1990)

- [42] S. A. Lawton and A. V. Phelps, J. Chem. Phys. **69**, 1055 (1978)
- [43] A. P. Hickman, M. Medikeri-Naphade, C. D. Chapin, and D. L. Huestis, Geophys. Res. Lett. **24**, 119 (1997)
- [44] T. Kimura (private communication)
- [45] H. J. Yoon, T. H. Chung, and D. C. Seo, Jpn. J. Appl. Phys. Pt. I **38**, 6890 (1999)
- [46] S. Ashida, C. Lee, and M. A. Lieberman, J. Vac. Sci. Technol. A **13**, 2498 (1995)
- [47] P. Chabert, J. L. Raimbault, J. M. Rax, and M. A. Lieberman, Phys. Plasmas **11**, 1775 (2004)
- [48] V. A. Lisovskii, Tech. Phys. **43**, 526 (1998)
- [49] L. Rhode, Ann. Physik **5**, 569 (1932)
- [50] G. M. Pateiuk, Sov. Phys. JETP **3**, 14 (1956)
- [51] G. Francis, *Ionization Phenomena in Gases* (Butterworths, London, 1960)
- [52] V. A. Lisovskiy and V. D. Yegorenkov, J. Phys. D: Appl. Phys. **32**, 2645 (1999)
- [53] V. A. Godyak, R. B. Piejak, and B. M. Alexandrovich, IEEE Trans. Plasma Sci. **19**, 660 (1991)
- [54] W. P. Allis and D. J. Rose, Phys. Rev. **93**, 84 (1954)
- [55] H. B. Smith, C. Charles, and R. W. Boswell, Phys. Plasmas **10**, 875 (2003)
- [56] V. A. Godyak and R. B. Piejak, J. Appl. Phys. **68**, 3157 (1990)
- [57] M. A. Lieberman and S. E. Savas, J. Vac. Sci. Technol. A **8**, 1632 (1990)
- [58] M. A. Lieberman, A. J. Lichtenberg, S. Kim, J. T. Gudmundsson, D. L. Keil, and J. Kim, Plasma Sources Sci. Technol. **15**, 276 (2006)
- [59] M. A. Lieberman, J. P. Booth, P. Chabert, J. M. Rax, and M. M. Turner, Plasma Sources Sci. Technol. **11**, 283 (2002)

- [60] M. A. Lieberman, A. J. Lichtenberg, and A. M. Marakhtanov, *Appl. Phys. Lett.* **75**, 3617 (1999)
- [61] P. Chabert, A. J. Lichtenberg, M. A. Lieberman, and A. M. Marakhtanov, *Plasma Sources Sci. Technol.* **10**, 478 (2001)
- [62] F. J. Mehr and M. A. Biondi, *Phys. Rev.* **181**, 264 (1969)
- [63] D. A. Hayton and B. Peart, *J. Phys. B* **26**, 2879 (1993)
- [64] R. Padgett and B. Peart, *J. Phys. B* **31**, L995 (1998)
- [65] X. Zhou and A. S. Dickinson, *Nucl. Instrum. Methods Phys. Res., Sect. B* **124**, 5 (1997)
- [66] R. E. Olson, *J. Chem. Phys.* **56**, 2979 (1972)
- [67] F. C. Fehsenfeld, D. L. Albritto, J. A. Burt, and H. I. Schiff, *Canadian J. Chem.* **47**, 1793 (1969)
- [68] A. A. Howling, L. Sansonnens, J. Ballutaud, C. Hollenstein, and J. P. M. Schmitt, *J. Appl. Phys.* **96**, 5429 (2004)
- [69] A. A. Howling, L. Derendinger, L. Sansonnens, H. Schmidt, C. Hollenstein, E. Sakanaka, and J. P. M. Schmitt, *J. Appl. Phys.* **97**, 123308 (2005)
- [70] P. Chabert, J. L. Raimbault, P. Levif, J. M. Rax, and M. A. Lieberman, *Phys. Rev. Lett.* **95**, 205001 (2005)